



저작자표시-비영리-변경금지 2.0 대한민국

이용자는 아래의 조건을 따르는 경우에 한하여 자유롭게

- 이 저작물을 복제, 배포, 전송, 전시, 공연 및 방송할 수 있습니다.

다음과 같은 조건을 따라야 합니다:



저작자표시. 귀하는 원저작자를 표시하여야 합니다.



비영리. 귀하는 이 저작물을 영리 목적으로 이용할 수 없습니다.



변경금지. 귀하는 이 저작물을 개작, 변형 또는 가공할 수 없습니다.

- 귀하는, 이 저작물의 재이용이나 배포의 경우, 이 저작물에 적용된 이용허락조건을 명확하게 나타내어야 합니다.
- 저작권자로부터 별도의 허가를 받으면 이러한 조건들은 적용되지 않습니다.

저작권법에 따른 이용자의 권리는 위의 내용에 의하여 영향을 받지 않습니다.

이것은 [이용허락규약\(Legal Code\)](#)을 이해하기 쉽게 요약한 것입니다.

[Disclaimer](#)

이학석사 학위논문

**Atomistic Origins of Carbon Solubility into
Amorphous and Crystalline Silicates at Ambient and
High Pressure: Implications for a Deep Carbon Cycle**

이성분계 결정질 규산염 및 비정질 규산염의
탄소 원자 주변 고상 핵자기 공명 분광분석:
지구 내부에서의 탄소 순환에 관한 미시적 기원 고찰

2011 년 8 월

서울대학교 대학원
자연과학대학 지구환경과학부
김 은 정

**Atomistic Origins of Carbon Solubility into
Amorphous and Crystalline Silicates at Ambient and
High Pressure: Implications for a Deep Carbon Cycle**

이성분계 결정질 규산염 및 비정질 규산염의
탄소 원자 주변 고상 핵자기 공명 분광분석:
지구 내부에서의 탄소 순환에 관한 미시적 기원 고찰

지도교수: 이성근

이 논문을 이학석사 학위논문으로 제출함

2011 년 8 월

서울대학교 대학원
자연과학대학 지구환경과학부
김 은 정

김은정의 이학석사 학위논문을 인준함.

2011 년 8 월

위 원 장	<u> 조 문 섭 </u>	(인)
부위원장	<u> 이 성 근 </u>	(인)
위 원	<u> 이 인 성 </u>	(인)

Abstract

Atomistic origins of carbon solubility into crystalline and non-crystalline silicates are essential to understand the effect of presence of light elements and/or volatiles (e.g. Carbon, CO₂, and etc.) on their diverse macroscopic thermodynamic and kinetic properties and to estimate the amount of carbon in the mantle. The structural information will give better insight into the deep carbon cycle in the earth's interiors and geochemical evolution of earth system through igneous and volcanic (degassing) processes. Because of these pronounced implications and importance, there have been extensive theoretical and experimental efforts to measure the amount of carbon species in silicate melts and to investigate the effect of carbon and volatiles on the melt properties. Despite these efforts, due to difficulties in direct probing of structures of volatile-containing crystals, glasses, and melt at high temperature and pressure conditions, little is known about their structures and carbon speciation in the melts and crystals at high pressure. In this study, we attempt to elucidate the atomic structures around carbon species in silicate crystals and melts at both ambient and high pressure up to 1.5 GPa using solid-state NMR and theoretical quantum chemical calculations.

We first explore the atomic environments around carbon in enstatite (MgSiO₃) synthesized at 1.5 GPa using ¹³C MAS NMR. ¹³C MAS NMR spectra show the multiple peaks at 126, 161, 171, 173, and 184 ppm. The peaks at 161, 171, and 173 ppm correspond to carbonate ion (CO₃²⁻), and the peak at 184 ppm is assigned to dissolved CO. The peak at 126 ppm is extremely sharp (FWHM of ~ 0.6 ppm) and it can either be due to four coordinated carbon (substituting Si in Si-tetrahedron) or due to gas phase

CO₂. In order to check that the sharp peak at 126 ppm is not from an instrumental artifact, we re-synthesized the sample with identical experimental conditions and collected ¹³C NMR spectra, which confirms that the peak at 126 ppm is from carbon species in the crystalline silicates. Then, in order to probe the origin of 126 ppm peak, we heated the sample at 750 °C for 10 minutes (decrepitation experiment). The ¹³C MAS NMR spectrum collected after decrepitation shows that the 126 ppm peak was removed, suggesting the carbon species responsible for the 126 ppm peak is rather unstable at 1 atm.

In order to provide further theoretical constraint on the origin of 126 ppm, we calculate ¹³C NMR chemical shift of carbon-substituted enstatite cluster using quantum chemical calculations based on the density functional theory. The results indicate that ¹³C NMR chemical shifts of four coordinated carbon in enstatite cluster can be ~ 254 ppm, suggesting that the 126 ppm peak is likely to be due to CO₂ rather than four coordinated carbon in the enstatite whereas further thorough theoretical calculations are certainly necessary to confirm the nature of the 126 ppm peak.

We also investigate the atomic environments around carbon in binary calcium oxide glasses synthesized at 1 atm under CO atmosphere using ¹³C MAS NMR. The NMR spectra for the glasses do not show any clear evidence for the carbon species (either molecular CO₂ or other species) in the silicate glasses at 1 atm. The spectrum for carbon-bearing calcium borate glasses synthesized under CO atmosphere, however, show a non-negligible carbon signal at ~270 ppm, implying that the observed peak may be due to the presence of four coordinated carbon in tetrahedral site (substituting boron in the BO₄ unit in the glass).

We finally report the ¹³C NMR spectrum for amorphous carbon

where the broad peak at 138 ppm corresponds to sp^2 hybridized structure of amorphous carbon. The first ^{13}C NMR spectrum for the compressed amorphous carbon at 1.5 GPa shows a new peak at 68 ppm due to carbon in a sp^3 hybridized bonding. This result indicates that there is a permanent pressure-induced densification in amorphous carbon characterized with a bond transition from sp^2 to sp^3 hybridization. The current results and methods show that natural abundance ^{13}C MAS NMR can be a quantitative probe of carbon species in both crystalline and non-crystalline silicates. The detailed structures around light elements and/or volatiles (e.g. Carbon, CO_2 , and etc.) in silicates revealed through ^{13}C NMR give insight into the atomistic mechanisms for deep carbon cycle in the earth's interior.

Keywords: volatiles, CO_2 , binary-component silicate glasses, enstatite, NMR, atomic structure

Tables of contents

ABSTRACT	1
TABLES OF CONTENTS	4
LIST OF FIGURES.....	6
LIST OF TABLES.....	11
1. INTRODUCTION	12
1.1. INTRODUCTION	12
1.2. PREVIOUS WORK	13
1.3. OBJECTIVES.....	19
2. NMR TECHNIQUES.....	21
3. THE EFFECT OF CARBON ON STRUCTURAL CHANGES IN SILICATE CRYSTALS.....	25
3.1. INTRODUCTION	25
3.2. EXPERIMENTS	26
3.3. RESULTS AND DISCUSSION.....	29
4. THE EFFECT OF CO ₂ IN STRUCTURAL CHANGES OF SILICATE GLASSES	37
4.1. INTRODUCTION	37
4.2. EXPERIMENTS	38
4.3. RESULTS AND DISCUSSION.....	42
5. FUTURE STUDIES.....	46
6. REMAINING QUESTIONS.....	47
7. CONCLUSION	47
REFERENCE.....	49
TABLES	55
FIGURES	60
APPENDIX SECTION.....	86

ABSTRACT IN KOREAN97

ACKNOWLEDGEMENT..... 오류! 책갈피가 정의되어 있지 않습니다.

LIST OF FIGURES

Figure 1 | Carbon solubility in silicate melts as a function of SiO₂ wt%. (A) Carbon solubility for the whole reference system. (B) Carbon solubility for the Na₂O-SiO₂ binary system. (C) Carbon solubility for the Na₂O-Al₂O₃-SiO₂ ternary system. (D) Carbon solubility for the multicomponent system.

Figure 2 | Carbon solubility in silicate melts as a function of mole fraction of non-bridging oxygen (NBO). (A) Carbon solubility for the whole reference system. (B) Carbon solubility for the Na₂O-SiO₂ binary system. (C) Carbon solubility for the multi-component system.

Figure 3 | Carbon solubility in silicate melts as a function of mole fraction of cations. (A) Carbon solubility as a function of mole fraction of Na₂O. (B) Carbon solubility as a function of mole fraction of CaO. (C) Carbon solubility as a function of mole fraction of MgO.

Figure 4 | Carbon solubility in silicate melts as a function of pressure. The upper limit of carbon solubility increases as increasing the pressure.

Figure 5 | Pictures of MgSiO₃ with 2.4 wt% amorphous carbon synthesized at 1.5 GPa in 1400°C for 48 hours. Figure 4A shows a first synthesized sample which has more impurities as-received and figure 4B shows a second synthesized sample which has relatively less impurities as-received. White grains in the picture are MgSiO₃ enstatite crystal, and black grains are compressed amorphous carbon.

Figure 6 | A picture of an MgSiO₃ grain with 2.4 wt% amorphous carbon synthesized at 1.5 GPa in 1400°C for 48 hours.

Figure 7 | Raman spectrum for crystalline MgSiO₃ with 2.4 wt% amorphous carbon at 1.5 GPa. The green, blue, and pink lines refer to the vibrational modes for crystalline MgSiO₃, gas phase CO₂, and CO₃²⁻ ion, respectively.

Figure 8 | One-dimensional ¹³C MAS NMR spectrum of MgSiO₃ with 2.4 wt% amorphous carbon. The bottom line refers to spectral features for rotor backgrounds, the middle line refers to spectral features for rotor and carbon-bearing MgSiO₃, and the top line refers to spectra features for carbon-bearing MgSiO₃, background-subtracted. The number in the bracket means the number of spacers used to collect the NMR signal from the sample.

Figure 9 | One-dimensional ¹³C MAS NMR spectrum of compressed amorphous carbon. The bottom line refers to spectral features for rotor backgrounds, the middle line refers to spectral features for rotor and compressed amorphous carbon, and the top line refers to spectra features for compressed amorphous carbon, background-subtracted. The number in the bracket means the number of spacers used to collect the NMR signal from the sample.
* refers to spinning sidebands.

Figure 10 | One-dimensional ¹³C MAS NMR spectrum of amorphous carbon. The bottom line refers to spectral features for rotor backgrounds, the middle line to spectral features for rotor and amorphous carbon, and the top line to spectra features for background-

subtracted amorphous carbon. The number in the bracket means the number of spacers used to collect the NMR signal from the sample. An asterisk refers to spinning sidebands.

Figure 11 | One-dimensional ^{13}C MAS NMR spectra of MgSiO_3 with 2.4% amorphous carbon, compressed amorphous carbon, and amorphous carbon. The rotor backgrounds were subtracted from the spectra. An asterisk refers to spinning sidebands.

Figure 12 | One-dimensional ^{13}C MAS NMR spectra of firstly and secondly synthesized MgSiO_3 with 2.4 wt% amorphous carbon. (top) Background-included spectra. (bottom) Background-subtracted and weight-normalized spectra.

Figure 13 | One-dimensional ^{13}C MAS NMR spectra of MgSiO_3 with 2.4 wt% amorphous carbon and MgSiO_3 heated at 750 °C for 10 minutes. The rotor backgrounds were subtracted from the original spectra and the spectra were weight-normalized.

Figure 14 | Atomic structure of MgSiO_3 , ortho-enstatite.

Figure 15 | A model cluster for simulating carbon-substituted MgSiO_3 .

Figure 16 | One-dimensional ^{13}C MAS NMR spectra of carbon-bearing CaSiO_3 and carbon-bearing CaO-SiO_2 eutectic composition synthesized in CO gas flow at 1 atm. (top) Background-included spectra. (bottom) Background-subtracted spectra. An asterisk refers to spinning sidebands.

Figure 17 | One-dimensional ^{13}C MAS NMR spectra of carbon-bearing

CaSiO₃ synthesized in CO gas flow at 1 atm. An asterisk refers to spinning sidebands.

Figure 18 | One-dimensional ¹³C MAS NMR spectra of carbon-bearing CaO-B₂O₃ synthesized in CO gas flow at 1 atm. An asterisk refers to spinning sidebands.

Figure A1 | ¹³C MAS NMR spectra of CaCO₃ and Na₂CO₃. The spectra are obtained from T₁ relaxation time measurements and the intensity is normalized to its maximum.

Figure A2 | Normalized maximum intensity of ¹³C NMR spectra for CaCO₃ and Na₂CO₃ as a function of delay time (s). Na₂CO₃ shows shorter T₁ relaxation time than CaCO₃.

Figure A3 | Micro-NMR Imaging of pisolite. The selected areas are where we measure the T₁ relaxation time of water absorbed into pisolite.

Figure A4 | Crystal structure of β-Ga₂O₃. (Top) Blue sphere is gallium and red sphere is oxygen. Unit cell structure of β-Ga₂O₃ shows two distinct gallium sites; octahedral sites and tetrahedral sites. (Bottom) Bond lengths of Ga-O in octahedron and tetrahedron. A and B mean the atoms at the top figure.

Figure A5 | ⁷¹Ga static NMR spectrum of β-Ga₂O₃.

Figure A6 | ⁷¹Ga static NMR spectrum of Ga-In-Zn oxide thin film.

Figure A7 | ⁷¹Ga static NMR spectra of β-Ga₂O₃ and Ga-In-Zn oxide thin film.

Figure A8 | ^{71}Ga NMR chemical shift range of four, five, and six-coordinated Ga in crystalline Ga compounds.

LIST OF TABLES

Table 1 | Functional property of analytical facilities

Table 2 | Calculated isotropic chemical shift of CO₂

Table A1 | T₁ relaxation measurement from micro-imaging NMR

Table A2 | NMR chemical shift, quadrupolar coupling, and asymmetric parameter η of Ga species, as reported in previous studies of ⁷¹Ga NMR

1. Introduction

1.1. Introduction

Microscopic origins of carbon solubility in silicate melts and crystals are an important process to understand the distribution of carbon, the property changes of silicates with carbon, and the evolution of layered earth and atmosphere (Eggler, Mysen et al. 1979; Richet and Bottinga 1984; Zhang and Zindler 1993; Blank and Brooker 1994; Keppler, Wiedenbeck et al. 2003; Behrens and Gaillard 2006; Shcheka, Wiedenbeck et al. 2006). Carbon dioxide is the second most abundant volatile in the mantle. The solubility of carbon in the silicate materials decreases as decreasing the pressure. Carbonates in the slab does not dissociated into carbon dioxide and oxide mineral in the subduction zone when the water contents of the surrounding area is not enough (Kerrick and Connolly 2001), and carbonate minerals can be transfer to the lower mantle as a magnesite (Biellmann, Gillet et al. 1993). It is believed that still large amount of carbon exists in the deep Earth calculated from the carbon contents in the meteorites (Green, Eggins et al. 1993).

Because of its importance and interests, there were many pioneering and intensive studies to measure the amount of carbon in silicate melts

(Pawley, Holloway et al. 1992; Blank, Stolper et al. 1993; Brooker, Kohn et al. 1999) and to define the property changes by the amount of volatiles (Brearley and Montana 1989; Kohn, Dupree et al. 1989; Brooker, Kohn et al. 2001; Brooker, Kohn et al. 2001). The attempts to measure the carbon solubility in silicates have been trying since 1930s, but direct measurement of the solubility and structure of carbon in silicates are performed since 1970s because of the difficulties of measuring a ppm scale of carbon and prevention of carbon contamination from other carbon sources (Blank and Brooker 1994). However, the exact atomic structure and the structural changes induced by pressure are not clearly demonstrated yet. In the next section, we present the previous works.

1.2. Previous Work

Measurement of the carbon solubility in silicate melts. The first experiment of measuring carbon in natural composition melt was performed by Wyllie and Tuttle (1959) and some early studies are based on the commercial silicates (Pearce 1964; Blank and Brooker 1994). The solubility of carbon dioxide in silicate decreases drastically as pressure decreases and that is too small to measure at 1 atm; therefore high pressure experiments are often performed to measure the solubility of carbon species in the silicates. However, the amount of carbon varies with the

analysis facilities(Blank and Brooker 1994), so one could obtain different solubility data of carbon in silicates with the same experimental condition. Figure 1 present the solubility trend of carbon in silicate melts as a function of weight percent of SiO₂ from the previous studies (Mysen, Arculus et al. 1975; Fine and Stolper 1985; Stolper, Fine et al. 1987; Kohn, Brooker et al. 1991; King and Holloway 2002; Nowak, Schreen et al. 2004; Mysen, Fogel et al. 2009; Morizet, Paris et al. 2010). Colors indicate the pressure in a series of colors; red color is the highest pressure and purple color is the lowest pressure. Figure 1A shows the carbon solubility for the whole composition system, figure 1B does that for the binary sodium-silicate system, figure 1C does that for the ternary sodium-aluminosilicate system, and figure 1D does that for the multi-component system. Although figure 1C suggests a weak relation between carbon solubility and weight percent of SiO₂, each figure in figure 1 shows the inverse relationship between the carbon solubility in various silicate melts and the weight percent of SiO₂. In figure 1B, pressure effect on carbon solubility increases until 20 kb. The solubility at 25 kb is less than that at 20 kb, so it is hard to pin down the pressure effect on the carbon solubility in binary system. It is tough to sentence any general equation of pressure effect on carbon solubility in silicate melts from these data because of many undetermined variables in the collected data; composition, the analytical method to measure the solubility, pressure and temperature condition. With classifying the data in detail

variables we can figure out the composition effects on the carbon solubility in silicate melts without extensive solubility measurement ourselves.

Figure 2 shows the effect of non-bridging oxygen (NBO) on the carbon solubility in silicate melts. Figure 2A presents the data for the overall composition system, figure 2B does for the binary sodium-silicate system, and figure 2C does for the multi component silicate system. The data for the ternary system is absent because only fully polymerized silicate system, which means that no NBO exists in the system, are present in the ternary sodium-aluminosilicate experiments. In many cases the mole fraction of NBO increases as decreasing the weight percent of SiO_2 , so figure 2 shows the opposite trend compared with figure 1. Figure 2 indicates that the carbon solubility in silicate melts tends to increase as the mole fraction of NBO increases.

Figure 3 shows the cation effect on carbon solubility in silicates. Figure 3A is a relationship between the mole fraction of Na_2O and carbon solubility, figure 3B between the mole fraction of CaO and carbon solubility, and figure 3C between the mole fraction of MgO and carbon solubility. Carbon solubility in silicate melts is inverse proportion to the mole fraction of Na_2O , and proportion to the mole fraction of CaO and MgO . These results are identical to the carbon solubility in natural melts which is less than 200 ppm in submarine basalt and less than 30 ppm in rhyolitic glasses(Blank and Brooker 1994). It seems that the effect of CaO is greater

than that of MgO, but we cannot find any reason for cation effect on solubility from previous works.

Figure 4 shows the pressure effect on the carbon solubility in silicates. Data are labeled by the composition of silicate melts. There is a positive correlation between pressure and solubility and if the data are normalized into weight percent of SiO₂ in silicate melts it might be shown a stronger correlation.

Measuring the carbon solubility in the silicate is also important in material sciences because of the slag. The carbon in molten slag control the ductility and weldability of the iron(Jung 2006) so calcium-aluminates and calcium silicates are studied(Berryman and Sommerville 1992; Jung 2006). Carbon in slag can also immobilize the hazard element, Cr, from industrial waste(Macias, Kindness et al. 1997) and some calcium-rich industrial wastes are used as a feedstock of mineral CO₂ sequestration (Huijgen and Comans 2005).

Speciation of carbon in silicates. Spectroscopes like Raman, IR, and NMR have been used to identify the speciation of carbon in silicates. The possible species of carbon in silicates are as followed; carbonate, molecular CO, molecular CO₂, methane, moissanite, and neutral carbon (Blank and Brooker 1994; Holloway and Blank 1994; Luth 2003).

Some suggests that four-coordinated carbon can exists as a substitution of Si in silicates (Freund, Kathrein et al. 1980; Shcheka, Wiedenbeck et al. 2006). They suggest that carbon solubility in silicate crystal shows the possibility of carbon substitution into tetrahedral Si sites. However, the experimental evidence of tetrahedral carbon is not found yet.

With Raman and IR spectroscopy, we can define not only the species of carbon in silicate melts but also the vibrational modes of each species. Blank and Brooker (1994) explained the vibrational mode of CO₂ and CO₃²⁻ which can be detected through Raman and IR. Symmetric stretch of CO₂ can be detected by Raman at 1337 cm⁻¹, and asymmetric stretch of CO₂ can be detected by IR at 2349 cm⁻¹. Each of two different asymmetric bends of CO₂ has 667 cm⁻¹ frequency in IR spectrum. However, two times of asymmetric bend of CO₂ is similar to the symmetric stretch of CO₂ and this makes resonance on the energy level and produce a perturbation on Raman spectrum, so we can get Fermi doublet of CO₂ at 1286 cm⁻¹ and 1388 cm⁻¹ in Raman spectrum. Asymmetric stretching of CO₂ in IR spectrum is detected as a doublet at 2340 and 2360 cm⁻¹ because of rotational effects (Brey 1976; Blank and Brooker 1994). Minor bands are shown in 3711 cm⁻¹ for symmetric and asymmetric stretch combined band, 2287 cm⁻¹ for asymmetric stretch of ¹³CO₂, and 2229 cm⁻¹ for asymmetric stretch of ¹⁴CO₂.

Vibrational modes of carbonate ion are more complex than that of CO₂ because it can have two different symmetry species, D_{3h} and C_{2v}. D_{3h}

symmetry species have equivalent C-O bond length. Active frequency of Raman and IR is changed through the symmetry of the molecule. There are four categories of fundamental vibrational motions of CO_3^{2-} ion; symmetric stretch, out-of-plane bend, asymmetric stretch, and in-plane bend. The frequency of each motion is 1063 cm^{-1} , 879 cm^{-1} , 1415 cm^{-1} , and 680 cm^{-1} , respectively. If carbonate ions has C_{2v} symmetry, then all of vibrational modes are active in Raman and IR. However, if it has D_{3h} symmetry, symmetric stretch is only Raman active and out-of-plane bend is only IR active. Frequency range from 1375 to 1680 cm^{-1} is assigned for asymmetric stretch of distorted carbonate (Mysen and Virgo 1980; Fine and Stolper 1985).

XRD can be used for determining the kinetics of carbon dioxide mechanosorption in Ca-silicates (Kalinkin 2009). However, it does not show the CO_2 peak but it shows that the peak intensity in XRD data of wollastonite increases as mechanosorption time increases. This result indicates that as mechanosorption of CO_2 continued, structure of wollastonite changed from crystal to amorphous.

Diffusion of carbon in silicates. The diffusion of carbon in silicate melts and crystals are also important to understand the degassing processes during the upwelling of magma (Nowak, Schreen et al. 2004). Nowak et al. (2004) studies carbon diffusion from rhyolitic to hawaiitic

melt composition and found that the mobility of CO₂ is constant though the changes of composition.

1.3. Objectives

Most of previous studies are focused on the measuring of carbon solubility in silicate melts and the exact atomic structure of carbon in silicate melts has not revealed based on the experimental data. Kubicki (Kubicki and Stolper 1995) made thermodynamic model of dissolution mechanism of carbon dioxide in silicate glasses, but there is no reliable studies with NMR which can support the previous experimental data with qualitative and quantitative atomic environment analysis.

Table 1 shows the analytical advantages of NMR from other analytical methods. We can obtain the information in short range order of the system so there were attempts to get NMR data of silicate melts; however they were focused on the multi-component system which means that we cannot identify which variables do affect on the structural changes of carbon and silicon in silicates. Using simple binary model system, we can show the effect of pressure on the carbon solubility with carefully defined variables. Fundamental aim of this thesis is to obtain good ¹³C NMR spectra of silicate glasses and crystals from the simple composition systems to reveal the atomic structure of carbon in silicates precisely.

The section 2 presents a brief introduction of NMR technique. In this section, previous experiments for ^{13}C NMR study like T_1 relaxation time measurement and NMR imaging is also presented. The section 3 presents studies of carbon solubility in crystalline MgSiO_3 at 1.5 GPa. It includes not only NMR study but also quantum chemical calculation study. The section 4 presents progress on studies of carbon solubility in CaO-SiO_2 binary system. ^{13}C NMR study of CaO-SiO_2 binary system has had a problem due to the low solubility of carbon and CO_2 in 1 atm study.

Appendix sections present T_1 relaxation experiment of calcium carbonate and sodium carbonate in ^{13}C NMR study, brief introduction of NMR imaging, and ^{71}Ga NMR study of Ga-In-Zn oxide thin film.

2. NMR techniques

Nuclear Magnetic Resonance (NMR) is a nuclide-specific facility which can give us the information of atomic structure of material in the short-range order. NMR is especially useful to analyze the atomic structure than other analysis techniques because it can read only one nuclide in one experiment so we can reduce the multi-component bonds.

Sample is located in the center of the magnetic coil. The nuclear spins of the sample are aligned along the magnetic field. If we give a pulse to the sample, the polarized nuclear spins lose their alignment temporarily and return to their original state. In this process, nuclear spins make signals. However, there are other nuclides in molecules so interactions between the magnetic field and spin interaction of neighbor nuclide make the chemical shift which has information of atomic environments.

^{13}C is the isotope of ^{12}C and ^{14}C . The most abundant isotope of carbon is ^{12}C , but the nuclear spin of ^{12}C is zero because ^{12}C has even numbers of neutron and proton. Some elements which have same number of neutron and proton show no spins in magnetic field, too. This is why we use ^{13}C for NMR study despite of the low natural abundance of ^{13}C (1.1 %). The sensitivity of nuclide in NMR is dependent on the gyromagnetic ratio γ and natural abundance. ^{13}C has 4 times low gyromagnetic ratio than ^1H and its natural abundance is only 1.1 % so it shows 6000 times low

sensitivity the ^1H NMR spectrum. That means we need to focus on collecting the high resolution NMR spectrum to overcome these difficulties. We use ^{13}C enriched sample for ^{13}C NMR study to reduce the collection time and enhance the intensity of signal. Fortunately ^{13}C is 1/2 spin nuclide which means that it is not a quadrupolar interaction nuclide, so we can concentrate only on enriching the sample with ^{13}C .

Static NMR and MAS NMR. Static NMR is a NMR experiment which does not spin the rotor by the air. Liquid has no anisotropic properties, so liquid-state NMR uses static NMR experiment and the spectrum features very sharp peaks. Solid has anisotropic properties, so the static solid-state NMR features broad peaks which have three distinct peaks. Compared to static NMR, magic angle spinning (MAS) NMR is a NMR experiment which spins the rotor in a specific angle (54.7°). The first-order parameter of anisotropic is angle dependent, and it is eliminated when the angle is 54.7° . As the first-order derivation of anisotropic parameter disappears, the spectrum shows sharp peaks and spinning side band. The distance between a peak and a spinning side band is determined by spinning speed, so faster the spinning speed broader the distance between a peak and a spinning side band. Spinning side band appears in the area of static NMR spectrum, so if the anisotropy of the nuclide is big, more than two spinning side band will appear.

Echo NMR. Echo NMR is a NMR experiment which gives two different pulses to the sample. One is 45° pulse and the other is 90° pulse. Signals differ depending on the recycle delay time because each species has different relaxation time, so we cannot use echo NMR as a quantitative analysis. With echo NMR experiment we get a dome-shaped spectrum and it makes us easy to simulate the data, so echo NMR is often used for detecting the number of different atomic environment of the sample.

T_1 relaxation NMR. T_1 relaxation NMR uses two pulses to get a spectrum. One is 90° pulse, and the other is 180° pulse. Originally, T_1 relaxation means the dephasing time of one-direction polarized nuclear spin in molecule. However, we cannot erase the magnetic field of NMR so we use opposite way to determine T_1 relaxation time. The net spin direction of sample in magnetic coil is polarized in one direction. If we give a pulse to nuclear spin then we can depolarize the nuclear spin temporarily. After the pulse, nuclear spins return to their original state and the polarization time is as same as depolarization time.

For further information and experimental exercises, see appendix I.

NMR Imaging. NMR Imaging is non-destructive 2D and 3D imaging technique with the μm resolution. NMR imaging uses magnetic

field gradient to get three dimensional image of sample. Detector obtain the signals from different position with different field gradient, so the signals can be divided to its positions. There are several methods to get a NMR imaging. 'm_msmevtr' method is the protocol to obtain a 2D image of a sample. 'm_ge3d' method is for 3D image of a sample.

For further information and experimental exercises, see appendix II.

3. The effect of carbon on structural changes in silicate crystals

3.1. Introduction

MgSiO₃ is the most abundant mineral composition in the mantle and mantle is thought to be the largest carbon reservoir in the Earth (Jambon 1994; Shcheka, Wiedenbeck et al. 2006). Understanding the atomic structure of carbon in silicates is important to estimate the amount of carbon in the mantle, however, we do not know the atomic structure of amorphous silicate properly now. Crystals have unit cell which means that we know their atomic structure well, so it is necessary to identify the atomic structure of carbon in silicates from the silicate crystals and it will be the first step to figure out the carbon solubility and carbon diffusion in the crystalline phase of silicates. In this section, ¹³C NMR study of carbon-bearing MgSiO₃ is presented. There is an unidentified peak in 126 ppm, so decrepitation experiment and quantum chemical calculation is also performed.

3.2. Experiments

Sample Preparation. MgSiO_3 , powdered crystalline phase, is cooked with 2.4 wt% of ^{13}C enriched amorphous carbon using piston cylinder at 1.5 GPa in 1400 C for 48 hours with H_2O . H_2O was added to activate the reaction. The 1.5 GPa condition is the same pressure as the pressure of 40 km depth in Earth's crust. Sample was synthesized twice at the same condition; the first one displayed in figure 4A has starting material as a impurities and the second one displayed in figure 4B has little impurities so second one shows nearly white crystalline MgSiO_3 phases. Each picture is taken at 3.2x magnification. In figure 4, white material is MgSiO_3 enstatite in which ^{13}C might be diffused and black material is compressed amorphous carbon which in transformed from ^{13}C enriched amorphous carbon when the sample was pressured and heated in piston cylinder.

Microscopic Observations. Microscopic observations were performed using Leica M205 C.

Raman Spectroscopy. Raman spectra for the crystalline MgSiO_3 with 2.4 wt% amorphous carbon, amorphous carbon, and compressed amorphous carbon were obtained by Ramboss LS 200 t Raman spectrometer. For the experiment, 488 nm lasers were used and its beam

diameter was 0.8 mm. Exposure time of the sample was 4 s and the number of accumulation was 100 for every spectrum. The Raman spectrum for the crystalline MgSiO₃ was obtained with 300/500 grating, and the Raman spectra for amorphous carbon and compressed amorphous carbon were obtained with 300/500 and 1800/500 grating.

NMR Spectroscopy. The ¹³C NMR spectra for the MgSiO₃ enstatite with 2.4 wt% of ¹³C enriched amorphous carbon were obtained by using a Varian 400 MHz solid-state NMR spectrometer (9.4 T) at a Larmor frequency of 100.582 MHz using a 3.2 mm zirconia rotor in a Varian double-resonance probe. The ¹³C MAS NMR spectra were referenced to solid-state adamantane (ADM) whose left peak is at 38.56 ppm in reference to tetramethylsilane (TMS). TMS is the NMR chemical shift reference material, but because of J-coupling effect of TMS, ADM is used as a reference in this thesis. One pulse sequence was used for ¹³C 1D MAS NMR and nearly 86400 scans were averaged to achieve the high resolution 1D MAS NMR spectra. The relaxation delay time was 5 s for ¹³C MAS NMR and the radio frequency pulse strength was 1.3 μs. Sample spinning speed is 14 kHz. The acquisition time is 30.72 ms which is longer than usual MAS NMR but shorter for gas phase NMR. The carbon-bearing silicate sample was packed in the rotor intentionally put the crystalline MgSiO₃ crystals in

the center of the rotor to get more carbon signals dissolved in the crystalline enstatite.

Quantum Chemical Calculations. Quantum chemical calculations are effective tools for obtaining microscopic properties of the sample which are hard to get from the experimental data. NMR chemical shielding calculations were performed using Gaussian 03. Workstation is installed in the Earth materials science laboratory. Gaussian basis sets are used in quantum chemical calculations and are more adequate for the desired results because they consider the electron interactions during calculations.

A cluster of carbon substituted MgSiO_3 orthoenstatite was not optimized due to the instability of carbon in tetrahedral site. NMR chemical shielding calculations were performed at the Becke, three-parameters, Lee-Yang-Parr (B3LYP) hybrid functional level of theory with the 6-311+G(2d) and 6-311G(2d) basis sets; and at the unrestricted Hartree-Fock (UHF) level of theory with the 6-311+G(2d) and 6-311G(2d). The cluster is modified from the structure of orthoenstatite at 0 GPa (Hugh-Jones and Angel 1994); three tetrahedron were cut from the crystal unit cell and a carbon was substituted into the middle tetrahedron.

Absolute chemical shielding calculations varies with level of theory, so structure of CO_2 is used for a reference of calculations. They were performed at the Hartree-Fock (UH) level of theory with the 6-31G* and 6-

311+G(2d) basis sets; unrestricted Hartree-Fock (UHF) level of theory with the 6-31G* and 6-311+G(2d) basis sets; and at the Becke, three-parameters, Lee-Yang-Parr (B3LYP) hybrid functional level of theory with the 6-311+G(2d) and 6-311G(2d) basis sets.

3.3. Results and Discussion

Microscopic Observation. Figure 5 and 6 show the pictures of MgSiO₃ sample taken with Leica M205 C. The sample shows white color in naked-eye observation. In grain by grain, they show different aspects. About 10% of grains of the samples show white and opaque appearances under the microscope and they seem to be at the interface of the MgSiO₃ and the amorphous carbon. The other 90% of grains of the samples show transparent appearances under the microscope and they seem to be inside of the sample when the pressure was applied. Both of them show the crystalline MgSiO₃ peak with Raman spectroscopy.

Raman Results. Figure 7 shows the Raman spectrum for crystalline MgSiO₃ with 2.4 wt% amorphous carbon (first sample). The green, blue, and pink lines refer to the vibrational modes for crystalline MgSiO₃, gas phase CO₂, and CO₃²⁻ ion, respectively. The multiple peaks in the spectrum are consistent with the vibrational modes for crystalline MgSiO₃; however,

no peaks are consistent with the vibrational modes for gas phase CO₂ or CO₃²⁻ ion. This spectrum indicates that white grains in the first sample are crystalline MgSiO₃, and carbon species in the MgSiO₃ is too small to detect by Raman spectroscopy.

¹³C MAS NMR Results. Figure 8, 9, and 10 shows the one-dimensional ¹³C MAS NMR spectra of MgSiO₃ with 2.4 wt% amorphous carbon, compressed amorphous carbon, and amorphous carbon. The number in the bracket of the background label means the number of spacers to use to collect the NMR spectrum from the sample. The sum of the area of the spectrum represents the amount of elements in the sample and the total area of the background is much larger than that of MgSiO₃ spectrum. This means the amount of carbon impurity is significant compared to the total amount of carbon in the sample. The intensity from the sample is smaller than that from background signal; therefore background subtraction is needed for each spectrum. Background subtracted spectra are presented in the top of each spectrum, and they are gathered in figure 11.

In figure 11, there are peaks at 184 ppm, 171 ppm, 161 ppm, and 126 ppm in ¹³C MAS NMR spectrum of enstatite. One broad peak from 40 ppm to 120 ppm is shown in compressed amorphous carbon spectrum and one broad peak from 90 ppm to 170 ppm is in amorphous carbon spectrum.

According to the previous ^{13}C NMR experiments of silicates (Kohn, Brooker et al. 1991), dissolved CO shows a peak at 184 ppm and carbonate ion (CO_3^{2-}) shows a peak in the range between 160 and 170 ppm which can be shifted up to 3 ppm due to the distortion of carbonate ion in the silicate structure. A peak at 126 ppm is assigned as CO_2 in Kohn et al.(1991). However, the data that Kohn et al. present have central spike at 125 ppm so we cannot see the clear peak at 125 ppm and it might seem that it is some noises in the spectrum. Rockafellow et al.(2009) suggest that sp^3 -hybridized carbon in TiO_2 structure shows a peak at 126 ppm and peak at 126 ppm in figure 11 shows a similar peak width and intensity in Rockafellow et al.(2009).

For amorphous carbon, graphite-like sp^2 structure appears at 138 ppm in ^{13}C MAS NMR spectrum and diamond-like sp^3 structure appears at 68 ppm (Alam, Friedmann et al. 2002; Alam, Friedmann et al. 2003). In figure 11, we can find the structural changes of carbon. As sample got pressured, sp^2 structure carbon in amorphous carbon is transformed into sp^3 structure carbon in compressed amorphous carbon.

Figure 12 shows the ^{13}C MAS NMR spectra of first and second synthesized carbon-bearing MgSiO_3 sample. Second sample was synthesized to find out whether the peak at 126 ppm is a real atomic evidence of carbon species in MgSiO_3 or not. It is abbreviated to first sample and second sample. Top spectra show the background-including

spectra and bottom spectra show background-subtracted and weight-normalized spectra. In the top spectra, second sample shows one peak at 126 ppm and no other peaks presented in first sample are found. Peak intensity at 126 ppm of second sample spectrum also decreases compared with that of first sample spectrum. The weight of the sample in the rotor is slightly different; first sample is 59.8 mg and second sample is 36.5 mg. To eliminate the effect of weight from the intensity differences, bottom spectra are weight-normalized after background subtraction. After the weight normalization, however, two spectra present differences in peak intensity and it is thought to be the differences in total amount of carbon in the sample. Important point of this figure is that a peak at 126 ppm does appear again in second sample and it is not a noise or an experimental error. To identify the atomic structure of carbon which can show a peak at 126 ppm in NMR spectrum, decrepitation experiment and quantum chemical calculation is followed.

Decrepitation experiment is performed on the second sample and figure 13 shows the results. When the sample is heated around 750 °C, fluid inclusions and trapped minerals escape from their original sites. After the 10 minutes of heating at 750 °C, the peak at 126 ppm disappears. FWHM (full width half maximum) of the peak at 126 ppm is about 0.6 ppm and that value is hard to find in solid-state NMR spectra. Usual FWHM of solid state material is more than 2 ppm. In case four coordinated carbon breaks

off its bond due to its unstable state, quantum calculation is followed to confirm the structure.

Figure 14 shows the atomic structure of MgSiO_3 , orthoenstatite. Orthoenstatite is one of polymorphs of MgSiO_3 ; orthoenstatite, clinoenstatite, and protoenstatite. Orthoenstatite is high temperature low pressure phase, clinoenstatite is low temperature low pressure phase, and protoenstatite is high pressure and high temperature phase. The transition between orthoenstatite and clinoenstatite is $600\text{ }^\circ\text{C}$ and the transition between orthoenstatite and protoenstatite is over 8 GPa and $900\text{ }^\circ\text{C}$ (Angel, Chopelas et al. 1992). The atomic position of orthoenstatite is referenced to (Hugh-Jones and Angel 1994).

Enstatite is a single-chain mineral; therefore there are four sites for carbon to be substituted during the synthesis: the bridging oxygen site, the non-bridging oxygen site, tetrahedral site of Si, and the network-modifying cation site of Mg. However, because the number of valence electrons of carbon is different from that of Mg, there is low possibility to substitute carbon with Mg.

Figure 15 shows structure model cluster for simulating carbon-substituted MgSiO_3 . Three tetrahedron and combined eight Mg is selected from the original structure and carbon is substituted into the middle tetrahedron. We cannot get the absolutely correct absolute values from the quantum chemical calculations; therefore we use CO_2 as a reference

material to compare the result from the MgSiO₃ structure. The bond length of C-O single bond is 1.53 Å and that of C=O double bond is 1.16 Å. The bond length of Si-O is 1.64 Å. Differences between C-O bond length and Si-O bond length make the model cluster distorted; therefore we calculated the single point energy to prevent the effect of structure during the optimization. Table 2 shows the results of chemical shift of CO₂ in quantum chemical calculations. These data show that B3LYP/6-311+G(2d) method corresponds well with experimental data. With B3LYP/6-311+G(2d) method, structure in figure 15 shows 254.5637 ppm as a chemical shift. This value is far from the 126 ppm in ¹³C NMR; however, we need to find the calculation trend from other method and to calculate with various C-O bond lengths to confirm the peak assignment. The cation radius of carbon is 0.15 Å and that of silicon is 0.26 Å which means that there have to be a distortion in crystal structure when the carbon substitutes Si in Si-tetrahedral site. It is not clear whether the crystal structure maintains with extended four-coordinated carbon in tetrahedral site or the carbon-substituted tetrahedron shrinks in some ways. To confirm the atomistic environments of carbon in crystalline MgSiO₃, we need to perform quantum chemical calculations with various model clusters which have variety ranges of the C-O bond lengths.

Carbon solubility in silicate crystals may follow this equation.

$$S = k \exp\left(-\frac{\Delta G + P\Delta V}{RT}\right)$$

S is the solubility of carbon, k is constant, ΔG is difference of Gibbs free energy between volatile free mineral and volatile saturated mineral, P is pressure, ΔV is volume of the mineral, R is gas constant, and T is the temperature of the system.

Studies of Ar solubility in silicate melts and CO₂ solubility in silicate crystals suggests that there will be solubility limits depending on the composition of the mineral because of the phase transitions near 440 km (Sarda and Guillot 2005; Shcheka, Wiedenbeck et al. 2006; Bouhifd, Jephcoat et al. 2008) It is expected that pressure-induced experiment with MgSiO₃ shows similar trend because we can find the carbonatite melt in high pressure samples which indicate that carbon and silicate are not mixed well in high pressure environments, and the free volume of the silicate crystal and melts will decrease as the pressure increases and this phenomena will occur the decrease solubility of CO₂ and CO₃²⁻.

Carbon solubility in silicate crystals can give us the evolution of carbon distribution in the earth. Earth originally consisted of crystalline minerals and layered earth was made after the magma ocean. Atomic structure of carbon would be changed with the pressure, temperature, and composition and the partitioning coefficient of the carbon would be the important factor to determine where the carbon would be transferred. Investigating the atomic environment of carbon in silicate crystals at low

pressure would be the first step to reveal the evolution and distribution of carbon in silicates from the fundamental level.

CO₂ capture and storage (CCS) is one of the big issues these days and this study could give information of carbon reactivity and atomistic environment. CO₂ storage process have four steps; first one is physical trapping, second one is residual trapping, third one is solubility trapping, and last one is mineral trapping. In this process CO₂ interacts with silicate minerals around 100 bar pressure. If we carry on the experiments at lower pressure, we can identify the carbon environment during CCS processes and it may give more information of CO₂ storage and modeling.

4. The effect of CO₂ in structural changes of silicate glasses

4.1. Introduction

Carbon solubility in silicate melts is important for understanding the evolution of the magma and volcanic eruption. Solubility of carbon in the silicate can lower the melting point of the minerals which means that composition of the partial melting magma can be changed by the amount of volatiles. Volcanic eruption at mid-ocean ridge is usually quietly erupted; however, when the contents of carbon dioxide is high in the magma, intense eruption can occur at mid-ocean ridge volcanoes (Helo, Longpre et al. 2011).

There are intensive previous studies which show the atomic structure of carbon in silicate melt and thermodynamic modeling of dissolution mechanism of carbon in silicates. However, structural analysis of carbon in silicates has not been studied due to the difficulties in getting high resolution NMR spectra. In this thesis, high resolution NMR studies are performed to reveal the atomic structure of carbon in silicate glasses. The composition of the system is CaO-SiO₂ binary system chosen from the

previous data in the section 1 which shows that solubility of carbon increases in the high Ca^{2+} ratio and low SiO_2 ratio conditions.

4.2. Experiments

Sample Preparation. A sample made by Sun Young Park at 1 atm was used to confirm whether carbon dioxide was dissolved in silicate glasses at 1 atm. The composition of the sample was the join of diopside and Ca-tschermakite as 25:75(abbreviated as CMAS), and 0.2 wt% of Co oxide was added to enlarge the spin-lattice relaxation and cut down the collection time. Sintered MgO was used for synthesizing the sample. One CMAS sample from Sun Young Park and two CMAS sample made by me were used for detection. Every sample was grinded in an agate mortar as a powder. The mixture of CMAS powders in a Pt crucible was heated up to 1600 °C in DelTech furnace with 275 °C/hr of the heating ratio and it was fused for 1 hour at 1600 °C. The heated sample was quenched into glasses by manually lowering the temperature of Pt crucible into distilled water.

CaSiO_3 glass was synthesized from mixtures of CaCO_3 powder and SiO_2 powder. Each powder was dried in a box furnace at 300 °C more than a week. Powders were mixed in an agate mortar and Pt crucible was used to fuse the mixtures. The mixture was heated with DelTech furnace with 275 °C/hr of the heating rate until the mixture was heated up to 1600 °C,

and the mixture was heated up to 1650 °C by manually raising the temperature of the furnace with heating rate about 1 °C/min. The mixtures were fused at 1650 °C in the air for 20 minutes. After then the heated sample was quenched into glasses by manually lowering a Pt crucible into distilled water. This sample was used for ¹³C NMR study for 1 atm sample and sent to Geophysical lab. in Carnegie Institute of Washington for higher pressure sample.

CaSiO₃ glass for 1 atm sample with CO gas was synthesized at Prof. Yoon-Bae Kang's laboratory at Graduate Institute of Ferrous Technology (GIFT), POSTECH. CaCO₃ powder and SiO₂ powder were used for synthesizing the sample. Each powder was dried in a box furnace at 300 °C more than a week and grinded in agate mortar. The mixture of powders were put into a micro vial, vacuum-packed, and sent to GIFT. Graphite crucible was used to fuse the mixtures and heating rate was 180 °C/hr. Deoxygenated argon gas was used until the temperature reached to 1600 °C and the temperature was maintained at 1600 °C for 20 hours with pure CO gas flow to equilibrate the sample. The sample was quenched with He gas after then.

CaO-B₂O₃ glass for 1 atm sample with CO gas was synthesized at Prof. Yoon-Bae Kang's laboratory at Graduate Institute of Ferrous Technology (GIFT), POSTECH. CaCO₃ powder and B₂O₃ glass were used for synthesizing the sample. CaCO₃ powder was dried in a box furnace at

300 °C more than a week and B₂O₃ glass was synthesized by several times of melting and quenching of B(OH)₃ above 470 °C. The ratio of CaO and B₂O₃ was 34.7 to 65.3 in mass percent and 39.7 to 60.3 in mol percent. Pre-materials were grinded in agate mortar. The mixture of powders were put into a micro vial, vacuum-packed, and sent to GIFT. Graphite crucible was used to fuse the mixtures. Deoxygenated argon gas was used until the temperature reached to 1500 °C and the temperature was maintained at 1500 °C for 18 hours with pure CO gas flow at the flow rate of 100 ml/min to equilibrate the sample. The sample was quenched with He gas after then.

CaMgSi₂O₆ glass for high pressure experiment was synthesized from mixtures of CaCO₃ powder, MgO, and SiO₂ powder. MgO used for synthesizing the sample was sintered at 1300 °C for 2 hours. Each pre-material was dried in a box furnace at 300 °C more than a week, and was grinded and mixed in an agate mortar as a powder. The mixture of CaMgSi₂O₆ powder in a Pt crucible was heated up to 1600 °C in DelTech furnace with 275 °C/hr of the heating rate, and were fused at 1600 °C in the air for 1 hour. After then the heated sample was quenched into glasses by manually lowering the temperature of Pt crucible into distilled water.

Analysis of Carbon Solubility. Elemental analyzer was used for quantifying the solubility of carbon in silicate glasses, which can quantify the amount of C, H, N, and S in compounds. Inside of the equipment, the

compounds were heated to produce oxides. The oxides were separated with their molar weight when they came through a column in an oven and TCD detector calculated the amount of each oxide. The lowest detect limit of elemental analyzer was 100 ppm.

MAS NMR spectrum collection. The ^{13}C NMR spectra for the CaO-SiO₂ binary system were obtained by using a Varian 400 MHz solid-state NMR spectrometer (9.4 T) at a Larmor frequency of 100.582 MHz using a 4 mm silicon nitride rotor in a Varian double-resonance probe. The ^{13}C MAS NMR spectra were referenced to solid-state adamantane (ADM) whose left peak is at 38.56 ppm in reference to tetramethylsilane (TMS). MAS spectra were obtained using one pulse sequence and 86400 scans were averaged to achieve the high resolution 1D MAS NMR spectra. The relaxation delay time was 5 s for ^{13}C MAS NMR and the radio frequency pulse strength was 1.0 μs . Sample spinning speed is 14 kHz. The acquisition time is 20.48 ms.

The ^{13}C NMR spectrum for the CaO-B₂O₃ binary system were obtained by using a Varian 400 MHz solid-state NMR spectrometer (9.4 T) at a Larmor frequency of 100.582 MHz using a 3.2 mm zirconia rotor in a Varian double-resonance probe. The ^{13}C MAS NMR spectra were referenced to solid-state adamantane (ADM). MAS spectrum was obtained using one pulse sequence and 86400 scans were averaged to achieve the high resolution 1D MAS NMR spectra. The relaxation delay time was 5 s

for ^{13}C MAS NMR and the radio frequency pulse strength was $1.3 \mu\text{s}$ (30° degree pulse). Sample spinning speed is 14 kHz. The acquisition time is 20.48 ms.

4.3. Results and Discussion

Analysis of Carbon Solubility in Silicate Glasses. Carbon solubility in silicate glasses is used by elemental analyzer. Before making a 1 atm silicate sample with CO_2 , we first check the carbon solubility in CMAS sample. Carbon solubility in CMAS samples are detected as 409 ppm for CMAS sample from Sun Young Park in first detection, and 84 ppm in second detection. It is 174 ppm and 35 ppm for CMAS synthesized by me in first detection, and 123 ppm and 52 ppm in second detection. There is unstability of carbon in CMAS silicate glasses and analytical method because its error range is much bigger than the total carbon solubility in silicate glasses.

^{13}C MAS NMR Results. Figure 16 and figure 17 show the ^{13}C MAS NMR studies of the CaO-SiO_2 binary system. Figure 16 shows the ^{13}C MAS NMR spectra of CaSiO_3 and CaO-SiO_2 eutectic system which are synthesized in Ar atmosphere. Top spectra in figure 16 shows the background-including spectra and they do not show any differences in

sight. Bottom spectra in figure 16 shows the background-subtracted spectra and they show no peaks around -50 to 300 ppm. When we check the carbon solubility in silicates with CMAS silicate glasses, the analysis data show that around 100 ppm of carbon dioxide was dissolved in the system. We do not perform the same analysis on the CaO-SiO₂ binary system samples; however it is thought to around 100 ppm of carbon dioxide are presented in this system, too. CaSiO₃ sample with CO gas flow was synthesized to find out the equilibrium effect on the solubility and to aim the high carbon-bearing sample.

Figure 17 shows the ¹³C MAS NMR spectrum of carbon-bearing CaSiO₃ sample. The bottom line shows the rotor background signal, the middle line shows the sample and rotor background signal, and the top line shows the background-subtracted signal. There were impurities in the CaSiO₃ sample which come from the graphite crucible during the sample pickup. Broad peak around 110 ppm is different from sp² or sp³ carbon peak in amorphous carbon ¹³C MAS NMR. Graphite oxides show the peak around 110 ppm in anisotropic chemical shift (Casabianca, Shaibat et al. 2010) and graphite shows the peaks around 100 ppm (Jiang, Solum et al. 2002; Si and Samulski 2008); therefore this peak is assigned to graphite. Further studies are necessary to investigate the atomic environments of carbon in the silicate glasses after picking up the impurities.

Figure 18 shows the ^{13}C MAS NMR spectrum of carbon-bearing CaO-B₂O₃ system. The peak around 110 ppm is assigned to graphite impurities and the peak around 270 ppm is thought to be the four coordinated carbon in calcium borate glasses which have 33 % of four coordinated boron in the whole boron environments. Quantum chemical calculations in section 3 suggests that the four coordinated carbon substituted Si in Si tetrahedron shows the NMR chemical shifts around 254 ppm and NMR chemical shifts are mainly influenced by first nearest neighborhood atoms. This spectrum shows the possibility of presence of the four coordinated carbon in oxides and it would be the first experimental evidence of the sp³ hybridized carbon if the peak around 270 ppm is reproducible and real peak from the carbon species in the calcium borate glasses. Solubility of carbon in CaO:B₂O₃ ratio of 39.7:60.3 in mole percent is approximately 1000 ppm (Park and Min 1999; Jung 2006). Configurational enthalpy of borosilicate is positive which means that mixing of boron and silicon is difficult (Lee, Kim et al. 2010); however in somehow we make the carbon-bearing borosilicate we may see the four coordinated carbon in tetrahedral site in silicate glasses.

Carbonatite is igneous rock which contains more than 50 vol.% of carbonate minerals (Philpotts and Ague 2009). When the rock contains more than 10 vol.% of silicate mineral, the rock is classified as carbonate mineral bearing silicate rock (Philpotts and Ague 2009). Carbonatite have

notably high concentration of Trace element like Nb, Sr, Th and rare earth elements. After 1950s it is known that Nb can exist as many as 0.4 % in carbonatites, so it has been used as a source rock of trace elements and rare earth elements. They are much more dissolved in alkali magma and the partitioning between silicate melts and carbonatite melts make these elements dissolved into carbonatite melts. Pyrochlore is the mineral which contains Nb and is characteristically found in carbonatite(Bell 1989). In some study, Nb is especially low in silicate melts which have high concentration of other rare earth elements (Solovova, Girnits et al. 2008).

The solubility of trace and rare earth elements are dependent on the amount of carbon species in the melts. That means if we can connect those two parameters, the solubility of CO₂ in primordial magma is inferred from the residue of trace and rare earth elements in the erupted magma. Experimental data of CO₂ solubility in the natural sample are always less than that in the primordial magma because of degassing. Trace and rare earth elements have the key to presume the solubility of CO₂ interior of the Earth. This makes it more important to understand the atomistic structure of carbon in the silicates and atomistic sites of carbon species in the silicates.

5. Future studies

To understand the pressure effect on carbon solubility and structure of carbon in silicate crystals, further high-pressure experiment is needed up to at least 24 GPa because phase transition occurs at 24 GPa for MgSiO_3 from spinel to perovskite. Shcheka et al. (2006) expected that the ratio of CO_2 in the whole carbon solubility in depth will increase as the pressure increases until 24 GPa and rapidly decreases above 24 GPa due to the phase transition of minerals. However, this is a speculation from the extrapolation of solubility of carbon in silicate minerals which were synthesized under 15 GPa. The synthesis of high pressure sample will be collaborated with Dr. Fei.

Peak assignment for ^{13}C MAS NMR spectra of CaSiO_3 with CO flow is necessary and after picking up the impurities such as graphite particles from the graphite crucible, high resolution ^{13}C MAS NMR will be performed again. To enhance the amount of carbon species in the silicate glasses, pre-mixed powder samples were sent to Dr. Fei in November 2010 to synthesize the high pressure carbon-bearing silicate glasses.

To identify the peak around 270 ppm in carbon-bearing $\text{CaO-B}_2\text{O}_3$ glasses, ^{13}C MAS NMR study for rotor background and carbon-bearing $\text{CaO-B}_2\text{O}_3$ glasses will be performed again. If the 270 ppm peak still exists,

it would be the first experimental results of four coordinated carbon in oxide glasses.

6. Remaining questions

There is ambiguity whether only fluid inclusions were removed by decrepitation experiment or unstable four coordinated carbon in Si tetrahedron could be removed together if it exists. I still do not understand the key factors of the stability of fluid inclusions and how they control the stability of fluid inclusions. If the pressure is one of the key factors, I wonder if the stability of fluid inclusions decreases when it comes back to 1 atm system after pressuring conditions.

7. Conclusion

Atomistic origins of carbon in binary silicate systems are the major object of this study. Carbon solubility in crystalline silicate and non-crystalline silicate is small in 1 atm system. To find the better experimental conditions to detect the carbon speciation in the silicates with NMR, first the previous studies are summarized. Previous studies show that carbon solubility in silicate melts increases as the pressure increases, temperature

decreases, weight percent of silicate decreases, the fraction of NBO increases, the cations like Ca^{2+} and Mg^{2+} increase. The composition of silicate crystal is decided to MgSiO_3 , which can represent the model mineral of the mantle, and that of silicate glass is decided to the eutectic composition of CaO and SiO_2 .

^{13}C NMR spectra for carbon-bearing MgSiO_3 show that there is dissolved CO, carbonate ion, and gas phase CO_2 or four-coordinated carbon. To confirm the atomic environments of 126 ppm peak deprecation experiment and quantum chemical calculations are performed.

^{13}C NMR spectra for Carbon-bearing CaSiO_3 and CaO-SiO_2 eutectic composition show the no meaningful peaks from carbon. It is thought to be due to low solubility of carbon and ^{13}C isotope in the glasses. ^{13}C NMR spectrum for Carbon-bearing $\text{CaO-B}_2\text{O}_3$ glasses show the peak at 270 ppm which is thought to be the presence of four coordinated carbon substituted boron in BO_4 units.

Reference

- Alam, T. M., T. A. Friedmann, et al. (2002). Solid State ^{13}C MAS NMR Investigations of Amorphous Carbon Thin Films Structural Changes During Annealing. Thin Films: Preparation, Characterization, Applications. J. S. M. P. Soriaga, L. A. Bottomley and Y.-G. Kim. New York, Kluwer: 370.
- Alam, T. M., T. A. Friedmann, et al. (2003). "Low temperature annealing in tetrahedral amorphous carbon thin films observed by C-13 NMR spectroscopy." Phys. Rev. B **67**(24).
- Angel, R. J., A. Chopelas, et al. (1992). "Stability of high-density clinoenstatite at upper-mantle pressures." Nature **358**(6384): 322-324.
- Behrens, H. and F. Gaillard (2006). "Geochemical Aspects of Melts: Volatiles and Redox Behavior." Elements **2**: 275-280.
- Bell, K., Ed. (1989). Carbonatites: genesis and evolution. Carbonatites: Momenclature, Average Chemical Compositions, and Element Distribution. London, Unwin Hyman Ltd.
- Berryman, R. A. and I. D. Sommerville (1992). "Carbon Solubility as Carbide in Calcium Silicate Melts." Metal. Trans. B **23**(2): 223-227.
- Biellmann, C., P. Gillet, et al. (1993). "Experimental evidence for carbonate stability in the Earth's lower mantle." Earth Planet. Sci. Lett. **118**: 31-41.
- Blank, J. G. and R. A. Brooker (1994). Experimental Studies of Carbon Dioxide in Silicate Melts: Solubility, Speciation, and Stable Carbon Isotope Behavior. Volatiles in Magmas. M. R. Carroll and J. R. Holloway. **30**.
- Blank, J. G., E. M. Stolper, et al. (1993). "Solubilities of Carbon-dioxide and Water in Rhyolitic melt at 850-Degrees-C and 750 Bars." Earth Planet. Sci. Lett. **119**(1-2): 27-36.
- Bouhifd, M. A., A. P. Jephcoat, et al. (2008). "Argon solubility drop in silicate melts at high pressures: A review of recent experiments." Chem. Geol. **256**(3-4): 252-258.

- Brearley, M. and A. Montana (1989). "The Effect of CO₂ on the Viscosity of Silicate Liquids at High-Pressure." Geochim. Cosmochim. Acta **53**(10): 2609-2616.
- Brey, G. (1976). "CO₂ Solubility and Solubility Mechanisms in Silicate Melts at High-Pressures." Contrib. Mineral. Petrol. **57**(2): 215-221.
- Brooker, R. A., S. C. Kohn, et al. (2001). "Structural controls on the solubility of CO₂ in silicate melts Part I: bulk solubility data." Chem. Geol. **174**(1-3): 225-239.
- Brooker, R. A., S. C. Kohn, et al. (2001). "Structural controls on the solubility of CO₂ in silicate melts Part II: IR characteristics of carbonate groups in silicate glasses." Chem. Geol. **174**(1-3): 241-254.
- Brooker, R. A., S. C. Kohn, et al. (1999). "Solubility, speciation and dissolution mechanisms for CO₂ in melts on the NaAlO₂-SiO₂ join." Geochim. Cosmochim. Acta **63**(21): 3549-3565.
- Bureau, B., G. Silly, et al. (1999). "From crystalline to glassy gallium fluoride materials: an NMR study of Ga-69 and Ga-71 quadrupolar nuclei." Solid State Nucl. Magn. Reson. **14**(2): 181-190.
- Casabianca, L. B., M. A. Shaibat, et al. (2010). "NMR-Based Structural Modeling of Graphite Oxide Using Multidimensional ¹³C Solid-State NMR and ab Initio Chemical Shift Calculations." Journal of the American Chemical Society **132**(16): 5672-5676.
- Eggler, D. H., B. O. Mysen, et al. (1979). "Solubility of Carbon-monoxide in Silicate Melts at High-pressures and Its Effect on Silicate Phase-relations." Earth Planet. Sci. Lett. **43**(2): 321-330.
- Fine, G. and E. Stolper (1985). "The Speciation of Carbon-dioxide in Sodium Aluminosilicate Glasses." Contrib. Mineral. Petrol. **91**(2): 105-121.
- Freund, F., H. Kathrein, et al. (1980). "Carbon in solid solution in forsterite--a key to the untractable nature of reduced carbon in terrestrial and cosmogenic rocks." Geochimica et Cosmochimica Acta **44**(9): 1319-1321, 1323-1333.
- Green, D. H., S. M. Eggins, et al. (1993). "The other carbon cycle." Nature **365**: 210-211.
- Helo, C., M.-A. Longpre, et al. (2011). "Explosive eruptions at mid-ocean ridges driven by CO₂-rich magmas." Nat. Geosci. **4**: 260-263.

- Holloway, J. R. and J. G. Blank (1994). Application of Experimental Results to C-O-H Species in Natural Melts. Volatiles in Magmas. Washington, Mineralogical Soc America. **30**: 187-230.
- Hugh-Jones, D. A. and R. J. Angel (1994). "A compressional study of MgSiO₃ orthoenstatite up to 8.5 GPa." Am. Mineral. **79**: 405-410.
- Huijgen, W. J. J. and R. N. J. Comans (2005). "Mineral CO₂ Sequestration by Steel Slag Carbonation." Environ. Sci. Technol. **39**(24): 9676-9682.
- Jambon, A. (1994). Earth Degassing and Large-Scale Geochemical Cycling of Volatile Elements. Volatiles in Magmas. Washington, Mineralogical Soc America. **30**: 479-517.
- Jiang, Y. J., M. S. Solum, et al. (2002). "A New Method for Measuring the Graphite Content of Anthracite Coals and Soots." Energy & Fuels **16**(5): 1296-1300.
- Jung, I. H. (2006). "Thermodynamic modeling of gas solubility in molten slags (I) - Carbon and nitrogen." ISIJ Int. **46**(11): 1577-1586.
- Jung, W. S., C. Park, et al. (2003). "Probing the nitrogen deficiency in gallium nitride by Ga-71 magic-angle spinning NMR spectroscopy." Bull. Korean Chem. Soc. **24**(7): 1011-1013.
- Kalinkin, A. (2009). "Kinetics of carbon dioxide chemisorption by Ca-containing silicates." J. Therm. Anal. Calorim. **95**(1): 105-110.
- Keppler, H., M. Wiedenbeck, et al. (2003). "Carbon solubility in olivine and the mode of carbon storage in the Earth's mantle." Nature **424**(6947): 414-416.
- Kerrick, D. M. and J. A. D. Connolly (2001). "Metamorphic devolatilization of subducted oceanic metabasalts: implications for seismicity, arc magmatism and volatile recycling." Earth Planet. Sci. Lett. **189**: 19-29.
- King, P. L. and J. R. Holloway (2002). "CO₂ solubility and speciation in intermediate (andesitic) melts: the role of H₂O and composition." Geochim. Cosmochim. Acta **66**(9): 1627-1640.
- Kohn, S. C., R. A. Brooker, et al. (1991). "C-13 MAS NMR - A Method for Studying CO₂ Speciation in Glasses." Geochim. Cosmochim. Acta **55**(12): 3879-3884.

- Kohn, S. C., R. Dupree, et al. (1989). "A Multinuclear Magnetic-Resonance Study of the Structure of Hydrous Albite Glasses." Geochim. Cosmochim. Acta **53**(11): 2925-2935.
- Kubicki, J. D. and E. M. Stolper (1995). "Structural Roles of CO₂ and CO₃²⁻ in Fully Polymerized Sodium Aluminosilicate Melts and Glasses." Geochim. Cosmochim. Acta **59**(4): 683-698.
- Lee, S. K., H. N. Kim, et al. (2010). "Nature of Chemical and Topological Disorder in Borogermanate Glasses: Insights from B-11 and O-17 Solid-State NMR and Quantum Chemical Calculations." J. Phys. Chem. B **114**(1): 412-420.
- Lee, S. K., S. B. Lee, et al. (2009). "Structure of Amorphous Aluminum Oxide." Phys. Rev. Lett. **103**(9).
- Luth, R. W. (2003). Mantle Volatiles--Distribution and Consequences. Treatise on Geochemistry. D. H. Heinrich and K. T. Karl. Oxford, Pergamon: 319-361.
- Macias, A., A. Kindness, et al. (1997). "Impact of carbon dioxide on the immobilization potential of cemented wastes: Chromium." Cement Concrete Res. **27**(2): 215-225.
- Massiot, D., I. Farnan, et al. (1995). "Ga-71 and Ga-69 nuclear-magnetic-resonance study of beta-Ga₂O₃ - resolution of 4-fold and 6-fold coordinated Ga sites in static conditions." Solid State Nucl. Magn. Reson. **4**(4): 241-248.
- Massiot, D., T. Vosegaard, et al. (1999). "Ga-71 NMR of reference Ga-IV, Ga-V, and Ga-VI compounds by MAS and QPASS, extension of gallium/aluminum NMR parameter correlation." Solid State Nucl. Magn. Reson. **15**(3): 159-169.
- Morizet, Y., M. Paris, et al. (2010). "C-O-H fluid solubility in haplobasalt under reducing conditions: An experimental study." Chem. Geol. **279**: 1-16.
- Mysen, B. O., R. J. Arculus, et al. (1975). "Solubility of Carbon-dioxide in Melts of Andesite, Tholeiite, and Olivine Mephelinite Composition to 30 kbar Pressure." Contrib. Mineral. Petrol. **53**(4): 227-239.
- Mysen, B. O., M. L. Fogel, et al. (2009). "Solution behavior of reduced C-O-H volatiles in silicate melts at high pressure and temperature." Geochim. Cosmochim. Acta **73**(6): 1696-1710.

- Mysen, B. O. and D. Virgo (1980). "The Solubility Behavior of CO₂ in Melts on the Join NaAlSi₃O₈-CaAlSi₃O₈-CO₂ at High-Presssures and Temperatures - A Raman-Spectroscopic Study." Am. Miner. **65**(11-1): 1166-1175.
- Nomura, K., T. Kamiya, et al. (2010). "Comprehensive studies on the stabilities of a-In-Ga-Zn-O based thin film transistor by constant current stress." Thin Solid Films **518**(11): 3012-3016.
- Nowak, M., D. Schreen, et al. (2004). "Argon and CO₂ on the race track in silicate melts: A tool for the development of a CO, speciation and diffusion model." Geochim. Cosmochim. Acta **68**(24): 5127-5138.
- Park, J. H., S. Lee, et al. (2009). "Density of States-Based DC I-V Model of Amorphous Gallium-Indium-Zinc-Oxide Thin-Film Transistors." IEEE Electron Device Letters **30**(10): 1069-1071.
- Park, J. H. and D. J. Min (1999). "Solubility of Carbon in CaO-B₂O₃ and BaO-B₂O₃ Slags." Metall. Mater. Trans. B. **30B**: 1045-.
- Pawley, A. R., J. R. Holloway, et al. (1992). "The Effect of Oxygen Fugacity on the Solubility of Carbon oxygen Fluids in Basaltic Melt." Earth Planet. Sci. Lett. **110**(1-4): 213-225.
- Pearce, M. L. (1964). "Solubility of Carbon Dioxide and Variation of Oxygen Ion Activity in Soda-silicate Melts." J. Am. Ceram. Soc. **47**(7): 342-347.
- Philpotts, A. and J. J. Ague (2009). Principles of Igneous and Metamorphic Petrology, Cambridge University Press.
- Richet, P. and Y. Bottinga (1984). "Anorthite, andesine, wollastonite, diopside, cordierite, and pyrope: thermodynamics of melting, glass transitions, and properties of the amorphous phases." Earth Planet. Sci. Lett. **67**: 415-432.
- Sarda, P. and B. Guillot (2005). "Breaking of Henry's law for noble gas and CO₂ solubility in silicate melt under pressure." Nature **436**(7047): 95-98.
- Shcheka, S. S., M. Wiedenbeck, et al. (2006). "Carbon solubility in mantle minerals." Earth and Planetary Science Letters **245**(3-4): 730-742.
- Shcheka, S. S., M. Wiedenbeck, et al. (2006). "Carbon solubility in mantle minerals." Earth Planet. Sci. Lett. **245**(3-4): 730-742.

- Si, Y. and E. T. Samulski (2008). "Synthesis of Water Soluble Graphene." Nano Letters **8**(6): 1679-1682.
- Solovova, I. P., A. V. Girnis, et al. (2008). "Origin of Carbonatite Magma during the Evolution of Ultrapotassic Basite Magma." Petrology **16**(4): 401-420.
- Stolper, E., G. Fine, et al. (1987). "Solubility of carbon dioxide in albitic melt." Am. Mineral.
- Vosegaard, T., D. Massiot, et al. (1997). "Ga-71 chemical shielding and quadrupole coupling tensors of the garnet $Y_3Ga_5O_{12}$ from single-crystal Ga-71 NMR." Inorg. Chem. **36**(11): 2446-2450.
- Yoon, S. M., S. H. Yang, et al. (2010). "Impact of Interface Controlling Layer of Al_2O_3 for Improving the Retention Behaviors of In-Ga-Zn oxide-based Ferroelectric Memory Transistor." Appl. Phys. Lett. **96**(23).
- Zhang, Y. and A. Zindler (1993). "Distribution and evolution of carbon and nitrogen in Earth." Earth Planet. Sci. Lett. **117**(3-4): 331-345.

Tables

Table 1. Functional property of analytical facilities

Measurements	Raman	IR	NMR	XRD
Source	Monochromic laser	Infrared light	Electromagnetic pulse	X-ray
Method	Inelastic scattering	Absorption	Resonance with external magnetic field and nuclear spin	X-ray diffraction
Detecting Target	Vibrational mode of molecule	Vibrational mode of molecule	Nuclear spin excitation	Crystal structure
Detection Order	Short-range order of atomic structure	Short-range order of atomic structure	Short-range order of atomic structure	Inter-atomic layer distance

Table 2. Calculated isotropic chemical shift of CO₂

Method/ Basis set	Isotropic shielding tensor (σ)	σ_{11}	σ_{22}	σ_{33}	Isotropic chemical shift
HF/6-31G*	74.3815	-29.9204	-29.9204	282.9854	121.9574
HF/ 6-311+G(2d)	52.7114	-62.4767	-62.4767	283.0875	135.7250
UHF/6-31G*	74.3815	-29.9204	-29.9204	282.9854	121.9574
UHF/6- 311+G(2d)	52.7114	-62.4767	-62.4767	283.0875	135.7250
B3LYP/6-31G*	77.0453	-27.0767	-27.0767	285.2894	108.8074
B3LYP/ 6-311+G(2d)	52.3191	-64.4053	-64.4053	285.7680	125.7284

Table A1. T₁ relaxation measurement from micro-imaging NMR

ROI name	ISA_1			ISA_2			ISA_3		
ROI area	0.00598 cm ²			0.00299 cm ²			0.0234 cm ²		
Parameter	value	Std. Dev.	usage	value	Std. Dev.	usage	value	Std. Dev.	usage
Absolute bias	0	0	fixed	0	0	fixed	2676.68	78461.1	varied
Signal intensity	606403	3209.63	varied	-2.09E+06	1.23E+07	varied	109762	77942.2	varied
T ₁ relaxation time (msec)	509.757	4.82943	varied	2.24E+06	1.23E+07	varied	138.2	52.0383	varied
Standard dev. of the fit	2668.9			4185.79			2668.26		
Repetition time (msec)	Mean	Std. Dev.	Func.	Mean	Std. Dev.	Func.	Mean	Std. Dev.	Func.
4000	606123	188388	606166	141390	26847.5	146149	110373	45107.0	112439
3000	610456	185941	604717	153237	25935.7	146149	112772	43142.9	112439
2000	589368	182167	594412	142722	22984.9	146149	116630	45379.8	112439
1000	517101	148075	521133	147453	27004.5	146149	111898	44051.0	112360
600	424552	108059	419514	145007	24907.6	146142	107620	42176.9	111010
400	327396	76093	329724	147970	26628.1	145651	108756	38777.2	106366
300	270036	58795	269758	141580	25054.8	142072	98915	36091.6	99916
250	235253	52070	235064	134529	21832.7	134484	94629	33650.1	94458

Table A2. NMR chemical shift, quadrupolar coupling, and asymmetric parameter η of Ga species, as reported in previous studies of ^{71}Ga NMR

Composition	Sample Type †	Spinning Speed (kHz)	Field Strength (T)	Functional Group	Chemical Shift (ppm)	C_Q (MHz)	η_Q	Ref
$\alpha\text{-Ga}_2\text{O}_3$	p	15	14.1	^{61}Ga	52	8.16	0	[01]
$\beta\text{-Ga}_2\text{O}_3$	p	15	14.1	^{43}Ga	201	11.1	0.85	[01]
$\beta\text{-Ga}_2\text{O}_3$	p	15	14.1	^{61}Ga	41	8.34	0.1	[01]
$\beta\text{-Ga}_2\text{O}_3$	p	12.5	11.7	^{61}Ga	50	-	-	[02]
$\beta\text{-Ga}_2\text{O}_3$	p	static	11.7	^{43}Ga	220	-	-	[02]
$\gamma\text{-Ga}_2\text{O}_3$	p	31	17.6	^{61}Ga	50	-	-	[03]
$\gamma\text{-Ga}_2\text{O}_3$	p	31	17.6	^{53}Ga	20	-	-	[03]
$\gamma\text{-Ga}_2\text{O}_3$	p	31	17.6	^{43}Ga	110	-	-	[03]
$\delta\text{-Ga}_2\text{O}_3$	p	15	14.1	^{61}Ga	52	8.5	0	[01]
$\delta\text{-Ga}_2\text{O}_3$	p	15	14.1	^{43}Ga	210	7	0	[01]
$\text{Y}_3\text{Ga}_5\text{O}_{12}$ Garnet	s	-	9.4	^{43}Ga	220	13.1	0.05	[04]
$\text{Y}_3\text{Ga}_5\text{O}_{12}$ Garnet	s	-	9.4	^{43}Ga	220	4.1	0.03	[04]
MgGa_2O_4 spinel	p	10	9.4	^{43}Ga	171	7.6	0.5*	[05]
MgGa_2O_4 spinel	p	10	9.4	^{61}Ga	74	7.6	0.5*	[05]
$\text{LaGaGe}_2\text{O}_7$	p	static	7.0, 9.4 11.7	^{53}Ga	75.8	15	0.7	[05]
$\text{Ca}_2\text{Ga}_2\text{SiO}_7$ gehlenite	p	10	9.4	^{43}Ga	233	>13.5	0.6 ~ 0.8	[05]

Sn:Ga:Zn:Al:O = 0.5:3.3:1.7:34.7:59.8	P	30	18.8	⁶⁷ Ga	30	12*	-	[06]
		30	18.8	⁶⁹ Ga	200	12*	-	[06]
GaPO ₄ cristoballite	p	static	7.0, 9.4, 11.7	⁶⁷ Ga	118	4.7	0.45	[05]
	p	15	17.6	⁶⁷ Ga (1)	-61.3	6.4		[07]
GaPO ₄ cristobalite	p	15	17.6	⁶⁷ Ga (2)	-68.6	2.8		[07]
	p	15	17.6	⁶⁷ Ga (3)	-64.2	4.5		[07]
GaPO ₄ quartz	p	15	18.8	⁶⁷ Ga	111	8.5	0.45	[07]
GaPO ₄ quartz	p	15	18.8	⁶⁷ Ga	100.3	8.6	0.51	[05]
Ga(OH)(O ₃ PC ₂ H ₄ - CO ₂ H)	p	10	9.4	⁶⁷ Ga	23	9.3	0.1	[05]
	p	10	9.4	⁶⁷ Ga	48	14.3	0.57	[05]

† p: crystalline power, s: single crystal, a: amorphous

* : fixed value

- [01] Bradely et al., 1993, Magn. Reson. Chem.
- [02] Massiot et al., 1995, Solid State Nucl. Magn. Reson.
- [03] Vosegarrd et al., 1997, Inorg. Chem.
- [05] Massiot et al., 1999, Solid State Nucl. Magn. Reson.
- [06] Massiot et al., 2000, Solid State Nucl. Magn. Reson.
- [07] Jung et al., 2003, Bull. Korean Chem. Soc.
- [08] Areat et al., 2005, Anorg. Allg. Chem
- [09] Montouillout et al., 2006, Magn. Reson. Chem.
- [10] O'Dell et al., 2007, Appl. Magn. Reson.

Figures

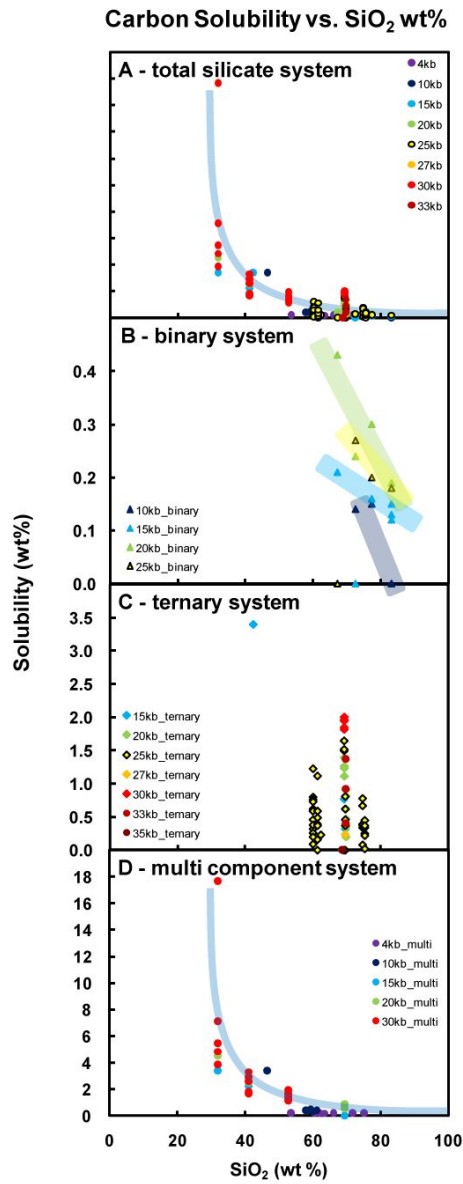


Figure 1 | Carbon solubility in silicate melts as a function of SiO₂ wt%. (A) Carbon solubility for the whole reference system. (B) Carbon solubility for the Na₂O-SiO₂ binary system. (C) Carbon solubility for the Na₂O-Al₂O₃-SiO₂ ternary system. (D) Carbon solubility for the multicomponent system.

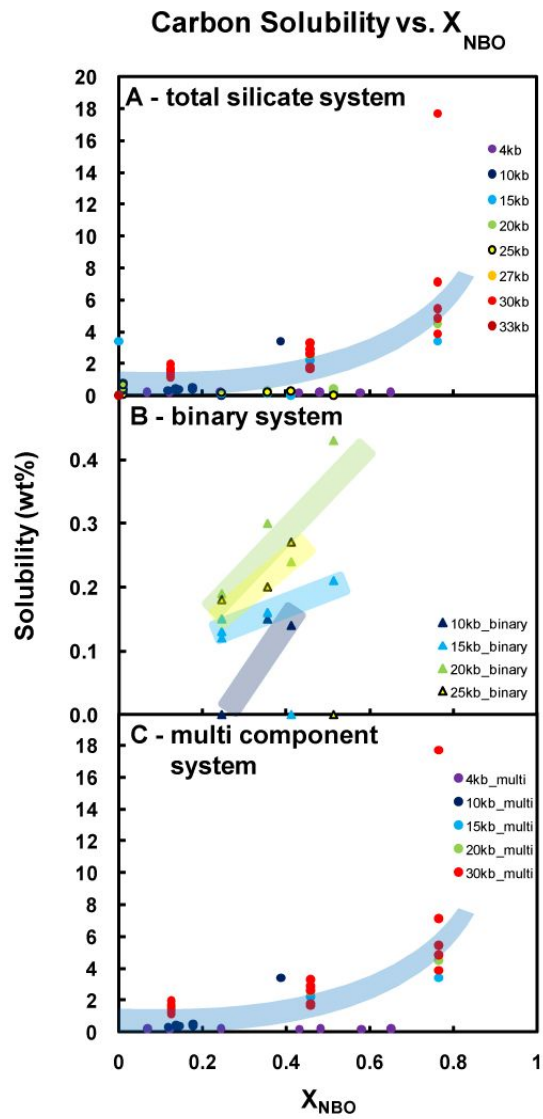


Figure 2 | Carbon solubility in silicate melts as a function of mole fraction of non-bridging oxygen (NBO). (A) Carbon solubility for the whole reference system. (B) Carbon solubility for the $\text{Na}_2\text{O-SiO}_2$ binary system. (C) Carbon solubility for the multi-component system.

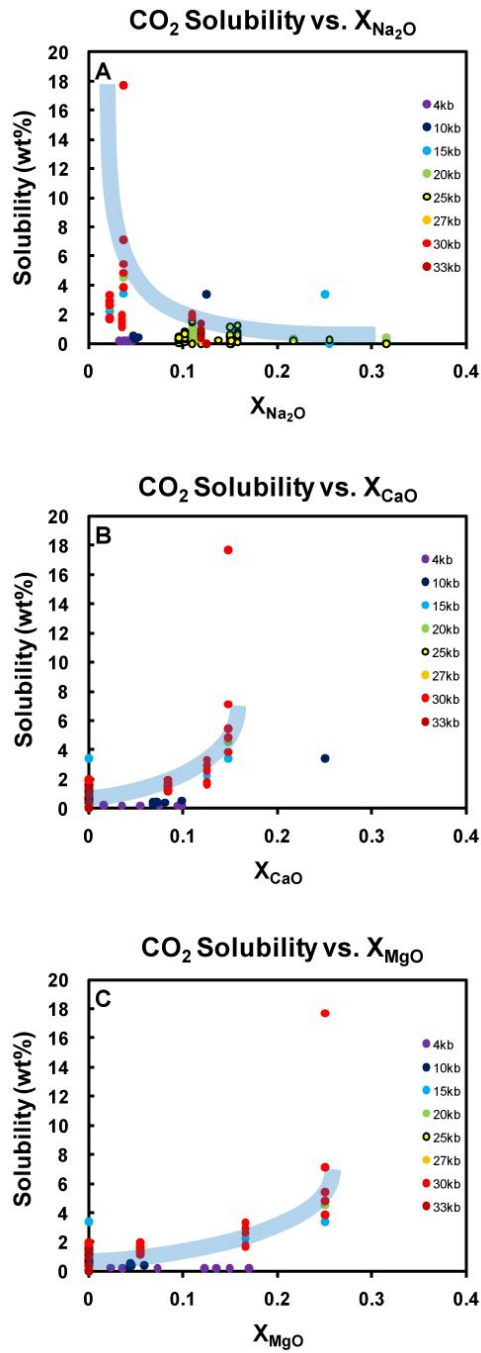


Figure 3 | Carbon solubility in silicate melts as a function of mole fraction of cations. (A) Carbon solubility as a function of mole fraction of Na₂O. (B) Carbon solubility as a function of mole fraction of CaO. (C) Carbon solubility as a function of mole fraction of MgO.

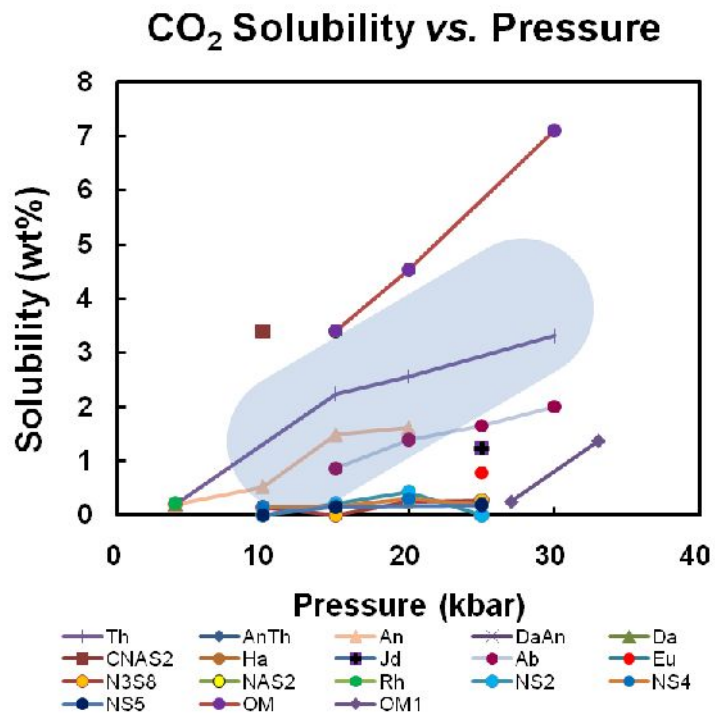


Figure 4 | Carbon solubility in silicate melts as a function of pressure. The upper limit of carbon solubility increases as increasing the pressure.

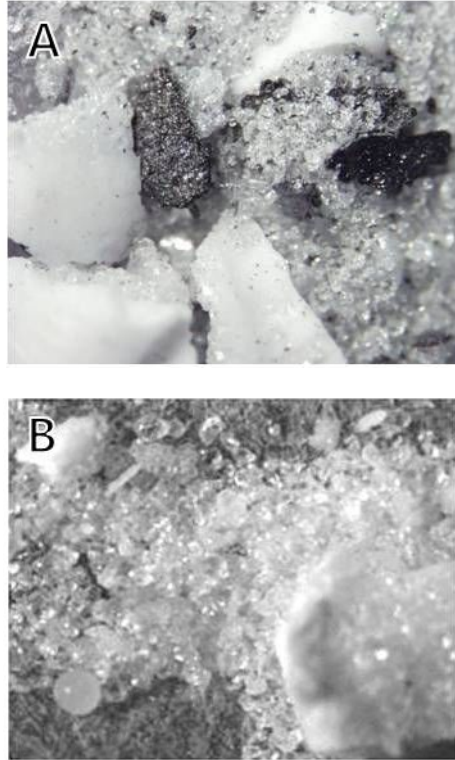


Figure 5 | Pictures of MgSiO_3 with 2.4 wt% amorphous carbon synthesized at 1.5 GPa in 1400°C for 48 hours. Figure 5A shows a first synthesized sample which has more impurities as-received and figure 5B shows a second synthesized sample which has relatively less impurities as-received. White grains in the picture are MgSiO_3 enstatite crystal, and black grains are compressed amorphous carbon.

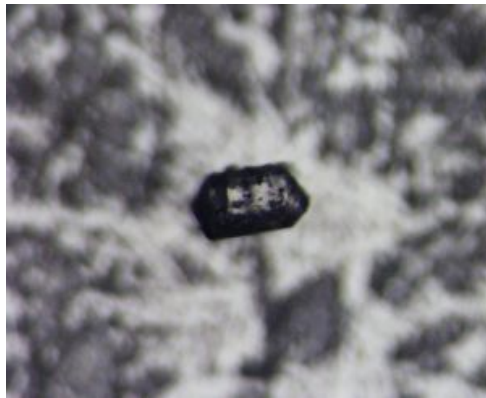


Figure 6 | A picture of an MgSiO_3 grain with 2.4 wt% amorphous carbon synthesized at 1.5 GPa in 1400°C for 48 hours.

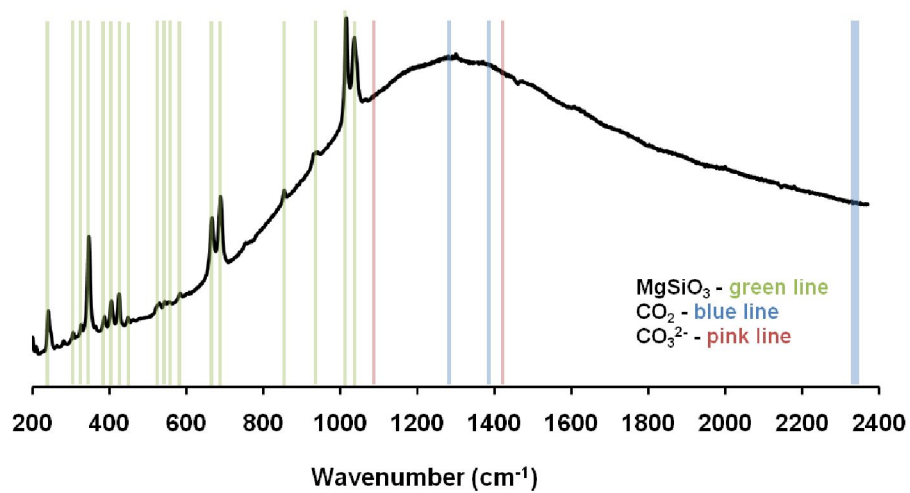


Figure 7 | Raman spectrum for crystalline MgSiO₃ with 2.4 wt% amorphous carbon at 1.5 GPa. The green, blue, and pink lines refer to the vibrational modes for crystalline MgSiO₃, gas phase CO₂, and CO₃²⁻ ion, respectively.

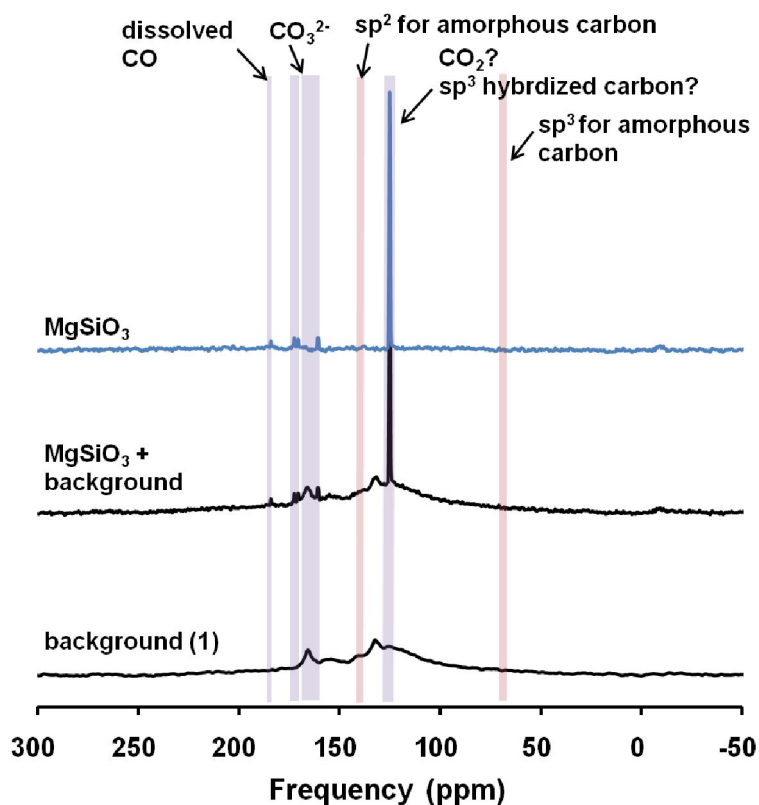


Figure 8 | One-dimensional ^{13}C MAS NMR spectrum of MgSiO_3 with 2.4 wt% amorphous carbon. The bottom line refers to spectral features for rotor backgrounds, the middle line refers to spectral features for rotor and carbon-bearing MgSiO_3 , and the top line refers to spectra features for carbon-bearing MgSiO_3 , background-subtracted. The number in the bracket means the number of spacers used to collect the NMR signal from the sample.

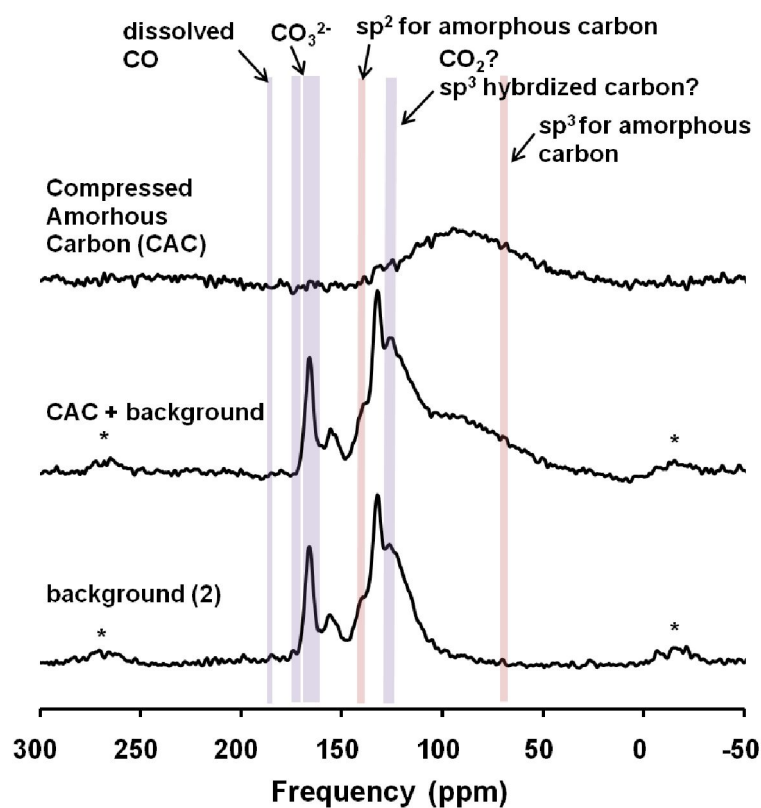


Figure 9 | One-dimensional ^{13}C MAS NMR spectrum of compressed amorphous carbon. The bottom line refers to spectral features for rotor backgrounds, the middle line refers to spectral features for rotor and compressed amorphous carbon, and the top line refers to spectra features for compressed amorphous carbon, background-subtracted. The number in the bracket means the number of spacers used to collect the NMR signal from the sample. An asterisk refers to spinning sidebands.

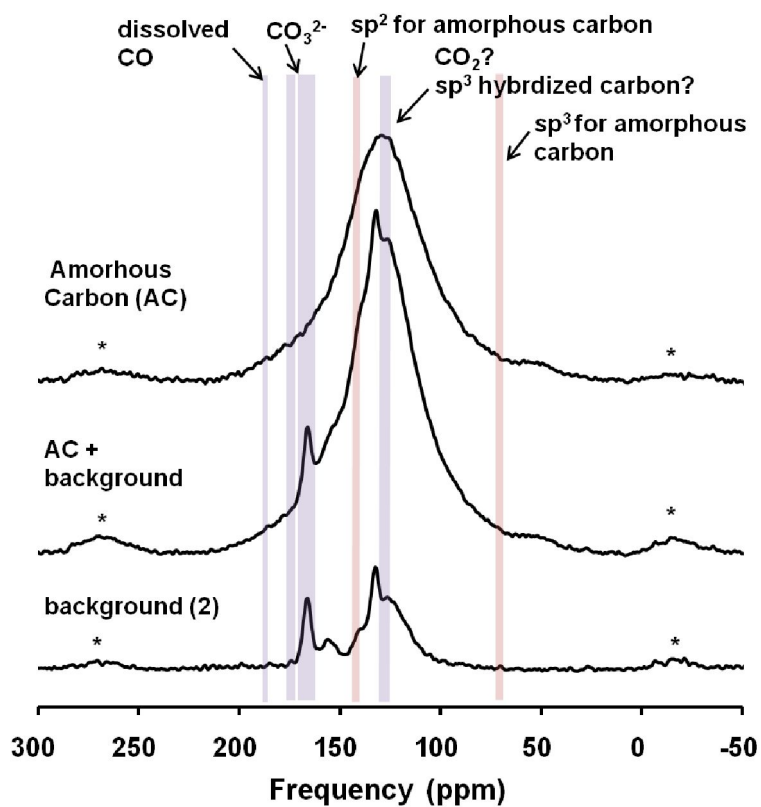


Figure 10 | One-dimensional ^{13}C MAS NMR spectrum of amorphous carbon.

The bottom line refers to spectral features for rotor backgrounds, the middle line to spectral features for rotor and amorphous carbon, and the top line to spectra features for background-subtracted amorphous carbon. The number in the bracket means the number of spacers used to collect the NMR signal from the sample. An asterisk refers to spinning sidebands.

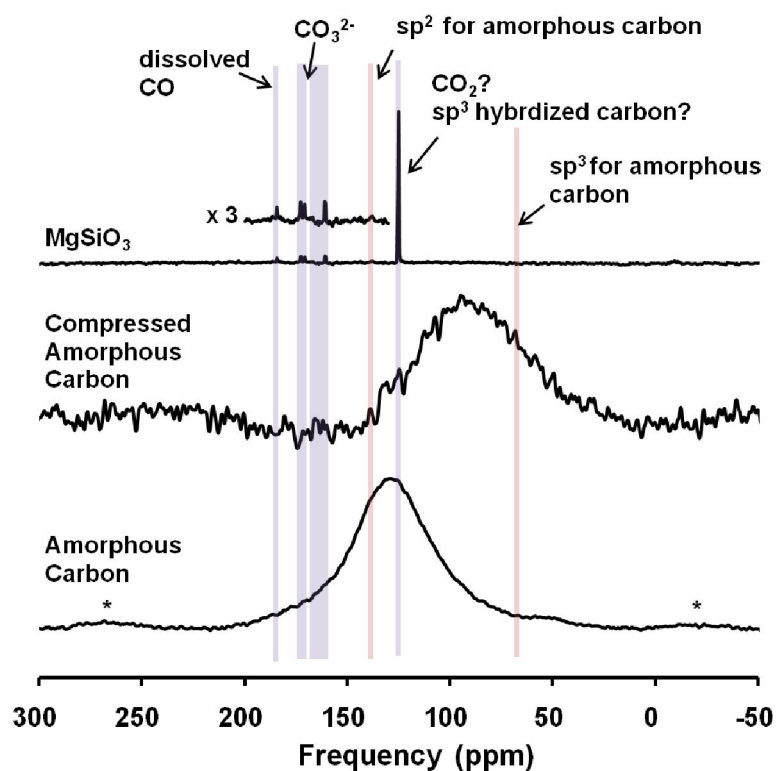


Figure 11 | One-dimensional ^{13}C MAS NMR spectra of MgSiO_3 with 2.4% amorphous carbon, compressed amorphous carbon, and amorphous carbon. The rotor backgrounds were subtracted from the spectra. An asterisk refers to spinning sidebands.

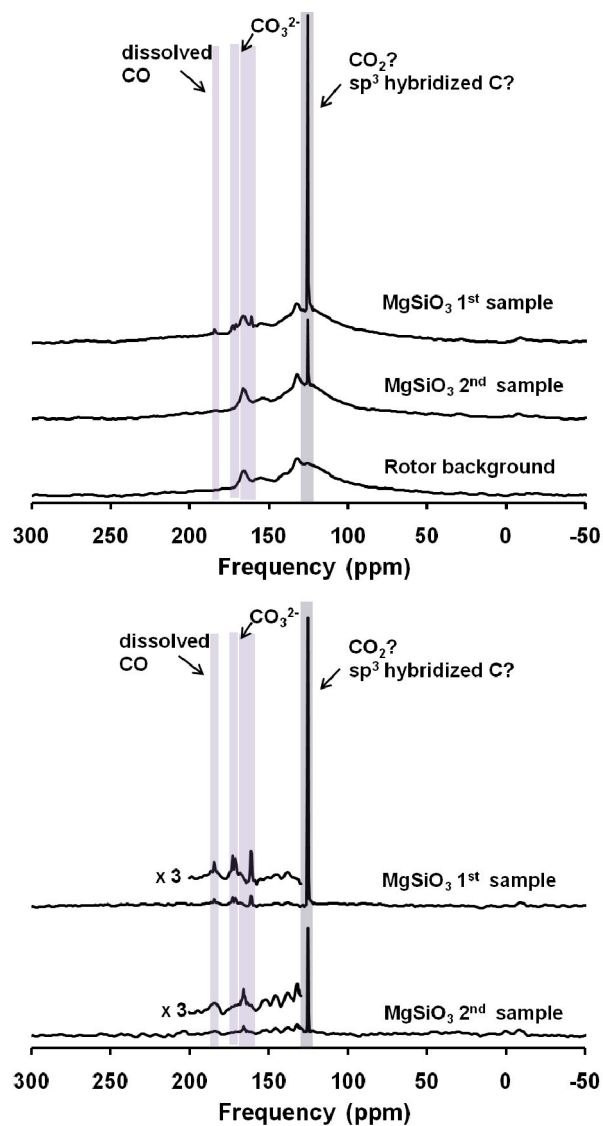


Figure 12 | One-dimensional ^{13}C MAS NMR spectra of firstly and secondly synthesized MgSiO_3 with 2.4 wt% amorphous carbon. (top) Background-included spectra. (bottom) Background-subtracted and weight-normalized spectra.

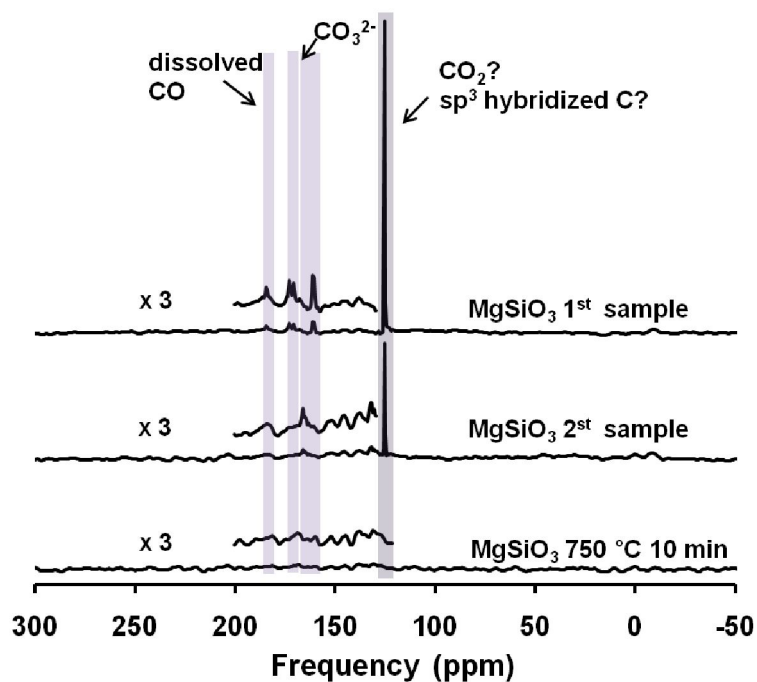


Figure 13 | One-dimensional ^{13}C MAS NMR spectra of MgSiO_3 with 2.4 wt% amorphous carbon and MgSiO_3 heated at 750 °C for 10 minutes. The rotor backgrounds were subtracted from the original spectra and the spectra were weight-normalized.

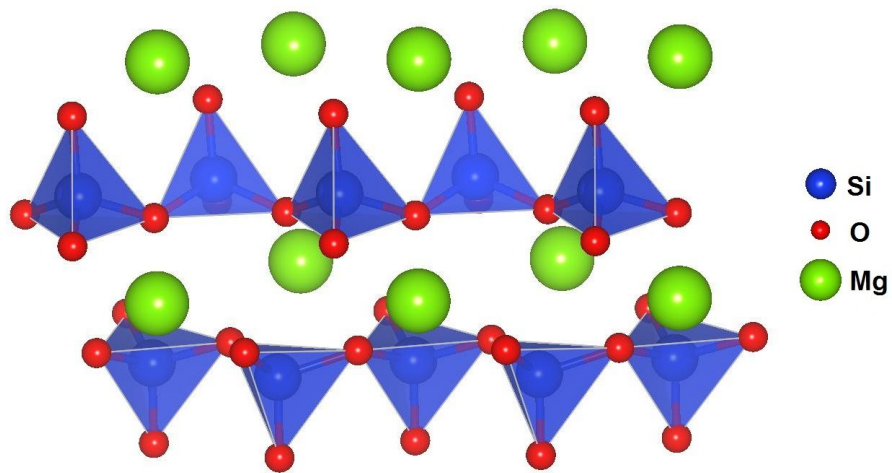


Figure 14 | Atomic structure of MgSiO_3 , ortho-enstatite.

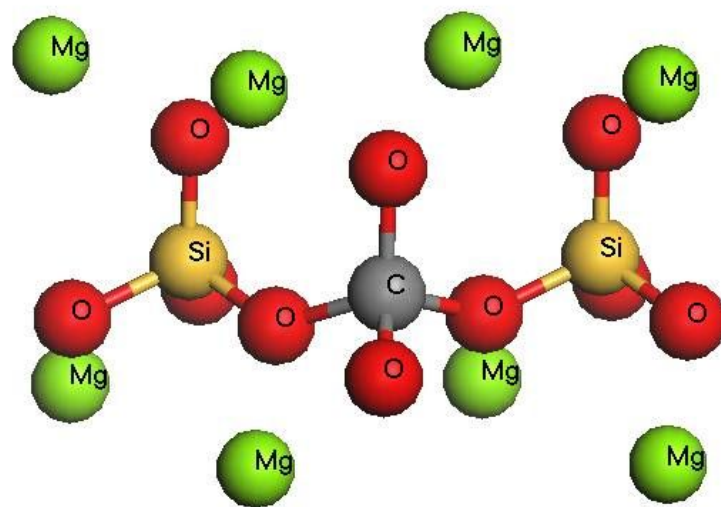


Figure 15 | A model cluster for simulating carbon-substituted MgSiO₃.

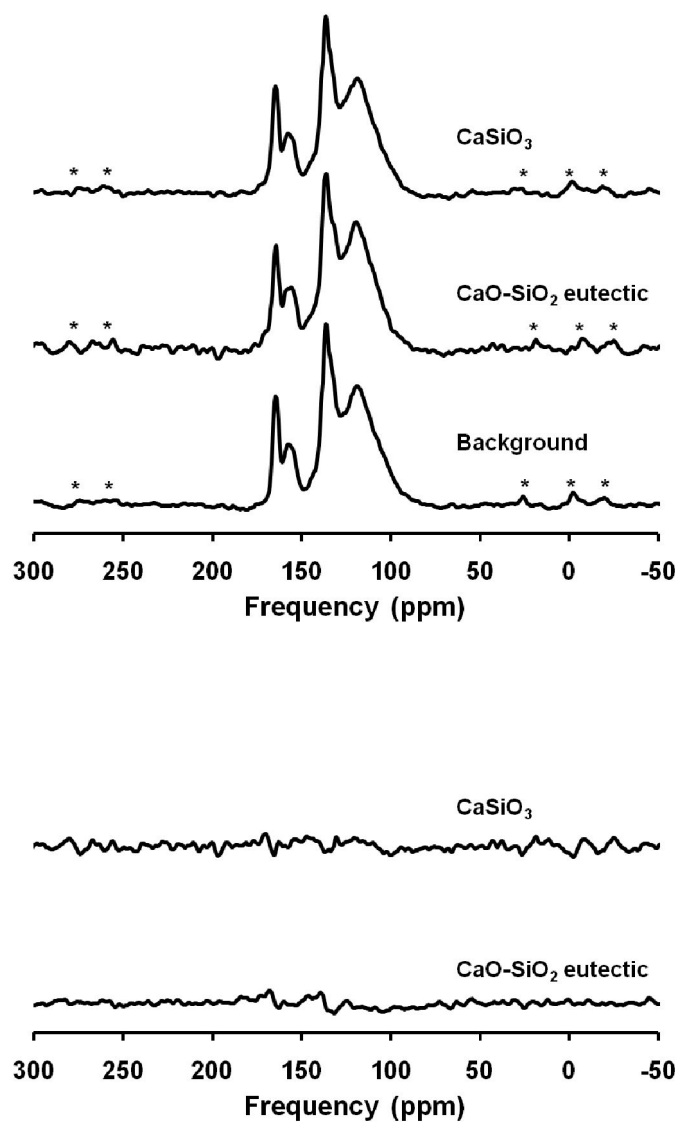


Figure 16 | One-dimensional ^{13}C MAS NMR spectra of carbon-bearing CaSiO_3 and carbon-bearing CaO-SiO_2 eutectic composition synthesized in CO gas flow at 1 atm. (top) Background-included spectra. (bottom) Background-subtracted spectra. An asterisk refers to spinning sidebands.

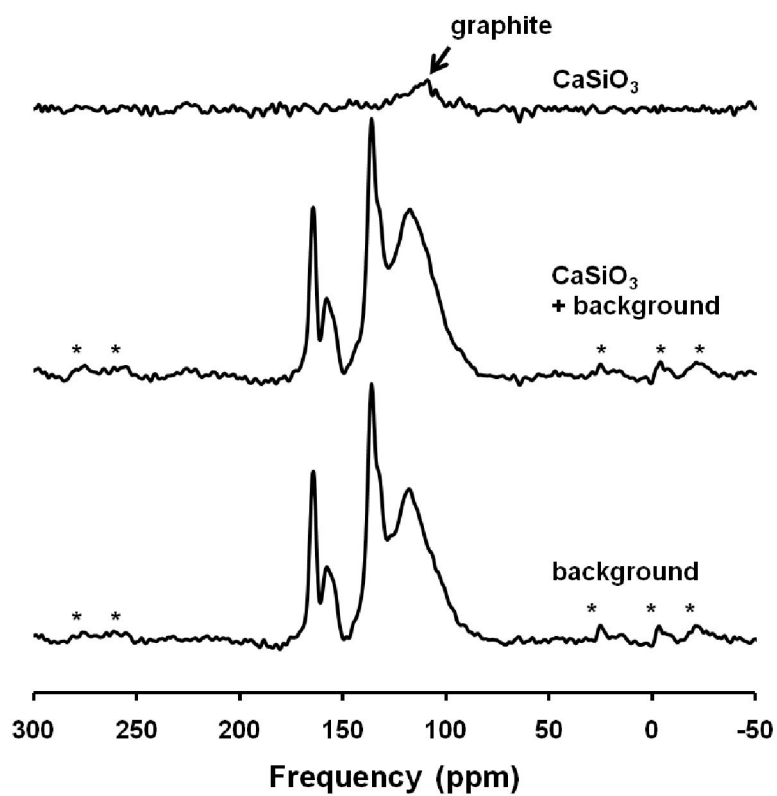


Figure 17 | One-dimensional ^{13}C MAS NMR spectra of carbon-bearing CaSiO_3 synthesized in CO gas flow at 1 atm. An asterisk refers to spinning sidebands.

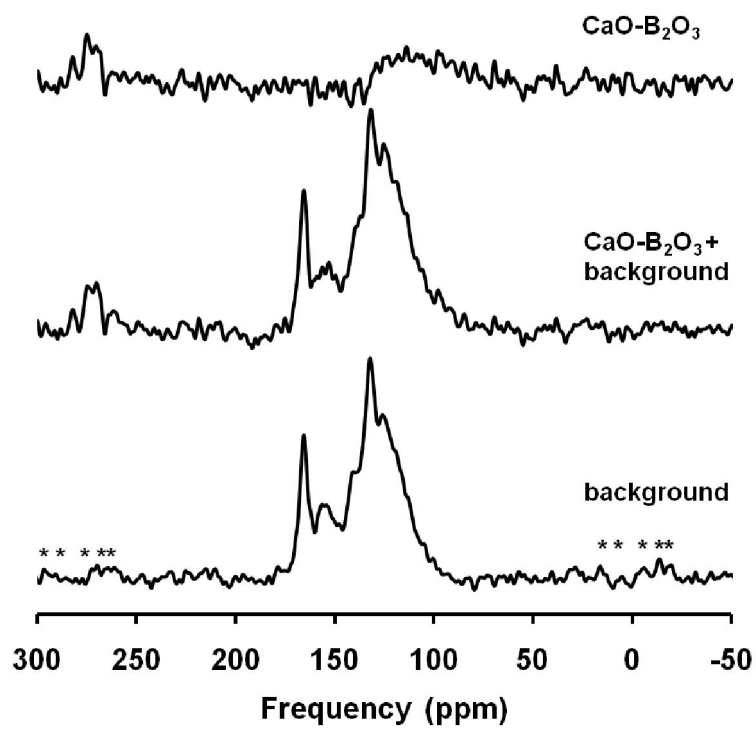


Figure 18 | One-dimensional ^{13}C MAS NMR spectra of carbon-bearing $\text{CaO-B}_2\text{O}_3$ synthesized in CO gas flow at 1 atm. An asterisk refers to spinning sidebands.

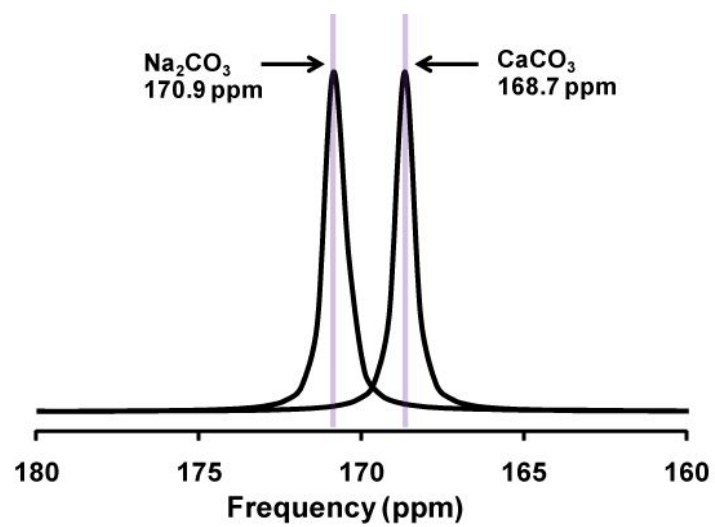


Figure A1 | ^{13}C MAS NMR spectra of CaCO_3 and Na_2CO_3 . The spectra are obtained from T_1 relaxation time measurements and the intensity is normalized to its maximum.

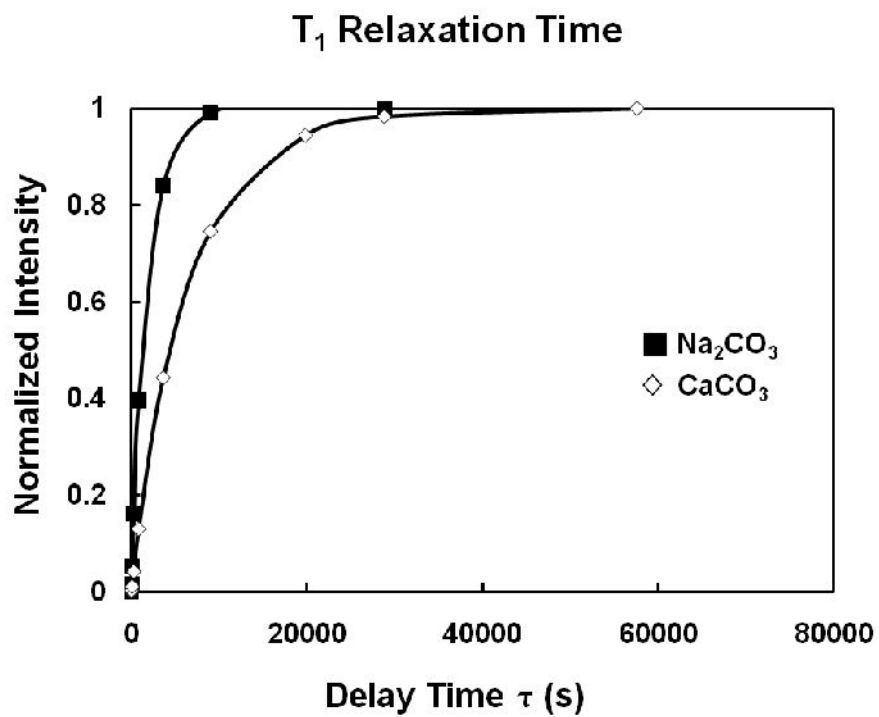


Figure A2 | Normalized maximum intensity of ^{13}C NMR spectra for CaCO_3 and Na_2CO_3 as a function of delay time (s). Na_2CO_3 shows shorter T_1 relaxation time than CaCO_3 .

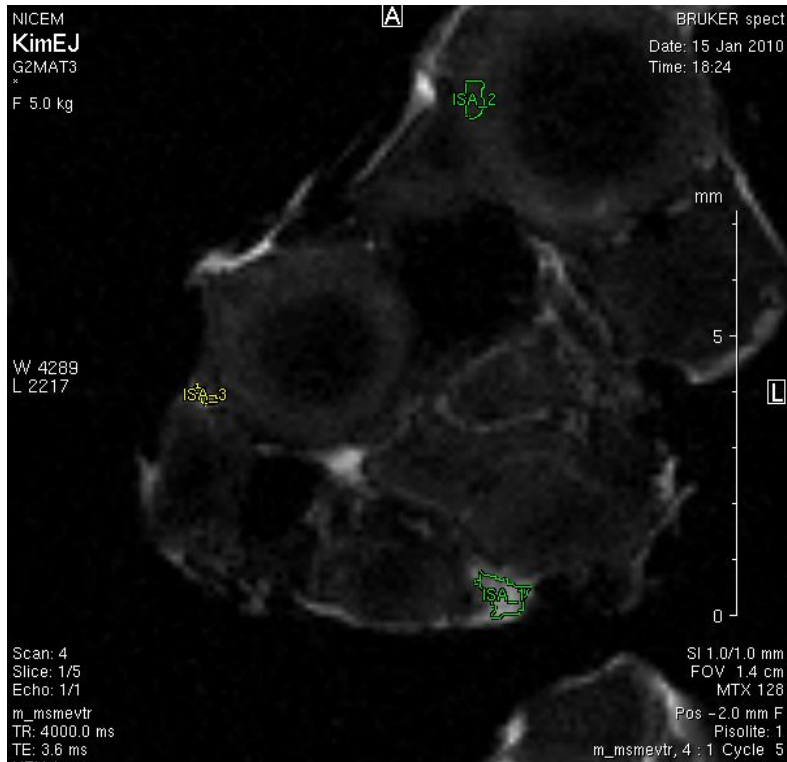


Figure A3 | Micro-NMR Imaging of pisolite. The selected areas are where we measure the T_1 relaxation time of water absorbed into pisolite.

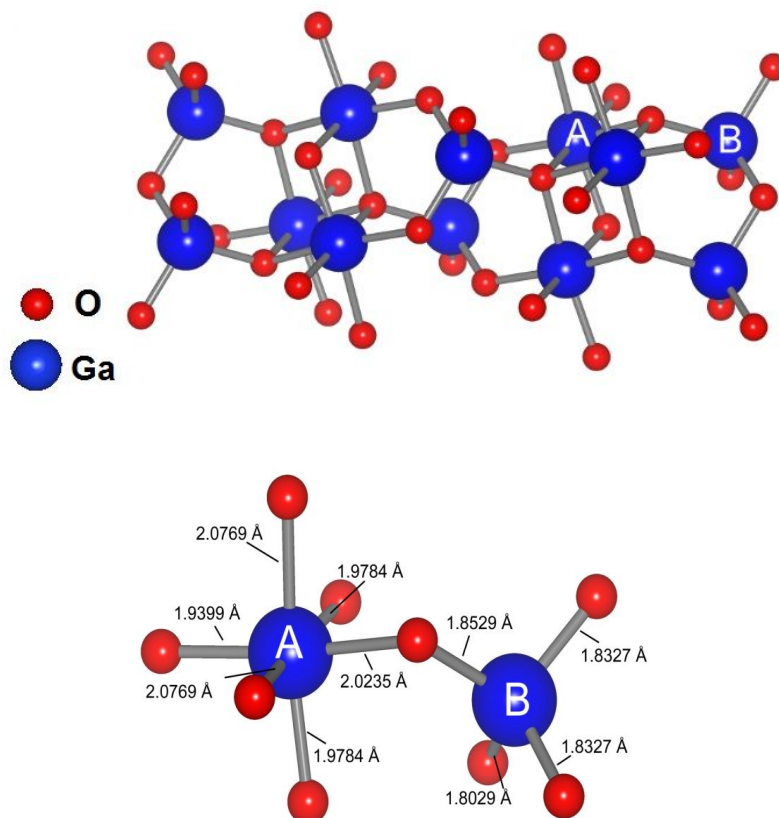


Figure A4 | Crystal structure of β - Ga_2O_3 . (Top) Blue sphere is gallium and red sphere is oxygen. Unit cell structure of β - Ga_2O_3 shows two distinct gallium sites; octahedral sites and tetrahedral sites. (Bottom) Bond lengths of Ga-O in octahedron and tetrahedron. A and B mean the atoms at the top figure.

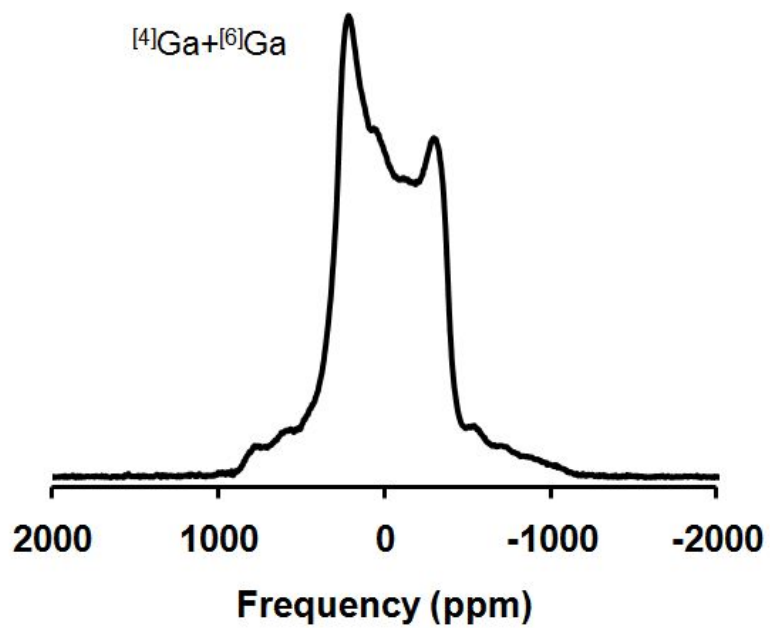


Figure A5 | ^{71}Ga static NMR spectrum of $\beta\text{-Ga}_2\text{O}_3$.

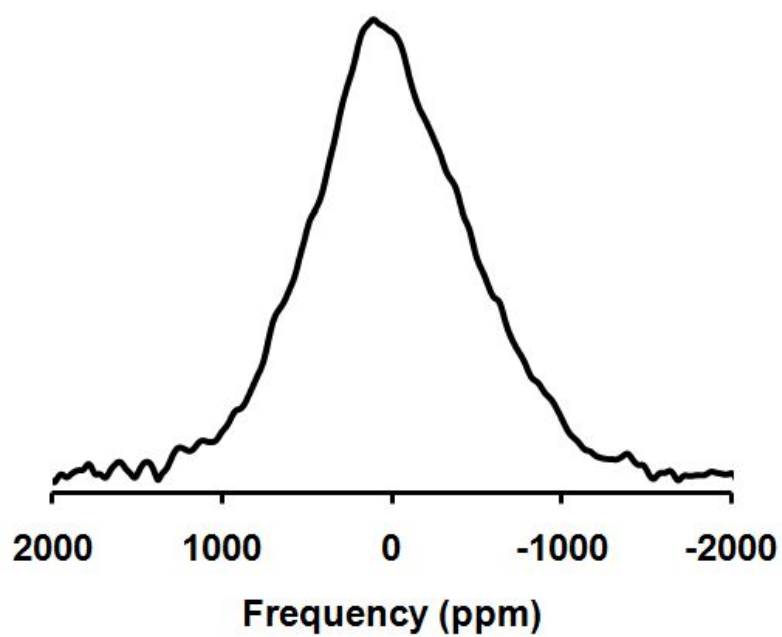


Figure A6 | ^{71}Ga static NMR spectrum of Ga-In-Zn oxide thin film.

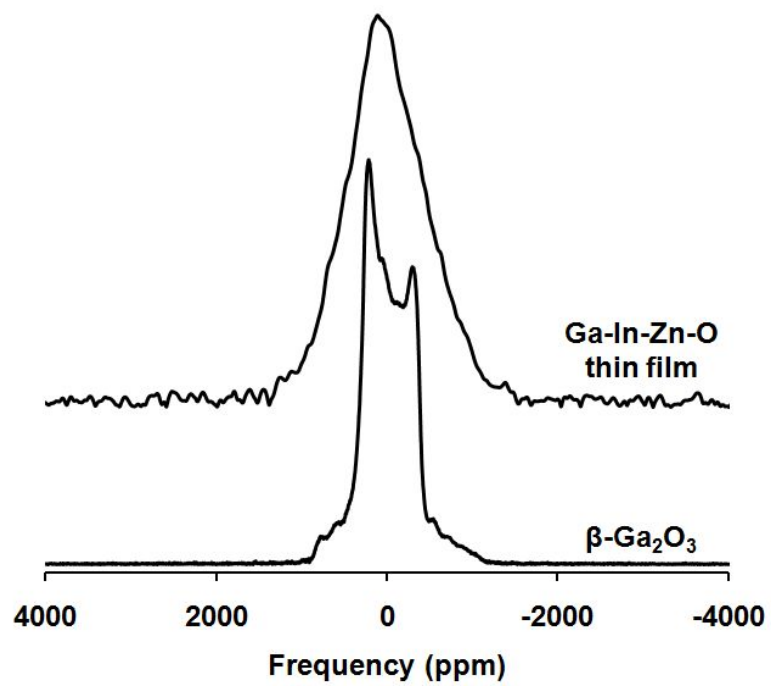


Figure A7 | ^{71}Ga static NMR spectra of $\beta\text{-Ga}_2\text{O}_3$ and Ga-In-Zn oxide thin film.

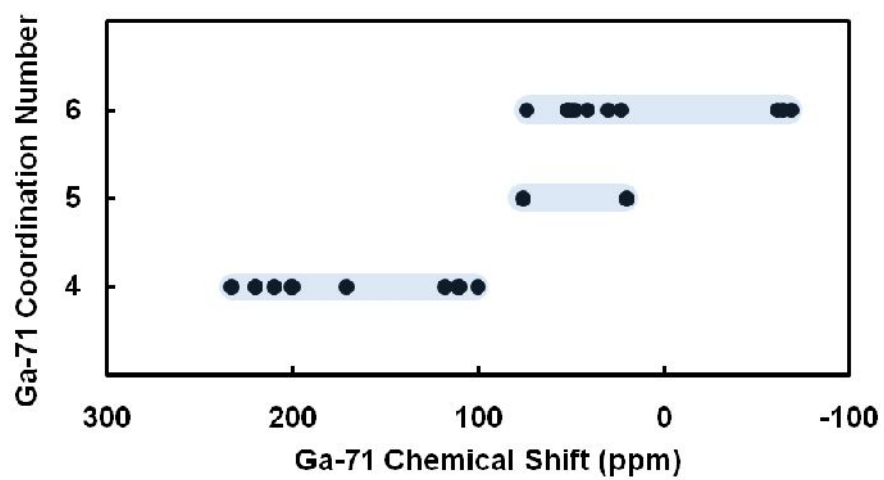


Figure A8 ^{71}Ga NMR chemical shift range of four, five, and six-coordinated Ga in crystalline Ga compounds.

Appendix section

Appendix I. T_1 relaxation time measurement

Determining T_1 relaxation time is important for quantitative analysis. T_1 relaxation is the interaction between spin and lattice (longitudinal relaxation). T_1 relaxation time is the time the max intensity spectrum is obtained. In solid-state NMR, recycle time is set about as three times as T_1 relaxation time. If we set the insufficient recycle time, the peak intensity decreases because of dephasing of signal due to the insufficient recycle time. Each species of nuclide can have different T_1 relaxation time. If the recycle time is not enough for some species, the peak of specific species decreases as the signal is collected and it is hard to get quantitative information from the spectrum.

Carbon has two major species in silicate melts; molecular CO_2 and carbonate ion structure CO_3^{2-} . What I want to know is the exact speciation of carbon in silicates and its quantitative analysis. The absolute amount of carbon in silicate is about tens to hundreds ppm by weight, and it is not a big difference between background signal and carbon in silicate signal. Measuring T_1 relaxation time of this sample is significant to get a high quality and quantitative C-13 NMR spectrum.

Figure A1 shows the C-13 MAS spectra of CaCO₃ and Na₂CO₃. CaCO₃ is a trigonal crystal with $R\bar{3}c$ space group, and Na₂CO₃ is a monoclinic crystal with $C2$ space group. Chemical shift is dependent on the atomic structure of nuclide, so CaCO₃ and Na₂CO₃ show the different chemical shift; 168.7 ppm, and 170.9 ppm, respectively.

Figure A2 shows the T1 relaxation time of CaCO₃ and Na₂CO₃ measured by NMR. Intensity of each spectrum is normalized by its maximum intensity. Experimental condition of each experiment is same except the recycle time condition. Echotime is arrayed from 0.5 s to 28800 s for Na₂CO₃ and 2 s to 57600 s for CaCO₃. Echotime and normalized intensity is plotted by exponential function,

$$M_z = M_0(1 - e^{-\frac{t}{T_1}})$$

M_z is the longitudinal magnetization, M_0 is the equilibrium magnetization, T_1 is T_1 relaxation time, and t is the echotime. Fitted in this equation, relaxation time of CaCO₃ is calculated as 6418 s with the 107 s of error, and 1729 s with 90 s of error for Na₂CO₃.

Appendix II. NMR Imaging.

NMR imaging spectroscopy is non-destructive 2D or 3D imaging technique with the resolution below 10 μm . The resolution is dependent on the contents of fluid, spin-spin relaxation time of fluid, and the connectivity of fluid in pores. A image is obtained by converting the frequency signal to space axes using the inhomogeneous magnetic field in Z-axis. It is called 'magnetic field gradient'. NMR imaging is sensitive to liquid phases, so by this process we can get a NMR image of fluids absorbed in solid, the distribution of fluids in solids, fluid-fluid interaction in pore structure of solids.

Figure A3 shows the NMR imaging of water-absorbed pisolite. This is obtained by 'm_msmevtr' method which can get 2D images of the sample. By varying the parameters, we can find the T_1 and T_2 relaxation time of fluid presented or absorbed in the pore structure of solid. Table A1 shows the T_1 relaxation time of the selected area. The brightness in the picture is how much water is detected by NMR imaging, and that means brighter spots have more water than darker spots. The brightest spots in the figure have water as isolated phases, and grey spots in the figure have water as absorbed phases.

Appendix III. Structure of Ga-In-Zn-O Thin Film: ^{71}Ga

NMR Studies

III-1. Introduction

GIZO thin film is used for thin film transistor. Because of its light-weight and a flexible property, GIZO thin film has received recent attention. It is spotlighted with electric paper, 3D peripheral circuit memory, flat display panel, and building blocks (Park, Lee et al. 2009; Nomura, Kamiya et al. 2010; Yoon, Yang et al. 2010). Ga is involved with site exchange with Al in crystalline phases, and substitution of Ga with Al can control the activity of zeolite used for catalyst. In these reasons, it is important to reveal the atomic structure of Ga in crystal and amorphous materials.

There are difficulties in investigating the structure of amorphous thin film with ordinary spectroscopy and X-ray scattering, but with solid-state nuclear magnetic resonance spectroscopy amorphous oxide researchers in Seoul National University have been discovering the structure of amorphous thin film (Lee, Lee et al. 2009).

There are two isotopes of gallium and the ratio of each are 60.4 % for ^{69}Ga and 39.6 for ^{71}Ga . Both of isotopes can be used for NMR spectroscopy but the relative sensitivity is higher for ^{71}Ga whose value is 0.14 than for ^{69}Ga whose relative sensitivity is 0.069, so ^{71}Ga is used for Ga NMR. ^{71}Ga is

categorized to a quadrupolar nuclide whose nuclear spin is $3/2$. Quadrupolar nuclides show 2nd quadrupolar effect because 2nd order perturbation is not zero in quadrupolar nuclides and quadrupolar effect does not appear from nuclides whose nuclear spin is $1/2$. Quadrupolar nuclides are hard to analyze NMR spectra because of broad peaks due to anisotropy and asymmetric peak shape. However, gallium has relatively high sensitivity and the structure of Ga-included complexes is getting more attention, so many papers have reported the atomic structure of Ga in crystal with ^{71}Ga NMR (Massiot, Farnan et al. 1995; Vosegaard, Massiot et al. 1997; Bureau, Silly et al. 1999; Massiot, Vosegaard et al. 1999; Jung, Park et al. 2003). Compared with the studies of atomic structure of Ga in crystalline phases, atomic structure of Ga in amorphous phases has not been studied due to the disorder of glass itself. There is no NMR study of Ga-bearing thin film until now. In this study, we report the local atomic structures of Ga thin films using ^{71}Ga NMR.

III-2. Experiments

Sample Preparation. $\beta\text{-Ga}_2\text{O}_3$ is used as a reference material to set up the ^{71}Ga NMR condition. $\beta\text{-Ga}_2\text{O}_3$ is purchased from Sigma Aldrich (serial number 215066), and GIZO thin film is taken from Jaejun Yu, the professor of department of physics and astronomy in SNU. Substrate

was removed from the sample until the thickness of the sample reached 20 μm to enhance the signal from the GIZO thin film.

NMR Spectroscopy. The ^{71}Ga NMR spectra were collected with Varian 400 MHz NMR spectroscopy (9.4 T) at a Larmor frequency of 121.989 MHz using a 4 mm Doty double resonance probe. The ^{71}Ga NMR spectra were referenced to Ga-nitrate atomic environments. Because of the high quadrupolar coupling constant, it is difficult to distinguish the signal from the spinning side band when the magic angle spinning (MAS) experiment is processed, so static experiment is performed. The procedure of the ^{71}Ga NMR was followed Hahn echo sequence. The recycle delay is 1 s and the 360° pulse length is 8 μs .

III-3. Results and Discussion

$\beta\text{-Ga}_2\text{O}_3$ is used for the reference to investigate the atomic environment of Ga in GIZO thin film. Figure A4 shows the crystal structure of $\beta\text{-Ga}_2\text{O}_3$. $\beta\text{-Ga}_2\text{O}_3$ is monoclinic system and is categorized in $C_{2/m}^2$ space group. The length of unit cell is $a=12.23 \text{ \AA}$, $b=3.04 \text{ \AA}$, $c=5.80 \text{ \AA}$, and axial angle is 103.7° . $\beta\text{-Ga}_2\text{O}_3$ has two distinguishable crystal sites of Ga as shown in Figure A4. One site is asymmetric tetrahedron and the other is asymmetric octahedron. They are arranged in a different direction. The

bond length of Ga-O of six-coordinated Ga is from 1.9399 Å to 2.0769 Å, and the bond angle of O-Ga-O is 171.934° which represents asymmetry of octahedron site. For four-coordinated Ga, the bond length is from 1.8029 Å to 1.8529 Å, and the bond angle of O-Ga-O of four-coordinated Ga is from 117.908° to 117.908°.

Figure A5 shows the ^{71}Ga static NMR spectrum of $\beta\text{-Ga}_2\text{O}_3$. From figure A4, it is analogized that the ratio of four- and six-coordinated Ga is 1 to 1. Table A1 is the previous NMR studies of ^{71}Ga NMR. According to table A2, chemical shift for four-coordinated Ga ranges between 100 and 200 ppm, and chemical shift for six-coordinated Ga ranges between -69 and 74 ppm.

Figure A6 presents the ^{71}Ga static NMR spectrum of GIZO thin film which shows a broad peak and whose FWHM is about 1000 ppm. ^{71}Ga static NMR spectrum of crystalline $\beta\text{-Ga}_2\text{O}_3$ featured in figure A5 shows 50 ppm of FWHM and tooth-shaped spectrum which can be found in NMR spectrum of general quadrupolar nuclide. In spite of figure A5, figure A6 shows the one broad peak, and spectrum has wider FWHM than in figure A5. Figure A7 shows the stack spectra of GIZO thin film and $\beta\text{-Ga}_2\text{O}_3$ crystal power. The broad peak in GIZO thin film cannot be simulated by one Gaussian or Lorentzian function. If there is one or two atomic environment, we can simulate the adequate atomic environment with Gaussian or Lorentzian function. In other words, this ^{71}Ga NMR spectrum

of GIZO thin film suggests that Ga in GIZO thin film should have structurally and topologically disordered atomic environment. Figure A8 presents the ^{71}Ga chemical shift as a function of atomic structure of Ga. Specific chemical shift data are shown in Table A1. Chemical shift range of four-coordinated Ga is from 100 to 220 ppm; from 20 to 76 ppm for five-coordinated Ga and from 69 to 74 ppm for six-coordinated Ga. There is a linear correlation between the coordination number and chemical shift in ^{71}Ga NMR. As the coordination number increases, chemical shift decreases. It is inferred from ^{71}Ga static NMR spectrum of $\beta\text{Ga}_2\text{O}_3$ and the change of chemical shift of other Ga complexes that Ga has four-, five- and six-coordinate atomic structure in GIZO thin film. However, we cannot clearly separate each atomic environmental peak from the spectrum of GIZO thin film because there is no specific information of peak position or quadrupolar coupling parameter of GIZO thin film. Quadrupolar broadening effect is reduced by NMR experiment with higher magnetic field. To analyze the atomic environment of GIZO thin film, experiments at higher field NMR is needed.

In this study, we report the first ^{71}Ga static NMR spectrum of amorphous GIZO thin film. GIZO thin film consists of quadrupolar nuclide Ga, and paramagnetic element In and Zn. The first ^{71}Ga NMR spectrum of GIZO thin film shows one broad peak and it is inferred that four-, five-, and six-coordinated Ga exists in GIZO thin film compared to the NMR

spectrum of $\beta\text{-Ga}_2\text{O}_3$ which has four- and six-coordinated Ga atomic environment. Because of the low resolution of the spectrum, we cannot analyze the quantitative atomic structure. We can obtain a better resolution spectrum with higher magnetic field NMR.

Eun Jeong Kim

Education

- 2009.8 ~ Candidates of M.S. Seoul National University, Korea. School of
Earth and Environmental Sciences
2009. 8 B. S. Seoul National University, Korea. School of Earth and
Environmental Sciences

Research Experience

- 2010 Teaching assistant, Seoul National University
- 2009 ~ 2011 Research assistant, Seoul National University

Research Interest

Physics and Chemistry of Earth Materials

Honors & Awards

- 2011.2 Scholarship from the Lotte foundation
- 2010.8 Scholarship from the Lotte foundation

Publications

- Lee, S. K., H. N. Kim, et al. (2010). "Nature of Chemical and Topological Disorder in Borogermanate Glasses: Insights from B-11 and O-17 Solid-State NMR and Quantum Chemical Calculations." J. Phys. Chem. B 114(1): 412-420.

Conferencess

2011. 5 1.5 GPa에서 결정질 엔스테타이트의 탄소 용해도에 관한 미시적 기원 연구 (Oral), 2011년 한국광물학회 학술발표회
2010. 10 고압 환경에서 마그네슘 규산염 광물의탄소 용해도에 대한 미시적 기원 연구: 지구 내부에서의 탄소 순환의 고찰 (Oral), 2010년 추계지질과학연합 학술발표회

국문 요약

결정질 규산염 및 맨틀 용융체에 존재하는 기체들은 결정 및 용융체의 성질을 바꾸는 데 중요한 역할을 한다. 결정질 규산염에 존재하는 기체들은 결정질 물질들의 상전이 곡선을 바꾸므로 부분 용융으로 생성되는 마그마의 조성은 기체들의 존재 및 용해도에 따라 크게 바뀐다. 비정질 규산염에 존재하는 이산화탄소는 탄산염 이온(CO_3^{2-})이나 이산화탄소 분자의 형태로 존재할 수 있는데, 이것은 미시적인 관점에서 비정질 규산염의 중합도(polymerization)을 바꾸어 맨틀의 점성도에 영향을 줄 수 있다. 이산화탄소는 마그마에 존재하는 기체들 중 두 번째로 양이 많은 기체로, 압력에 따른 용해도의 차이가 크기 때문에 화산 분출이 일어날 때에는 다량의 이산화탄소가 지권으로부터 대기권으로 방출된다. 대기권으로의 이산화탄소의 유입은 기후 변화에 영향을 줄 수 있으며, 운석 내에 용해되어 있는 탄소의 양으로부터 추정하였을 때 맨틀에 지구상에서 가장 많은 양의 탄소 화학종이 존재할 것으로 생각되지만 이에 대한 실험 데이터들이 부족했기 때문에 1950년대부터 지금까지 여러 다성분계 규산염 물질에서의 이산화탄소의 용해도 및 용해 기작을 설명하기 위한 연구들이 활발히 진행되어 왔다. 하지만 분광 분석기기들의 분석 한계 및 분석 방법서부터 기인한 정량 분석이 어려움, 그리고 이산화탄소의 낮은 용해도로 인해 이산화탄소가

용해되었을 때의 탄소의 화학종 변화에 대한 연구만이 명확히 규명되어 있으며 이산화탄소로 인한 원자 구조의 변화를 명확히 규명한 예는 없다.

본 연구에서는 특정 원소에 대한 원자 구조를 제공함과 동시에 정량적인 분석이 가능한 고분해능 고상 핵자기 공명 분광 분석(NMR, nuclear magnetic resonance)를 이용하여 맨틀의 모델 시스템으로 볼 수 있는 이성분계 결정질 규산염인 $MgSiO_3$ 엔스테타이트(enstatite)와 중앙해령 현무암(MORB, mid ocean ridge basalt)의 모델 시스템으로 볼 수 있는 이원계 비정질 규산염인 $CaO-SiO_2$ 의 공유점 조성과 $CaSiO_3$, 그리고 이원계 비정질 $CaO-B_2O_3$ 에 대해 이들에 용해된 탄소의 원자 구조를 규명하였다.

NMR을 이용하여 분석할 수 있는 탄소 동위원소는 자성 모멘트가 있는 ^{13}C 로, 자연 존재량이 1.1%이기 때문에 분광 분석에 어려움이 있다. 엔스테타이트에 용해된 탄소의 양은 ppm 단위로 자연 존재하는 ^{13}C 를 이용하여 분석하기에는 그 양이 매우 적기 때문에 ^{13}C 를 강화(enrich)하여 분석하였다. 이원계 비정질 산화물들의 경우 C/CO 평형을 맞추었을 때 이원계 비정질 규산염은 400 ppm 정도이고, 이원계 비정질 $CaO-B_2O_3$ 는 1000 ppm 정도의 탄화물($C_{2^{2-}}$, carbide)이 용해된다는 이전 연구 결과에 따라 자연 존재하는 ^{13}C 를 이용하여 분석하였다.

엔스테타이트의 결정 구조에는 Mg^{2+} 가 들어가는 M 구조와 O^{2-} 가 Si^{4+} 와 연결되어 있는 사면체 구조가 존재한다. 합성된 시료가 엔스테타이트의 결정 구조를 유지하고 있는지를 확인하기 위하여 수행한

Raman 분광 분석에서 시료의 진동 모드는 기존에 알려진 엔스테타이트의 진동 모드와 일치함을 확인하였다. 그러나 Raman 분광분석을 통하여 기존에 알려진 기체상의 CO₂의 진동 모드나 CO₃²⁻의 진동모드는 확인할 수 없었다. ¹³C NMR 분석결과에서 126, 161, 171, 173, 그리고 184 ppm에서 피크가 존재함을 보았고, 이전 연구 결과에 따라 용해된 일산화탄소가 184 ppm에서 나타나며 탄산염 이온이 161, 171, 그리고 173 ppm에서 나타남을 확인하였다. 126 ppm에서 나타나는 피크에 대해서는 이산화탄소인 경우와 사베위수 탄소인 경우의 두 가지 원자 환경이 존재할 수 있다. 우선 NMR 분석결과에서 나타나는 126 ppm 피크가 실험적으로 나타나는 노이즈인지 아니면 실제 시료로부터 나오는 피크인지를 확인하기 위해 같은 합성 조건에서 합성한 시료를 통해 ¹³C NMR 분석을 다시 수행하였고, 그 결과 126 ppm 피크는 재현 가능한 실제 피크인 것으로 확인되었다. 이에 따라 126 ppm 피크가 나타내는 탄소의 원자 환경을 정의하고자 탈기체화 반응과 양자 화학 계산을 수행하였다.

탈기체화 반응은 두 번째 합성한 시료를 이용하였으며 750 °C에서 10분간 가열했다. 탈기체화 반응 후 얻어진 시료는 ¹³C NMR 실험에서 이전 실험에서 보이던 126 ppm 피크가 사라진 것을 확인하였다. 그러나 불안정한 사베위수 탄소가 탈기체화 반응 과정에서 화학 결합을 끊고 사라질 수 있으며, 이전 연구들에서 사베위수 탄소에 대한 양자 화학 계산이 존재하지 않았기 때문에 사베위수 탄소에 대한 양자 화학 계산을

수행하였다. 양자 화학 계산은 가우시안 03 프로그램을 이용하였다. 양자 화학 계산의 정확도를 평가하고자 계산된 화학 차폐값을 알고 있는 CO₂ 구조를 이용하여 양자 화학 계산을 실시한 후, 이 중에서 가장 정확도가 높은 계산 방법론을 이용하여 사베위수 탄소에 대한 계산을 수행하였다. B3LYP/6-311+G(2d) 방법을 이용한 계산 결과 사베위수 탄소는 254 ppm에서 화학 차폐값을 나타내는 것으로 확인되었다.

이원계 비정질 규산염 물질인 CaSiO₃와 CaO-SiO₂의 공유점 조성에 대한 시료는 1 기압 하에서 합성되었다. 초기에 합성한 시료는 Ar 분위기에서 ¹³C을 강화한 CaCO₃를 이용하여 합성하였다. 이들 시료에서는 ¹³C NMR 실험을 통해 탄소 원자 환경이 규명되지 않았으며 이것은 CaCO₃에 존재하는 이산화탄소가 가열 과정에서 열분해되어 사라지고 NMR을 통해 분석 가능한 하한선보다 적은 양의 이산화탄소가 용해되어서 나타나는 현상으로 생각된다. CO 분위기에서 C/CO 평형을 이룬 시료들에 대해서 400 ppm의 탄소가 용해될 수 있다는 이전 연구결과로부터 같은 조성의 시료에 대해서 흑연 도가니를 이용하여 CO 분위기에서 합성하였다. 두 번째 합성한 시료의 경우 흑연 도가니에서 함께 나온 흑연 불순물을 제대로 제거하지 못하여 흑연의 ¹³C NMR 스펙트럼만을 얻을 수 있었다. 이것은 시료가 C/CO 평형을 이루어 400 ppm 정도가 용해되어도, ¹³C을 강화하여 합성한 시료가 아니므로 시료에 용해된 탄소 화학종 중 NMR로 분석할 수 있는 것들은 4 ppm 이하로 매우 적은 양이기 때문에 나타나는 현상으로 생각된다. 이로부터 ¹³C

MAS NMR 연구를 통해 현재까지 분석할 수 있는 하한치는 적어도 4 ppm 이상은 되어야 하는 것으로 생각된다.

CaO:B₂O₃의 몰비율이 39.7:60.3 인 이원계 비정질 봉산염 물질은 CO 분위기에서 C/CO 평형을 이루었을 때 1000 ppm 정도의 탄소가 용해될 수 있다고 알려졌다. 1 기압 하에서 흑연 도가니를 이용하여 CO 분위기에서 합성한 탄소를 포함하는 봉산염의 ¹³C MAS NMR 결과에서는 불순물로 포함된 흑연의 피크와 이전 결과들에서는 보이지 않던 270 ppm의 피크가 나타난다. 이것은 양자 화학 계산에서 사베위수 탄소가 나타내는 NMR 화학 차폐의 값과 비슷한 영역이다. 이 피크가 실제 시료에 존재하는 탄소의 원자 환경을 나타내는 피크인지를 확인하기 위해서는 이전과 같이 시료를 재합성 및 재실험 과정을 거쳐야 할 것으로 생각된다. 이 피크가 봉산염에 존재하는 사베위수의 봉산을 치환하여 들어간 탄소가 나타내는 원자 환경이라면, 이것은 실험적으로는 처음으로 산소와 탄소로 이루어진 사면체 구조에 존재하는 사베위수의 탄소의 원자 구조를 밝힌 것이다.

실험을 수행하는 과정에서 초기 물질로 들어간 비정질 탄소와 압축된 비정질 탄소에 대한 ¹³C MAS NMR 실험도 처음으로 수행되었다. NMR 실험 결과에서 비정질 탄소는 138 ppm에서 넓은 반치폭의 피크를 보이며 이것은 비정질 탄소에서 sp² 혼성화된 탄소가 나타내는 피크이다. 압축된 비정질 탄소는 68 ppm에서 넓은 반치폭의 피크를 보이며 이것은 비정질 탄소에서 sp³ 혼성화된 탄소가 나타내는 피크이다. 압축된

비정질 탄소의 피크 위치가 비정질 탄소의 피크와 다른 곳에서 나타나는 것은 피스톤 실린더를 이용한 고압 실험과정에서 비정질 탄소에 압력으로 인한 영구적인 구조 변화가 일어난 것으로 생각된다. Raman 분광 분석을 이용하여 비정질 탄소와 압축된 비정질 탄소에 대한 진동 모드에 대한 연구도 수행되었다. 비정질 탄소의 경우 1200~1600 cm^{-1} 의 영역에서 흑연의 진동 모드가 나타난다. 이 중 1550 cm^{-1} 의 영역에서 G 모드라고 불리는 미세 결정질 흑연의 진동 모드가 나타나며, 1350 cm^{-1} 의 영역에서 D 모드라고 불리는 무질서한 미세 흑연 결정의 진동 모드가 나타난다. 비정질 탄소의 Raman 분광 분석에서는 1200~1600 cm^{-1} 영역에서 넓은 피크가 나타나는 반면에 압축된 비정질 탄소의 경우 G 모드라고 불리는 1550 cm^{-1} 의 영역에서 피크가 나타난다. 이것은 압력에 의해 구조 변화가 생기면서 비정질 탄소의 무질서도가 줄어들고 미세 결정질 흑연이 증가하였음을 알려준다.

위의 실험들은 이제까지는 실험 시간이 오래 걸리고 측정하기 어려워 잘 시도되지 않던 ^{13}C MAS NMR 실험을 이용하여 결정질 규산염 및 비정질 산화물에 용해된 탄소의 화학종을 밝혔으며 NMR을 이용하여 측정할 수 있는 용해도의 한계치가 어디까지인가를 확인했다는 데에 의의가 있다. 또한 비정질 붕산염 물질에서는 B^{4+} 를 치환하여 사면체 구조에 들어가 있는 C^{4+} 가 발견된 것으로 생각되는데, 이것이 실제 원자 환경을 나타내는 피크라면 이제까지 주장만 되어오던 사배위수의 탄소 원자 환경에 대하여 실험적으로 보인 첫 결과이다.

높은 압력 조건에서 실험을 수행한다면 비정질 규산염 물질에서도 규소와 탄소의 치환반응을 통한 사배위수의 탄소의 원자 환경을 발견할 수 있을 것으로 기대된다. 본 연구에서 얻어진 이원계 규산염에서의 이산화탄소의 원자 구조에 대한 정보는 전지구적인 지질현상에서 나타나는 이산화탄소의 용해 및 분출 기작을 설명해주며, 탄소의 원자 구조에 대한 새로운 실험 결과를 제시하고 있다. 이를 통해 지구 내부에서의 탄소 순환을 미시적인 관점에서 설명을 할 수 있다.

주요어: 이산화탄소, 휘발성 유체, 이성분계 비정질 규산염, 엔스테타이트, NMR, 원자 구조



저작자표시-비영리-변경금지 2.0 대한민국

이용자는 아래의 조건을 따르는 경우에 한하여 자유롭게

- 이 저작물을 복제, 배포, 전송, 전시, 공연 및 방송할 수 있습니다.

다음과 같은 조건을 따라야 합니다:



저작자표시. 귀하는 원저작자를 표시하여야 합니다.



비영리. 귀하는 이 저작물을 영리 목적으로 이용할 수 없습니다.



변경금지. 귀하는 이 저작물을 개작, 변형 또는 가공할 수 없습니다.

- 귀하는, 이 저작물의 재이용이나 배포의 경우, 이 저작물에 적용된 이용허락조건을 명확하게 나타내어야 합니다.
- 저작권자로부터 별도의 허가를 받으면 이러한 조건들은 적용되지 않습니다.

저작권법에 따른 이용자의 권리는 위의 내용에 의하여 영향을 받지 않습니다.

이것은 [이용허락규약\(Legal Code\)](#)을 이해하기 쉽게 요약한 것입니다.

[Disclaimer](#)

이학석사 학위논문

**Atomistic Origins of Carbon Solubility into
Amorphous and Crystalline Silicates at Ambient and
High Pressure: Implications for a Deep Carbon Cycle**

이성분계 결정질 규산염 및 비정질 규산염의
탄소 원자 주변 고상 핵자기 공명 분광분석:
지구 내부에서의 탄소 순환에 관한 미시적 기원 고찰

2011 년 8 월

서울대학교 대학원
자연과학대학 지구환경과학부
김 은 정

Abstract

Atomistic origins of carbon solubility into crystalline and non-crystalline silicates are essential to understand the effect of presence of light elements and/or volatiles (e.g. Carbon, CO₂, and etc.) on their diverse macroscopic thermodynamic and kinetic properties and to estimate the amount of carbon in the mantle. The structural information will give better insight into the deep carbon cycle in the earth's interiors and geochemical evolution of earth system through igneous and volcanic (degassing) processes. Because of these pronounced implications and importance, there have been extensive theoretical and experimental efforts to measure the amount of carbon species in silicate melts and to investigate the effect of carbon and volatiles on the melt properties. Despite these efforts, due to difficulties in direct probing of structures of volatile-containing crystals, glasses, and melt at high temperature and pressure conditions, little is known about their structures and carbon speciation in the melts and crystals at high pressure. In this study, we attempt to elucidate the atomic structures around carbon species in silicate crystals and melts at both ambient and high pressure up to 1.5 GPa using solid-state NMR and theoretical quantum chemical calculations.

We first explore the atomic environments around carbon in enstatite (MgSiO₃) synthesized at 1.5 GPa using ¹³C MAS NMR. ¹³C MAS NMR spectra show the multiple peaks at 126, 161, 171, 173, and 184 ppm. The peaks at 161, 171, and 173 ppm correspond to carbonate ion (CO₃²⁻), and the peak at 184 ppm is assigned to dissolved CO. The peak at 126 ppm is extremely sharp (FWHM of ~ 0.6 ppm) and it can either be due to four coordinated carbon (substituting Si in Si-tetrahedron) or due to gas phase

CO₂. In order to check that the sharp peak at 126 ppm is not from an instrumental artifact, we re-synthesized the sample with identical experimental conditions and collected ¹³C NMR spectra, which confirms that the peak at 126 ppm is from carbon species in the crystalline silicates. Then, in order to probe the origin of 126 ppm peak, we heated the sample at 750 °C for 10 minutes (decrepitation experiment). The ¹³C MAS NMR spectrum collected after decrepitation shows that the 126 ppm peak was removed, suggesting the carbon species responsible for the 126 ppm peak is rather unstable at 1 atm.

In order to provide further theoretical constraint on the origin of 126 ppm, we calculate ¹³C NMR chemical shift of carbon-substituted enstatite cluster using quantum chemical calculations based on the density functional theory. The results indicate that ¹³C NMR chemical shifts of four coordinated carbon in enstatite cluster can be ~ 254 ppm, suggesting that the 126 ppm peak is likely to be due to CO₂ rather than four coordinated carbon in the enstatite whereas further thorough theoretical calculations are certainly necessary to confirm the nature of the 126 ppm peak.

We also investigate the atomic environments around carbon in binary calcium oxide glasses synthesized at 1 atm under CO atmosphere using ¹³C MAS NMR. The NMR spectra for the glasses do not show any clear evidence for the carbon species (either molecular CO₂ or other species) in the silicate glasses at 1 atm. The spectrum for carbon-bearing calcium borate glasses synthesized under CO atmosphere, however, show a non-negligible carbon signal at ~270 ppm, implying that the observed peak may be due to the presence of four coordinated carbon in tetrahedral site (substituting boron in the BO₄ unit in the glass).

We finally report the ¹³C NMR spectrum for amorphous carbon

where the broad peak at 138 ppm corresponds to sp^2 hybridized structure of amorphous carbon. The first ^{13}C NMR spectrum for the compressed amorphous carbon at 1.5 GPa shows a new peak at 68 ppm due to carbon in a sp^3 hybridized bonding. This result indicates that there is a permanent pressure-induced densification in amorphous carbon characterized with a bond transition from sp^2 to sp^3 hybridization. The current results and methods show that natural abundance ^{13}C MAS NMR can be a quantitative probe of carbon species in both crystalline and non-crystalline silicates. The detailed structures around light elements and/or volatiles (e.g. Carbon, CO_2 , and etc.) in silicates revealed through ^{13}C NMR give insight into the atomistic mechanisms for deep carbon cycle in the earth's interior.

Keywords: volatiles, CO_2 , binary-component silicate glasses, enstatite, NMR, atomic structure

Tables of contents

ABSTRACT	1
TABLES OF CONTENTS	4
LIST OF FIGURES.....	6
LIST OF TABLES.....	11
1. INTRODUCTION	12
1.1. INTRODUCTION	12
1.2. PREVIOUS WORK	13
1.3. OBJECTIVES.....	19
2. NMR TECHNIQUES	21
3. THE EFFECT OF CARBON ON STRUCTURAL CHANGES IN SILICATE CRYSTALS.....	25
3.1. INTRODUCTION	25
3.2. EXPERIMENTS	26
3.3. RESULTS AND DISCUSSION.....	29
4. THE EFFECT OF CO ₂ IN STRUCTURAL CHANGES OF SILICATE GLASSES	37
4.1. INTRODUCTION	37
4.2. EXPERIMENTS	38
4.3. RESULTS AND DISCUSSION.....	42
5. FUTURE STUDIES.....	46
6. REMAINING QUESTIONS.....	47
7. CONCLUSION	47
REFERENCE.....	49
TABLES	55
FIGURES	60
APPENDIX SECTION.....	86

ABSTRACT IN KOREAN97

ACKNOWLEDGEMENT..... 오류! 책갈피가 정의되어 있지 않습니다.

LIST OF FIGURES

Figure 1 | Carbon solubility in silicate melts as a function of SiO₂ wt%. (A) Carbon solubility for the whole reference system. (B) Carbon solubility for the Na₂O-SiO₂ binary system. (C) Carbon solubility for the Na₂O-Al₂O₃-SiO₂ ternary system. (D) Carbon solubility for the multicomponent system.

Figure 2 | Carbon solubility in silicate melts as a function of mole fraction of non-bridging oxygen (NBO). (A) Carbon solubility for the whole reference system. (B) Carbon solubility for the Na₂O-SiO₂ binary system. (C) Carbon solubility for the multi-component system.

Figure 3 | Carbon solubility in silicate melts as a function of mole fraction of cations. (A) Carbon solubility as a function of mole fraction of Na₂O. (B) Carbon solubility as a function of mole fraction of CaO. (C) Carbon solubility as a function of mole fraction of MgO.

Figure 4 | Carbon solubility in silicate melts as a function of pressure. The upper limit of carbon solubility increases as increasing the pressure.

Figure 5 | Pictures of MgSiO₃ with 2.4 wt% amorphous carbon synthesized at 1.5 GPa in 1400°C for 48 hours. Figure 4A shows a first synthesized sample which has more impurities as-received and figure 4B shows a second synthesized sample which has relatively less impurities as-received. White grains in the picture are MgSiO₃ enstatite crystal, and black grains are compressed amorphous carbon.

Figure 6 | A picture of an MgSiO₃ grain with 2.4 wt% amorphous carbon synthesized at 1.5 GPa in 1400°C for 48 hours.

Figure 7 | Raman spectrum for crystalline MgSiO₃ with 2.4 wt% amorphous carbon at 1.5 GPa. The green, blue, and pink lines refer to the vibrational modes for crystalline MgSiO₃, gas phase CO₂, and CO₃²⁻ ion, respectively.

Figure 8 | One-dimensional ¹³C MAS NMR spectrum of MgSiO₃ with 2.4 wt% amorphous carbon. The bottom line refers to spectral features for rotor backgrounds, the middle line refers to spectral features for rotor and carbon-bearing MgSiO₃, and the top line refers to spectra features for carbon-bearing MgSiO₃, background-subtracted. The number in the bracket means the number of spacers used to collect the NMR signal from the sample.

Figure 9 | One-dimensional ¹³C MAS NMR spectrum of compressed amorphous carbon. The bottom line refers to spectral features for rotor backgrounds, the middle line refers to spectral features for rotor and compressed amorphous carbon, and the top line refers to spectra features for compressed amorphous carbon, background-subtracted. The number in the bracket means the number of spacers used to collect the NMR signal from the sample.
* refers to spinning sidebands.

Figure 10 | One-dimensional ¹³C MAS NMR spectrum of amorphous carbon. The bottom line refers to spectral features for rotor backgrounds, the middle line to spectral features for rotor and amorphous carbon, and the top line to spectra features for background-

subtracted amorphous carbon. The number in the bracket means the number of spacers used to collect the NMR signal from the sample. An asterisk refers to spinning sidebands.

Figure 11 | One-dimensional ^{13}C MAS NMR spectra of MgSiO_3 with 2.4% amorphous carbon, compressed amorphous carbon, and amorphous carbon. The rotor backgrounds were subtracted from the spectra. An asterisk refers to spinning sidebands.

Figure 12 | One-dimensional ^{13}C MAS NMR spectra of firstly and secondly synthesized MgSiO_3 with 2.4 wt% amorphous carbon. (top) Background-included spectra. (bottom) Background-subtracted and weight-normalized spectra.

Figure 13 | One-dimensional ^{13}C MAS NMR spectra of MgSiO_3 with 2.4 wt% amorphous carbon and MgSiO_3 heated at 750 °C for 10 minutes. The rotor backgrounds were subtracted from the original spectra and the spectra were weight-normalized.

Figure 14 | Atomic structure of MgSiO_3 , ortho-enstatite.

Figure 15 | A model cluster for simulating carbon-substituted MgSiO_3 .

Figure 16 | One-dimensional ^{13}C MAS NMR spectra of carbon-bearing CaSiO_3 and carbon-bearing CaO-SiO_2 eutectic composition synthesized in CO gas flow at 1 atm. (top) Background-included spectra. (bottom) Background-subtracted spectra. An asterisk refers to spinning sidebands.

Figure 17 | One-dimensional ^{13}C MAS NMR spectra of carbon-bearing

CaSiO₃ synthesized in CO gas flow at 1 atm. An asterisk refers to spinning sidebands.

Figure 18 | One-dimensional ¹³C MAS NMR spectra of carbon-bearing CaO-B₂O₃ synthesized in CO gas flow at 1 atm. An asterisk refers to spinning sidebands.

Figure A1 | ¹³C MAS NMR spectra of CaCO₃ and Na₂CO₃. The spectra are obtained from T₁ relaxation time measurements and the intensity is normalized to its maximum.

Figure A2 | Normalized maximum intensity of ¹³C NMR spectra for CaCO₃ and Na₂CO₃ as a function of delay time (s). Na₂CO₃ shows shorter T₁ relaxation time than CaCO₃.

Figure A3 | Micro-NMR Imaging of pisolite. The selected areas are where we measure the T₁ relaxation time of water absorbed into pisolite.

Figure A4 | Crystal structure of β-Ga₂O₃. (Top) Blue sphere is gallium and red sphere is oxygen. Unit cell structure of β-Ga₂O₃ shows two distinct gallium sites; octahedral sites and tetrahedral sites. (Bottom) Bond lengths of Ga-O in octahedron and tetrahedron. A and B mean the atoms at the top figure.

Figure A5 | ⁷¹Ga static NMR spectrum of β-Ga₂O₃.

Figure A6 | ⁷¹Ga static NMR spectrum of Ga-In-Zn oxide thin film.

Figure A7 | ⁷¹Ga static NMR spectra of β-Ga₂O₃ and Ga-In-Zn oxide thin film.

Figure A8 | ^{71}Ga NMR chemical shift range of four, five, and six-coordinated Ga in crystalline Ga compounds.

LIST OF TABLES

Table 1 | Functional property of analytical facilities

Table 2 | Calculated isotropic chemical shift of CO₂

Table A1 | T₁ relaxation measurement from micro-imaging NMR

Table A2 | NMR chemical shift, quadrupolar coupling, and asymmetric parameter η of Ga species, as reported in previous studies of ⁷¹Ga NMR

1. Introduction

1.1. Introduction

Microscopic origins of carbon solubility in silicate melts and crystals are an important process to understand the distribution of carbon, the property changes of silicates with carbon, and the evolution of layered earth and atmosphere (Eggler, Mysen et al. 1979; Richet and Bottinga 1984; Zhang and Zindler 1993; Blank and Brooker 1994; Keppler, Wiedenbeck et al. 2003; Behrens and Gaillard 2006; Shcheka, Wiedenbeck et al. 2006). Carbon dioxide is the second most abundant volatile in the mantle. The solubility of carbon in the silicate materials decreases as decreasing the pressure. Carbonates in the slab does not dissociated into carbon dioxide and oxide mineral in the subduction zone when the water contents of the surrounding area is not enough (Kerrick and Connolly 2001), and carbonate minerals can be transfer to the lower mantle as a magnesite (Biellmann, Gillet et al. 1993). It is believed that still large amount of carbon exists in the deep Earth calculated from the carbon contents in the meteorites (Green, Eggins et al. 1993).

Because of its importance and interests, there were many pioneering and intensive studies to measure the amount of carbon in silicate melts

(Pawley, Holloway et al. 1992; Blank, Stolper et al. 1993; Brooker, Kohn et al. 1999) and to define the property changes by the amount of volatiles (Brearley and Montana 1989; Kohn, Dupree et al. 1989; Brooker, Kohn et al. 2001; Brooker, Kohn et al. 2001). The attempts to measure the carbon solubility in silicates have been trying since 1930s, but direct measurement of the solubility and structure of carbon in silicates are performed since 1970s because of the difficulties of measuring a ppm scale of carbon and prevention of carbon contamination from other carbon sources (Blank and Brooker 1994). However, the exact atomic structure and the structural changes induced by pressure are not clearly demonstrated yet. In the next section, we present the previous works.

1.2. Previous Work

Measurement of the carbon solubility in silicate melts. The first experiment of measuring carbon in natural composition melt was performed by Wyllie and Tuttle (1959) and some early studies are based on the commercial silicates (Pearce 1964; Blank and Brooker 1994). The solubility of carbon dioxide in silicate decreases drastically as pressure decreases and that is too small to measure at 1 atm; therefore high pressure experiments are often performed to measure the solubility of carbon species in the silicates. However, the amount of carbon varies with the

analysis facilities(Blank and Brooker 1994), so one could obtain different solubility data of carbon in silicates with the same experimental condition. Figure 1 present the solubility trend of carbon in silicate melts as a function of weight percent of SiO₂ from the previous studies (Mysen, Arculus et al. 1975; Fine and Stolper 1985; Stolper, Fine et al. 1987; Kohn, Brooker et al. 1991; King and Holloway 2002; Nowak, Schreen et al. 2004; Mysen, Fogel et al. 2009; Morizet, Paris et al. 2010). Colors indicate the pressure in a series of colors; red color is the highest pressure and purple color is the lowest pressure. Figure 1A shows the carbon solubility for the whole composition system, figure 1B does that for the binary sodium-silicate system, figure 1C does that for the ternary sodium-aluminosilicate system, and figure 1D does that for the multi-component system. Although figure 1C suggests a weak relation between carbon solubility and weight percent of SiO₂, each figure in figure 1 shows the inverse relationship between the carbon solubility in various silicate melts and the weight percent of SiO₂. In figure 1B, pressure effect on carbon solubility increases until 20 kb. The solubility at 25 kb is less than that at 20 kb, so it is hard to pin down the pressure effect on the carbon solubility in binary system. It is tough to sentence any general equation of pressure effect on carbon solubility in silicate melts from these data because of many undetermined variables in the collected data; composition, the analytical method to measure the solubility, pressure and temperature condition. With classifying the data in detail

variables we can figure out the composition effects on the carbon solubility in silicate melts without extensive solubility measurement ourselves.

Figure 2 shows the effect of non-bridging oxygen (NBO) on the carbon solubility in silicate melts. Figure 2A presents the data for the overall composition system, figure 2B does for the binary sodium-silicate system, and figure 2C does for the multi component silicate system. The data for the ternary system is absent because only fully polymerized silicate system, which means that no NBO exists in the system, are present in the ternary sodium-aluminosilicate experiments. In many cases the mole fraction of NBO increases as decreasing the weight percent of SiO_2 , so figure 2 shows the opposite trend compared with figure 1. Figure 2 indicates that the carbon solubility in silicate melts tends to increase as the mole fraction of NBO increases.

Figure 3 shows the cation effect on carbon solubility in silicates. Figure 3A is a relationship between the mole fraction of Na_2O and carbon solubility, figure 3B between the mole fraction of CaO and carbon solubility, and figure 3C between the mole fraction of MgO and carbon solubility. Carbon solubility in silicate melts is inverse proportion to the mole fraction of Na_2O , and proportion to the mole fraction of CaO and MgO . These results are identical to the carbon solubility in natural melts which is less than 200 ppm in submarine basalt and less than 30 ppm in rhyolitic glasses(Blank and Brooker 1994). It seems that the effect of CaO is greater

than that of MgO, but we cannot find any reason for cation effect on solubility from previous works.

Figure 4 shows the pressure effect on the carbon solubility in silicates. Data are labeled by the composition of silicate melts. There is a positive correlation between pressure and solubility and if the data are normalized into weight percent of SiO₂ in silicate melts it might be shown a stronger correlation.

Measuring the carbon solubility in the silicate is also important in material sciences because of the slag. The carbon in molten slag control the ductility and weldability of the iron(Jung 2006) so calcium-aluminates and calcium silicates are studied(Berryman and Sommerville 1992; Jung 2006). Carbon in slag can also immobilize the hazard element, Cr, from industrial waste(Macias, Kindness et al. 1997) and some calcium-rich industrial wastes are used as a feedstock of mineral CO₂ sequestration (Huijgen and Comans 2005).

Speciation of carbon in silicates. Spectroscopes like Raman, IR, and NMR have been used to identify the speciation of carbon in silicates. The possible species of carbon in silicates are as followed; carbonate, molecular CO, molecular CO₂, methane, moissanite, and neutral carbon (Blank and Brooker 1994; Holloway and Blank 1994; Luth 2003).

Some suggests that four-coordinated carbon can exists as a substitution of Si in silicates (Freund, Kathrein et al. 1980; Shcheka, Wiedenbeck et al. 2006). They suggest that carbon solubility in silicate crystal shows the possibility of carbon substitution into tetrahedral Si sites. However, the experimental evidence of tetrahedral carbon is not found yet.

With Raman and IR spectroscopy, we can define not only the species of carbon in silicate melts but also the vibrational modes of each species. Blank and Brooker (1994) explained the vibrational mode of CO₂ and CO₃²⁻ which can be detected through Raman and IR. Symmetric stretch of CO₂ can be detected by Raman at 1337 cm⁻¹, and asymmetric stretch of CO₂ can be detected by IR at 2349 cm⁻¹. Each of two different asymmetric bends of CO₂ has 667 cm⁻¹ frequency in IR spectrum. However, two times of asymmetric bend of CO₂ is similar to the symmetric stretch of CO₂ and this makes resonance on the energy level and produce a perturbation on Raman spectrum, so we can get Fermi doublet of CO₂ at 1286 cm⁻¹ and 1388 cm⁻¹ in Raman spectrum. Asymmetric stretching of CO₂ in IR spectrum is detected as a doublet at 2340 and 2360 cm⁻¹ because of rotational effects (Brey 1976; Blank and Brooker 1994). Minor bands are shown in 3711 cm⁻¹ for symmetric and asymmetric stretch combined band, 2287 cm⁻¹ for asymmetric stretch of ¹³CO₂, and 2229 cm⁻¹ for asymmetric stretch of ¹⁴CO₂.

Vibrational modes of carbonate ion are more complex than that of CO₂ because it can have two different symmetry species, D_{3h} and C_{2v}. D_{3h}

symmetry species have equivalent C-O bond length. Active frequency of Raman and IR is changed through the symmetry of the molecule. There are four categories of fundamental vibrational motions of CO_3^{2-} ion; symmetric stretch, out-of-plane bend, asymmetric stretch, and in-plane bend. The frequency of each motion is 1063 cm^{-1} , 879 cm^{-1} , 1415 cm^{-1} , and 680 cm^{-1} , respectively. If carbonate ions has C_{2v} symmetry, then all of vibrational modes are active in Raman and IR. However, if it has D_{3h} symmetry, symmetric stretch is only Raman active and out-of-plane bend is only IR active. Frequency range from 1375 to 1680 cm^{-1} is assigned for asymmetric stretch of distorted carbonate (Mysen and Virgo 1980; Fine and Stolper 1985).

XRD can be used for determining the kinetics of carbon dioxide mechanosorption in Ca-silicates (Kalinkin 2009). However, it does not show the CO_2 peak but it shows that the peak intensity in XRD data of wollastonite increases as mechanosorption time increases. This result indicates that as mechanosorption of CO_2 continued, structure of wollastonite changed from crystal to amorphous.

Diffusion of carbon in silicates. The diffusion of carbon in silicate melts and crystals are also important to understand the degassing processes during the upwelling of magma (Nowak, Schreen et al. 2004). Nowak et al. (2004) studies carbon diffusion from rhyolitic to hawaiitic

melt composition and found that the mobility of CO₂ is constant though the changes of composition.

1.3. Objectives

Most of previous studies are focused on the measuring of carbon solubility in silicate melts and the exact atomic structure of carbon in silicate melts has not revealed based on the experimental data. Kubicki (Kubicki and Stolper 1995) made thermodynamic model of dissolution mechanism of carbon dioxide in silicate glasses, but there is no reliable studies with NMR which can support the previous experimental data with qualitative and quantitative atomic environment analysis.

Table 1 shows the analytical advantages of NMR from other analytical methods. We can obtain the information in short range order of the system so there were attempts to get NMR data of silicate melts; however they were focused on the multi-component system which means that we cannot identify which variables do affect on the structural changes of carbon and silicon in silicates. Using simple binary model system, we can show the effect of pressure on the carbon solubility with carefully defined variables. Fundamental aim of this thesis is to obtain good ¹³C NMR spectra of silicate glasses and crystals from the simple composition systems to reveal the atomic structure of carbon in silicates precisely.

The section 2 presents a brief introduction of NMR technique. In this section, previous experiments for ^{13}C NMR study like T_1 relaxation time measurement and NMR imaging is also presented. The section 3 presents studies of carbon solubility in crystalline MgSiO_3 at 1.5 GPa. It includes not only NMR study but also quantum chemical calculation study. The section 4 presents progress on studies of carbon solubility in CaO-SiO_2 binary system. ^{13}C NMR study of CaO-SiO_2 binary system has had a problem due to the low solubility of carbon and CO_2 in 1 atm study.

Appendix sections present T_1 relaxation experiment of calcium carbonate and sodium carbonate in ^{13}C NMR study, brief introduction of NMR imaging, and ^{71}Ga NMR study of Ga-In-Zn oxide thin film.

2. NMR techniques

Nuclear Magnetic Resonance (NMR) is a nuclide-specific facility which can give us the information of atomic structure of material in the short-range order. NMR is especially useful to analyze the atomic structure than other analysis techniques because it can read only one nuclide in one experiment so we can reduce the multi-component bonds.

Sample is located in the center of the magnetic coil. The nuclear spins of the sample are aligned along the magnetic field. If we give a pulse to the sample, the polarized nuclear spins lose their alignment temporarily and return to their original state. In this process, nuclear spins make signals. However, there are other nuclides in molecules so interactions between the magnetic field and spin interaction of neighbor nuclide make the chemical shift which has information of atomic environments.

^{13}C is the isotope of ^{12}C and ^{14}C . The most abundant isotope of carbon is ^{12}C , but the nuclear spin of ^{12}C is zero because ^{12}C has even numbers of neutron and proton. Some elements which have same number of neutron and proton show no spins in magnetic field, too. This is why we use ^{13}C for NMR study despite of the low natural abundance of ^{13}C (1.1 %). The sensitivity of nuclide in NMR is dependent on the gyromagnetic ratio γ and natural abundance. ^{13}C has 4 times low gyromagnetic ratio than ^1H and its natural abundance is only 1.1 % so it shows 6000 times low

sensitivity the ^1H NMR spectrum. That means we need to focus on collecting the high resolution NMR spectrum to overcome these difficulties. We use ^{13}C enriched sample for ^{13}C NMR study to reduce the collection time and enhance the intensity of signal. Fortunately ^{13}C is 1/2 spin nuclide which means that it is not a quadrupolar interaction nuclide, so we can concentrate only on enriching the sample with ^{13}C .

Static NMR and MAS NMR. Static NMR is a NMR experiment which does not spin the rotor by the air. Liquid has no anisotropic properties, so liquid-state NMR uses static NMR experiment and the spectrum features very sharp peaks. Solid has anisotropic properties, so the static solid-state NMR features broad peaks which have three distinct peaks. Compared to static NMR, magic angle spinning (MAS) NMR is a NMR experiment which spins the rotor in a specific angle (54.7°). The first-order parameter of anisotropic is angle dependent, and it is eliminated when the angle is 54.7° . As the first-order derivation of anisotropic parameter disappears, the spectrum shows sharp peaks and spinning side band. The distance between a peak and a spinning side band is determined by spinning speed, so faster the spinning speed broader the distance between a peak and a spinning side band. Spinning side band appears in the area of static NMR spectrum, so if the anisotropy of the nuclide is big, more than two spinning side band will appear.

Echo NMR. Echo NMR is a NMR experiment which gives two different pulses to the sample. One is 45° pulse and the other is 90° pulse. Signals differ depending on the recycle delay time because each species has different relaxation time, so we cannot use echo NMR as a quantitative analysis. With echo NMR experiment we get a dome-shaped spectrum and it makes us easy to simulate the data, so echo NMR is often used for detecting the number of different atomic environment of the sample.

T_1 relaxation NMR. T_1 relaxation NMR uses two pulses to get a spectrum. One is 90° pulse, and the other is 180° pulse. Originally, T_1 relaxation means the dephasing time of one-direction polarized nuclear spin in molecule. However, we cannot erase the magnetic field of NMR so we use opposite way to determine T_1 relaxation time. The net spin direction of sample in magnetic coil is polarized in one direction. If we give a pulse to nuclear spin then we can depolarize the nuclear spin temporarily. After the pulse, nuclear spins return to their original state and the polarization time is as same as depolarization time.

For further information and experimental exercises, see appendix I.

NMR Imaging. NMR Imaging is non-destructive 2D and 3D imaging technique with the μm resolution. NMR imaging uses magnetic

field gradient to get three dimensional image of sample. Detector obtain the signals from different position with different field gradient, so the signals can be divided to its positions. There are several methods to get a NMR imaging. 'm_msmevtr' method is the protocol to obtain a 2D image of a sample. 'm_ge3d' method is for 3D image of a sample.

For further information and experimental exercises, see appendix II.

3. The effect of carbon on structural changes in silicate crystals

3.1. Introduction

MgSiO₃ is the most abundant mineral composition in the mantle and mantle is thought to be the largest carbon reservoir in the Earth (Jambon 1994; Shcheka, Wiedenbeck et al. 2006). Understanding the atomic structure of carbon in silicates is important to estimate the amount of carbon in the mantle, however, we do not know the atomic structure of amorphous silicate properly now. Crystals have unit cell which means that we know their atomic structure well, so it is necessary to identify the atomic structure of carbon in silicates from the silicate crystals and it will be the first step to figure out the carbon solubility and carbon diffusion in the crystalline phase of silicates. In this section, ¹³C NMR study of carbon-bearing MgSiO₃ is presented. There is an unidentified peak in 126 ppm, so decrepitation experiment and quantum chemical calculation is also performed.

3.2. Experiments

Sample Preparation. MgSiO_3 , powdered crystalline phase, is cooked with 2.4 wt% of ^{13}C enriched amorphous carbon using piston cylinder at 1.5 GPa in 1400 C for 48 hours with H_2O . H_2O was added to activate the reaction. The 1.5 GPa condition is the same pressure as the pressure of 40 km depth in Earth's crust. Sample was synthesized twice at the same condition; the first one displayed in figure 4A has starting material as a impurities and the second one displayed in figure 4B has little impurities so second one shows nearly white crystalline MgSiO_3 phases. Each picture is taken at 3.2x magnification. In figure 4, white material is MgSiO_3 enstatite in which ^{13}C might be diffused and black material is compressed amorphous carbon which in transformed from ^{13}C enriched amorphous carbon when the sample was pressured and heated in piston cylinder.

Microscopic Observations. Microscopic observations were performed using Leica M205 C.

Raman Spectroscopy. Raman spectra for the crystalline MgSiO_3 with 2.4 wt% amorphous carbon, amorphous carbon, and compressed amorphous carbon were obtained by Rambooss LS 200 t Raman spectrometer. For the experiment, 488 nm lasers were used and its beam

diameter was 0.8 mm. Exposure time of the sample was 4 s and the number of accumulation was 100 for every spectrum. The Raman spectrum for the crystalline MgSiO_3 was obtained with 300/500 grating, and the Raman spectra for amorphous carbon and compressed amorphous carbon were obtained with 300/500 and 1800/500 grating.

NMR Spectroscopy. The ^{13}C NMR spectra for the MgSiO_3 enstatite with 2.4 wt% of ^{13}C enriched amorphous carbon were obtained by using a Varian 400 MHz solid-state NMR spectrometer (9.4 T) at a Larmor frequency of 100.582 MHz using a 3.2 mm zirconia rotor in a Varian double-resonance probe. The ^{13}C MAS NMR spectra were referenced to solid-state adamantane (ADM) whose left peak is at 38.56 ppm in reference to tetramethylsilane (TMS). TMS is the NMR chemical shift reference material, but because of J-coupling effect of TMS, ADM is used as a reference in this thesis. One pulse sequence was used for ^{13}C 1D MAS NMR and nearly 86400 scans were averaged to achieve the high resolution 1D MAS NMR spectra. The relaxation delay time was 5 s for ^{13}C MAS NMR and the radio frequency pulse strength was 1.3 μs . Sample spinning speed is 14 kHz. The acquisition time is 30.72 ms which is longer than usual MAS NMR but shorter for gas phase NMR. The carbon-bearing silicate sample was packed in the rotor intentionally put the crystalline MgSiO_3 crystals in

the center of the rotor to get more carbon signals dissolved in the crystalline enstatite.

Quantum Chemical Calculations. Quantum chemical calculations are effective tools for obtaining microscopic properties of the sample which are hard to get from the experimental data. NMR chemical shielding calculations were performed using Gaussian 03. Workstation is installed in the Earth materials science laboratory. Gaussian basis sets are used in quantum chemical calculations and are more adequate for the desired results because they consider the electron interactions during calculations.

A cluster of carbon substituted MgSiO_3 orthoenstatite was not optimized due to the instability of carbon in tetrahedral site. NMR chemical shielding calculations were performed at the Becke, three-parameters, Lee-Yang-Parr (B3LYP) hybrid functional level of theory with the 6-311+G(2d) and 6-311G(2d) basis sets; and at the unrestricted Hartree-Fock (UHF) level of theory with the 6-311+G(2d) and 6-311G(2d). The cluster is modified from the structure of orthoenstatite at 0 GPa (Hugh-Jones and Angel 1994); three tetrahedron were cut from the crystal unit cell and a carbon was substituted into the middle tetrahedron.

Absolute chemical shielding calculations varies with level of theory, so structure of CO_2 is used for a reference of calculations. They were performed at the Hartree-Fock (UH) level of theory with the 6-31G* and 6-

311+G(2d) basis sets; unrestricted Hartree-Fock (UHF) level of theory with the 6-31G* and 6-311+G(2d) basis sets; and at the Becke, three-parameters, Lee-Yang-Parr (B3LYP) hybrid functional level of theory with the 6-311+G(2d) and 6-311G(2d) basis sets.

3.3. Results and Discussion

Microscopic Observation. Figure 5 and 6 show the pictures of MgSiO₃ sample taken with Leica M205 C. The sample shows white color in naked-eye observation. In grain by grain, they show different aspects. About 10% of grains of the samples show white and opaque appearances under the microscope and they seem to be at the interface of the MgSiO₃ and the amorphous carbon. The other 90% of grains of the samples show transparent appearances under the microscope and they seem to be inside of the sample when the pressure was applied. Both of them show the crystalline MgSiO₃ peak with Raman spectroscopy.

Raman Results. Figure 7 shows the Raman spectrum for crystalline MgSiO₃ with 2.4 wt% amorphous carbon (first sample). The green, blue, and pink lines refer to the vibrational modes for crystalline MgSiO₃, gas phase CO₂, and CO₃²⁻ ion, respectively. The multiple peaks in the spectrum are consistent with the vibrational modes for crystalline MgSiO₃; however,

no peaks are consistent with the vibrational modes for gas phase CO₂ or CO₃²⁻ ion. This spectrum indicates that white grains in the first sample are crystalline MgSiO₃, and carbon species in the MgSiO₃ is too small to detect by Raman spectroscopy.

¹³C MAS NMR Results. Figure 8, 9, and 10 shows the one-dimensional ¹³C MAS NMR spectra of MgSiO₃ with 2.4 wt% amorphous carbon, compressed amorphous carbon, and amorphous carbon. The number in the bracket of the background label means the number of spacers to use to collect the NMR spectrum from the sample. The sum of the area of the spectrum represents the amount of elements in the sample and the total area of the background is much larger than that of MgSiO₃ spectrum. This means the amount of carbon impurity is significant compared to the total amount of carbon in the sample. The intensity from the sample is smaller than that from background signal; therefore background subtraction is needed for each spectrum. Background subtracted spectra are presented in the top of each spectrum, and they are gathered in figure 11.

In figure 11, there are peaks at 184 ppm, 171 ppm, 161 ppm, and 126 ppm in ¹³C MAS NMR spectrum of enstatite. One broad peak from 40 ppm to 120 ppm is shown in compressed amorphous carbon spectrum and one broad peak from 90 ppm to 170 ppm is in amorphous carbon spectrum.

According to the previous ^{13}C NMR experiments of silicates (Kohn, Brooker et al. 1991), dissolved CO shows a peak at 184 ppm and carbonate ion (CO_3^{2-}) shows a peak in the range between 160 and 170 ppm which can be shifted up to 3 ppm due to the distortion of carbonate ion in the silicate structure. A peak at 126 ppm is assigned as CO_2 in Kohn et al.(1991). However, the data that Kohn et al. present have central spike at 125 ppm so we cannot see the clear peak at 125 ppm and it might seem that it is some noises in the spectrum. Rockafellow et al.(2009) suggest that sp^3 -hybridized carbon in TiO_2 structure shows a peak at 126 ppm and peak at 126 ppm in figure 11 shows a similar peak width and intensity in Rockafellow et al.(2009).

For amorphous carbon, graphite-like sp^2 structure appears at 138 ppm in ^{13}C MAS NMR spectrum and diamond-like sp^3 structure appears at 68 ppm (Alam, Friedmann et al. 2002; Alam, Friedmann et al. 2003). In figure 11, we can find the structural changes of carbon. As sample got pressured, sp^2 structure carbon in amorphous carbon is transformed into sp^3 structure carbon in compressed amorphous carbon.

Figure 12 shows the ^{13}C MAS NMR spectra of first and second synthesized carbon-bearing MgSiO_3 sample. Second sample was synthesized to find out whether the peak at 126 ppm is a real atomic evidence of carbon species in MgSiO_3 or not. It is abbreviated to first sample and second sample. Top spectra show the background-including

spectra and bottom spectra show background-subtracted and weight-normalized spectra. In the top spectra, second sample shows one peak at 126 ppm and no other peaks presented in first sample are found. Peak intensity at 126 ppm of second sample spectrum also decreases compared with that of first sample spectrum. The weight of the sample in the rotor is slightly different; first sample is 59.8 mg and second sample is 36.5 mg. To eliminate the effect of weight from the intensity differences, bottom spectra are weight-normalized after background subtraction. After the weight normalization, however, two spectra present differences in peak intensity and it is thought to be the differences in total amount of carbon in the sample. Important point of this figure is that a peak at 126 ppm does appear again in second sample and it is not a noise or an experimental error. To identify the atomic structure of carbon which can show a peak at 126 ppm in NMR spectrum, decrepitation experiment and quantum chemical calculation is followed.

Decrepitation experiment is performed on the second sample and figure 13 shows the results. When the sample is heated around 750 °C, fluid inclusions and trapped minerals escape from their original sites. After the 10 minutes of heating at 750 °C, the peak at 126 ppm disappears. FWHM (full width half maximum) of the peak at 126 ppm is about 0.6 ppm and that value is hard to find in solid-state NMR spectra. Usual FWHM of solid state material is more than 2 ppm. In case four coordinated carbon breaks

off its bond due to its unstable state, quantum calculation is followed to confirm the structure.

Figure 14 shows the atomic structure of MgSiO_3 , orthoenstatite. Orthoenstatite is one of polymorphs of MgSiO_3 ; orthoenstatite, clinoenstatite, and protoenstatite. Orthoenstatite is high temperature low pressure phase, clinoenstatite is low temperature low pressure phase, and protoenstatite is high pressure and high temperature phase. The transition between orthoenstatite and clinoenstatite is $600\text{ }^\circ\text{C}$ and the transition between orthoenstatite and protoenstatite is over 8 GPa and $900\text{ }^\circ\text{C}$ (Angel, Chopelas et al. 1992). The atomic position of orthoenstatite is referenced to (Hugh-Jones and Angel 1994).

Enstatite is a single-chain mineral; therefore there are four sites for carbon to be substituted during the synthesis: the bridging oxygen site, the non-bridging oxygen site, tetrahedral site of Si, and the network-modifying cation site of Mg. However, because the number of valence electrons of carbon is different from that of Mg, there is low possibility to substitute carbon with Mg.

Figure 15 shows structure model cluster for simulating carbon-substituted MgSiO_3 . Three tetrahedron and combined eight Mg is selected from the original structure and carbon is substituted into the middle tetrahedron. We cannot get the absolutely correct absolute values from the quantum chemical calculations; therefore we use CO_2 as a reference

material to compare the result from the MgSiO₃ structure. The bond length of C-O single bond is 1.53 Å and that of C=O double bond is 1.16 Å. The bond length of Si-O is 1.64 Å. Differences between C-O bond length and Si-O bond length make the model cluster distorted; therefore we calculated the single point energy to prevent the effect of structure during the optimization. Table 2 shows the results of chemical shift of CO₂ in quantum chemical calculations. These data show that B3LYP/6-311+G(2d) method corresponds well with experimental data. With B3LYP/6-311+G(2d) method, structure in figure 15 shows 254.5637 ppm as a chemical shift. This value is far from the 126 ppm in ¹³C NMR; however, we need to find the calculation trend from other method and to calculate with various C-O bond lengths to confirm the peak assignment. The cation radius of carbon is 0.15 Å and that of silicon is 0.26 Å which means that there have to be a distortion in crystal structure when the carbon substitutes Si in Si-tetrahedral site. It is not clear whether the crystal structure maintains with extended four-coordinated carbon in tetrahedral site or the carbon-substituted tetrahedron shrinks in some ways. To confirm the atomistic environments of carbon in crystalline MgSiO₃, we need to perform quantum chemical calculations with various model clusters which have variety ranges of the C-O bond lengths.

Carbon solubility in silicate crystals may follow this equation.

$$S = k \exp\left(-\frac{\Delta G + P\Delta V}{RT}\right)$$

S is the solubility of carbon, k is constant, ΔG is difference of Gibbs free energy between volatile free mineral and volatile saturated mineral, P is pressure, ΔV is volume of the mineral, R is gas constant, and T is the temperature of the system.

Studies of Ar solubility in silicate melts and CO₂ solubility in silicate crystals suggests that there will be solubility limits depending on the composition of the mineral because of the phase transitions near 440 km (Sarda and Guillot 2005; Shcheka, Wiedenbeck et al. 2006; Bouhifd, Jephcoat et al. 2008) It is expected that pressure-induced experiment with MgSiO₃ shows similar trend because we can find the carbonatite melt in high pressure samples which indicate that carbon and silicate are not mixed well in high pressure environments, and the free volume of the silicate crystal and melts will decrease as the pressure increases and this phenomena will occur the decrease solubility of CO₂ and CO₃²⁻.

Carbon solubility in silicate crystals can give us the evolution of carbon distribution in the earth. Earth originally consisted of crystalline minerals and layered earth was made after the magma ocean. Atomic structure of carbon would be changed with the pressure, temperature, and composition and the partitioning coefficient of the carbon would be the important factor to determine where the carbon would be transferred. Investigating the atomic environment of carbon in silicate crystals at low

pressure would be the first step to reveal the evolution and distribution of carbon in silicates from the fundamental level.

CO₂ capture and storage (CCS) is one of the big issues these days and this study could give information of carbon reactivity and atomistic environment. CO₂ storage process have four steps; first one is physical trapping, second one is residual trapping, third one is solubility trapping, and last one is mineral trapping. In this process CO₂ interacts with silicate minerals around 100 bar pressure. If we carry on the experiments at lower pressure, we can identify the carbon environment during CCS processes and it may give more information of CO₂ storage and modeling.

4. The effect of CO₂ in structural changes of silicate glasses

4.1. Introduction

Carbon solubility in silicate melts is important for understanding the evolution of the magma and volcanic eruption. Solubility of carbon in the silicate can lower the melting point of the minerals which means that composition of the partial melting magma can be changed by the amount of volatiles. Volcanic eruption at mid-ocean ridge is usually quietly erupted; however, when the contents of carbon dioxide is high in the magma, intense eruption can occur at mid-ocean ridge volcanoes (Helo, Longpre et al. 2011).

There are intensive previous studies which show the atomic structure of carbon in silicate melt and thermodynamic modeling of dissolution mechanism of carbon in silicates. However, structural analysis of carbon in silicates has not been studied due to the difficulties in getting high resolution NMR spectra. In this thesis, high resolution NMR studies are performed to reveal the atomic structure of carbon in silicate glasses. The composition of the system is CaO-SiO₂ binary system chosen from the

previous data in the section 1 which shows that solubility of carbon increases in the high Ca^{2+} ratio and low SiO_2 ratio conditions.

4.2. Experiments

Sample Preparation. A sample made by Sun Young Park at 1 atm was used to confirm whether carbon dioxide was dissolved in silicate glasses at 1 atm. The composition of the sample was the join of diopside and Ca-tschermakite as 25:75(abbreviated as CMAS), and 0.2 wt% of Co oxide was added to enlarge the spin-lattice relaxation and cut down the collection time. Sintered MgO was used for synthesizing the sample. One CMAS sample from Sun Young Park and two CMAS sample made by me were used for detection. Every sample was grinded in an agate mortar as a powder. The mixture of CMAS powders in a Pt crucible was heated up to 1600 °C in DelTech furnace with 275 °C/hr of the heating ratio and it was fused for 1 hour at 1600 °C. The heated sample was quenched into glasses by manually lowering the temperature of Pt crucible into distilled water.

CaSiO_3 glass was synthesized from mixtures of CaCO_3 powder and SiO_2 powder. Each powder was dried in a box furnace at 300 °C more than a week. Powders were mixed in an agate mortar and Pt crucible was used to fuse the mixtures. The mixture was heated with DelTech furnace with 275 °C/hr of the heating rate until the mixture was heated up to 1600 °C,

and the mixture was heated up to 1650 °C by manually raising the temperature of the furnace with heating rate about 1 °C/min. The mixtures were fused at 1650 °C in the air for 20 minutes. After then the heated sample was quenched into glasses by manually lowering a Pt crucible into distilled water. This sample was used for ¹³C NMR study for 1 atm sample and sent to Geophysical lab. in Carnegie Institute of Washington for higher pressure sample.

CaSiO₃ glass for 1 atm sample with CO gas was synthesized at Prof. Yoon-Bae Kang's laboratory at Graduate Institute of Ferrous Technology (GIFT), POSTECH. CaCO₃ powder and SiO₂ powder were used for synthesizing the sample. Each powder was dried in a box furnace at 300 °C more than a week and grinded in agate mortar. The mixture of powders were put into a micro vial, vacuum-packed, and sent to GIFT. Graphite crucible was used to fuse the mixtures and heating rate was 180 °C/hr. Deoxygenated argon gas was used until the temperature reached to 1600 °C and the temperature was maintained at 1600 °C for 20 hours with pure CO gas flow to equilibrate the sample. The sample was quenched with He gas after then.

CaO-B₂O₃ glass for 1 atm sample with CO gas was synthesized at Prof. Yoon-Bae Kang's laboratory at Graduate Institute of Ferrous Technology (GIFT), POSTECH. CaCO₃ powder and B₂O₃ glass were used for synthesizing the sample. CaCO₃ powder was dried in a box furnace at

300 °C more than a week and B₂O₃ glass was synthesized by several times of melting and quenching of B(OH)₃ above 470 °C. The ratio of CaO and B₂O₃ was 34.7 to 65.3 in mass percent and 39.7 to 60.3 in mol percent. Pre-materials were grinded in agate mortar. The mixture of powders were put into a micro vial, vacuum-packed, and sent to GIFT. Graphite crucible was used to fuse the mixtures. Deoxygenated argon gas was used until the temperature reached to 1500 °C and the temperature was maintained at 1500 °C for 18 hours with pure CO gas flow at the flow rate of 100 ml/min to equilibrate the sample. The sample was quenched with He gas after then.

CaMgSi₂O₆ glass for high pressure experiment was synthesized from mixtures of CaCO₃ powder, MgO, and SiO₂ powder. MgO used for synthesizing the sample was sintered at 1300 °C for 2 hours. Each pre-material was dried in a box furnace at 300 °C more than a week, and was grinded and mixed in an agate mortar as a powder. The mixture of CaMgSi₂O₆ powder in a Pt crucible was heated up to 1600 °C in DelTech furnace with 275 °C/hr of the heating rate, and were fused at 1600 °C in the air for 1 hour. After then the heated sample was quenched into glasses by manually lowering the temperature of Pt crucible into distilled water.

Analysis of Carbon Solubility. Elemental analyzer was used for quantifying the solubility of carbon in silicate glasses, which can quantify the amount of C, H, N, and S in compounds. Inside of the equipment, the

compounds were heated to produce oxides. The oxides were separated with their molar weight when they came through a column in an oven and TCD detector calculated the amount of each oxide. The lowest detect limit of elemental analyzer was 100 ppm.

MAS NMR spectrum collection. The ^{13}C NMR spectra for the CaO-SiO₂ binary system were obtained by using a Varian 400 MHz solid-state NMR spectrometer (9.4 T) at a Larmor frequency of 100.582 MHz using a 4 mm silicon nitride rotor in a Varian double-resonance probe. The ^{13}C MAS NMR spectra were referenced to solid-state adamantane (ADM) whose left peak is at 38.56 ppm in reference to tetramethylsilane (TMS). MAS spectra were obtained using one pulse sequence and 86400 scans were averaged to achieve the high resolution 1D MAS NMR spectra. The relaxation delay time was 5 s for ^{13}C MAS NMR and the radio frequency pulse strength was 1.0 μs . Sample spinning speed is 14 kHz. The acquisition time is 20.48 ms.

The ^{13}C NMR spectrum for the CaO-B₂O₃ binary system were obtained by using a Varian 400 MHz solid-state NMR spectrometer (9.4 T) at a Larmor frequency of 100.582 MHz using a 3.2 mm zirconia rotor in a Varian double-resonance probe. The ^{13}C MAS NMR spectra were referenced to solid-state adamantane (ADM). MAS spectrum was obtained using one pulse sequence and 86400 scans were averaged to achieve the high resolution 1D MAS NMR spectra. The relaxation delay time was 5 s

for ^{13}C MAS NMR and the radio frequency pulse strength was $1.3 \mu\text{s}$ (30° degree pulse). Sample spinning speed is 14 kHz. The acquisition time is 20.48 ms.

4.3. Results and Discussion

Analysis of Carbon Solubility in Silicate Glasses. Carbon solubility in silicate glasses is used by elemental analyzer. Before making a 1 atm silicate sample with CO_2 , we first check the carbon solubility in CMAS sample. Carbon solubility in CMAS samples are detected as 409 ppm for CMAS sample from Sun Young Park in first detection, and 84 ppm in second detection. It is 174 ppm and 35 ppm for CMAS synthesized by me in first detection, and 123 ppm and 52 ppm in second detection. There is unstability of carbon in CMAS silicate glasses and analytical method because its error range is much bigger than the total carbon solubility in silicate glasses.

^{13}C MAS NMR Results. Figure 16 and figure 17 show the ^{13}C MAS NMR studies of the CaO-SiO_2 binary system. Figure 16 shows the ^{13}C MAS NMR spectra of CaSiO_3 and CaO-SiO_2 eutectic system which are synthesized in Ar atmosphere. Top spectra in figure 16 shows the background-including spectra and they do not show any differences in

sight. Bottom spectra in figure 16 shows the background-subtracted spectra and they show no peaks around -50 to 300 ppm. When we check the carbon solubility in silicates with CMAS silicate glasses, the analysis data show that around 100 ppm of carbon dioxide was dissolved in the system. We do not perform the same analysis on the CaO-SiO₂ binary system samples; however it is thought to around 100 ppm of carbon dioxide are presented in this system, too. CaSiO₃ sample with CO gas flow was synthesized to find out the equilibrium effect on the solubility and to aim the high carbon-bearing sample.

Figure 17 shows the ¹³C MAS NMR spectrum of carbon-bearing CaSiO₃ sample. The bottom line shows the rotor background signal, the middle line shows the sample and rotor background signal, and the top line shows the background-subtracted signal. There were impurities in the CaSiO₃ sample which come from the graphite crucible during the sample pickup. Broad peak around 110 ppm is different from sp² or sp³ carbon peak in amorphous carbon ¹³C MAS NMR. Graphite oxides show the peak around 110 ppm in anisotropic chemical shift (Casabianca, Shaibat et al. 2010) and graphite shows the peaks around 100 ppm (Jiang, Solum et al. 2002; Si and Samulski 2008); therefore this peak is assigned to graphite. Further studies are necessary to investigate the atomic environments of carbon in the silicate glasses after picking up the impurities.

Figure 18 shows the ^{13}C MAS NMR spectrum of carbon-bearing CaO-B₂O₃ system. The peak around 110 ppm is assigned to graphite impurities and the peak around 270 ppm is thought to be the four coordinated carbon in calcium borate glasses which have 33 % of four coordinated boron in the whole boron environments. Quantum chemical calculations in section 3 suggest that the four coordinated carbon substituted Si in Si tetrahedron shows the NMR chemical shifts around 254 ppm and NMR chemical shifts are mainly influenced by first nearest neighborhood atoms. This spectrum shows the possibility of presence of the four coordinated carbon in oxides and it would be the first experimental evidence of the sp³ hybridized carbon if the peak around 270 ppm is reproducible and real peak from the carbon species in the calcium borate glasses. Solubility of carbon in CaO:B₂O₃ ratio of 39.7:60.3 in mole percent is approximately 1000 ppm (Park and Min 1999; Jung 2006). Configurational enthalpy of borosilicate is positive which means that mixing of boron and silicon is difficult (Lee, Kim et al. 2010); however in somehow we make the carbon-bearing borosilicate we may see the four coordinated carbon in tetrahedral site in silicate glasses.

Carbonatite is igneous rock which contains more than 50 vol.% of carbonate minerals (Philpotts and Ague 2009). When the rock contains more than 10 vol.% of silicate mineral, the rock is classified as carbonate mineral bearing silicate rock (Philpotts and Ague 2009). Carbonatite have

notably high concentration of Trace element like Nb, Sr, Th and rare earth elements. After 1950s it is known that Nb can exist as many as 0.4 % in carbonatites, so it has been used as a source rock of trace elements and rare earth elements. They are much more dissolved in alkali magma and the partitioning between silicate melts and carbonatite melts make these elements dissolved into carbonatite melts. Pyrochlore is the mineral which contains Nb and is characteristically found in carbonatite(Bell 1989). In some study, Nb is especially low in silicate melts which have high concentration of other rare earth elements (Solovova, Girnits et al. 2008).

The solubility of trace and rare earth elements are dependent on the amount of carbon species in the melts. That means if we can connect those two parameters, the solubility of CO₂ in primordial magma is inferred from the residue of trace and rare earth elements in the erupted magma. Experimental data of CO₂ solubility in the natural sample are always less than that in the primordial magma because of degassing. Trace and rare earth elements have the key to presume the solubility of CO₂ interior of the Earth. This makes it more important to understand the atomistic structure of carbon in the silicates and atomistic sites of carbon species in the silicates.

5. Future studies

To understand the pressure effect on carbon solubility and structure of carbon in silicate crystals, further high-pressure experiment is needed up to at least 24 GPa because phase transition occurs at 24 GPa for MgSiO_3 from spinel to perovskite. Shcheka et al. (2006) expected that the ratio of CO_2 in the whole carbon solubility in depth will increase as the pressure increases until 24 GPa and rapidly decreases above 24 GPa due to the phase transition of minerals. However, this is a speculation from the extrapolation of solubility of carbon in silicate minerals which were synthesized under 15 GPa. The synthesis of high pressure sample will be collaborated with Dr. Fei.

Peak assignment for ^{13}C MAS NMR spectra of CaSiO_3 with CO flow is necessary and after picking up the impurities such as graphite particles from the graphite crucible, high resolution ^{13}C MAS NMR will be performed again. To enhance the amount of carbon species in the silicate glasses, pre-mixed powder samples were sent to Dr. Fei in November 2010 to synthesize the high pressure carbon-bearing silicate glasses.

To identify the peak around 270 ppm in carbon-bearing $\text{CaO-B}_2\text{O}_3$ glasses, ^{13}C MAS NMR study for rotor background and carbon-bearing $\text{CaO-B}_2\text{O}_3$ glasses will be performed again. If the 270 ppm peak still exists,

it would be the first experimental results of four coordinated carbon in oxide glasses.

6. Remaining questions

There is ambiguity whether only fluid inclusions were removed by decrepitation experiment or unstable four coordinated carbon in Si tetrahedron could be removed together if it exists. I still do not understand the key factors of the stability of fluid inclusions and how they control the stability of fluid inclusions. If the pressure is one of the key factors, I wonder if the stability of fluid inclusions decreases when it comes back to 1 atm system after pressuring conditions.

7. Conclusion

Atomistic origins of carbon in binary silicate systems are the major object of this study. Carbon solubility in crystalline silicate and non-crystalline silicate is small in 1 atm system. To find the better experimental conditions to detect the carbon speciation in the silicates with NMR, first the previous studies are summarized. Previous studies show that carbon solubility in silicate melts increases as the pressure increases, temperature

decreases, weight percent of silicate decreases, the fraction of NBO increases, the cations like Ca^{2+} and Mg^{2+} increase. The composition of silicate crystal is decided to MgSiO_3 , which can represent the model mineral of the mantle, and that of silicate glass is decided to the eutectic composition of CaO and SiO_2 .

^{13}C NMR spectra for carbon-bearing MgSiO_3 show that there is dissolved CO, carbonate ion, and gas phase CO_2 or four-coordinated carbon. To confirm the atomic environments of 126 ppm peak deprecation experiment and quantum chemical calculations are performed.

^{13}C NMR spectra for Carbon-bearing CaSiO_3 and CaO-SiO_2 eutectic composition show the no meaningful peaks from carbon. It is thought to be due to low solubility of carbon and ^{13}C isotope in the glasses. ^{13}C NMR spectrum for Carbon-bearing $\text{CaO-B}_2\text{O}_3$ glasses show the peak at 270 ppm which is thought to be the presence of four coordinated carbon substituted boron in BO_4 units.

Reference

- Alam, T. M., T. A. Friedmann, et al. (2002). Solid State ^{13}C MAS NMR Investigations of Amorphous Carbon Thin Films Structural Changes During Annealing. Thin Films: Preparation, Characterization, Applications. J. S. M. P. Soriaga, L. A. Bottomley and Y.-G. Kim. New York, Kluwer: 370.
- Alam, T. M., T. A. Friedmann, et al. (2003). "Low temperature annealing in tetrahedral amorphous carbon thin films observed by C-13 NMR spectroscopy." Phys. Rev. B **67**(24).
- Angel, R. J., A. Chopelas, et al. (1992). "Stability of high-density clinoenstatite at upper-mantle pressures." Nature **358**(6384): 322-324.
- Behrens, H. and F. Gaillard (2006). "Geochemical Aspects of Melts: Volatiles and Redox Behavior." Elements **2**: 275-280.
- Bell, K., Ed. (1989). Carbonatites: genesis and evolution. Carbonatites: Momenclature, Average Chemical Compositions, and Element Distribution. London, Unwin Hyman Ltd.
- Berryman, R. A. and I. D. Sommerville (1992). "Carbon Solubility as Carbide in Calcium Silicate Melts." Metal. Trans. B **23**(2): 223-227.
- Biellmann, C., P. Gillet, et al. (1993). "Experimental evidence for carbonate stability in the Earth's lower mantle." Earth Planet. Sci. Lett. **118**: 31-41.
- Blank, J. G. and R. A. Brooker (1994). Experimental Studies of Carbon Dioxide in Silicate Melts: Solubility, Speciation, and Stable Carbon Isotope Behavior. Volatiles in Magmas. M. R. Carroll and J. R. Holloway. **30**.
- Blank, J. G., E. M. Stolper, et al. (1993). "Solubilities of Carbon-dioxide and Water in Rhyolitic melt at 850-Degrees-C and 750 Bars." Earth Planet. Sci. Lett. **119**(1-2): 27-36.
- Bouhifd, M. A., A. P. Jephcoat, et al. (2008). "Argon solubility drop in silicate melts at high pressures: A review of recent experiments." Chem. Geol. **256**(3-4): 252-258.

- Brearley, M. and A. Montana (1989). "The Effect of CO₂ on the Viscosity of Silicate Liquids at High-Pressure." Geochim. Cosmochim. Acta **53**(10): 2609-2616.
- Brey, G. (1976). "CO₂ Solubility and Solubility Mechanisms in Silicate Melts at High-Pressures." Contrib. Mineral. Petrol. **57**(2): 215-221.
- Brooker, R. A., S. C. Kohn, et al. (2001). "Structural controls on the solubility of CO₂ in silicate melts Part I: bulk solubility data." Chem. Geol. **174**(1-3): 225-239.
- Brooker, R. A., S. C. Kohn, et al. (2001). "Structural controls on the solubility of CO₂ in silicate melts Part II: IR characteristics of carbonate groups in silicate glasses." Chem. Geol. **174**(1-3): 241-254.
- Brooker, R. A., S. C. Kohn, et al. (1999). "Solubility, speciation and dissolution mechanisms for CO₂ in melts on the NaAlO₂-SiO₂ join." Geochim. Cosmochim. Acta **63**(21): 3549-3565.
- Bureau, B., G. Silly, et al. (1999). "From crystalline to glassy gallium fluoride materials: an NMR study of Ga-69 and Ga-71 quadrupolar nuclei." Solid State Nucl. Magn. Reson. **14**(2): 181-190.
- Casabianca, L. B., M. A. Shaibat, et al. (2010). "NMR-Based Structural Modeling of Graphite Oxide Using Multidimensional ¹³C Solid-State NMR and ab Initio Chemical Shift Calculations." Journal of the American Chemical Society **132**(16): 5672-5676.
- Eggler, D. H., B. O. Mysen, et al. (1979). "Solubility of Carbon-monoxide in Silicate Melts at High-pressures and Its Effect on Silicate Phase-relations." Earth Planet. Sci. Lett. **43**(2): 321-330.
- Fine, G. and E. Stolper (1985). "The Speciation of Carbon-dioxide in Sodium Aluminosilicate Glasses." Contrib. Mineral. Petrol. **91**(2): 105-121.
- Freund, F., H. Kathrein, et al. (1980). "Carbon in solid solution in forsterite--a key to the untractable nature of reduced carbon in terrestrial and cosmogenic rocks." Geochimica et Cosmochimica Acta **44**(9): 1319-1321, 1323-1333.
- Green, D. H., S. M. Eggins, et al. (1993). "The other carbon cycle." Nature **365**: 210-211.
- Helo, C., M.-A. Longpre, et al. (2011). "Explosive eruptions at mid-ocean ridges driven by CO₂-rich magmas." Nat. Geosci. **4**: 260-263.

- Holloway, J. R. and J. G. Blank (1994). Application of Experimental Results to C-O-H Species in Natural Melts. Volatiles in Magmas. Washington, Mineralogical Soc America. **30**: 187-230.
- Hugh-Jones, D. A. and R. J. Angel (1994). "A compressional study of MgSiO₃ orthoenstatite up to 8.5 GPa." Am. Mineral. **79**: 405-410.
- Huijgen, W. J. J. and R. N. J. Comans (2005). "Mineral CO₂ Sequestration by Steel Slag Carbonation." Environ. Sci. Technol. **39**(24): 9676-9682.
- Jambon, A. (1994). Earth Degassing and Large-Scale Geochemical Cycling of Volatile Elements. Volatiles in Magmas. Washington, Mineralogical Soc America. **30**: 479-517.
- Jiang, Y. J., M. S. Solum, et al. (2002). "A New Method for Measuring the Graphite Content of Anthracite Coals and Soots." Energy & Fuels **16**(5): 1296-1300.
- Jung, I. H. (2006). "Thermodynamic modeling of gas solubility in molten slags (I) - Carbon and nitrogen." ISIJ Int. **46**(11): 1577-1586.
- Jung, W. S., C. Park, et al. (2003). "Probing the nitrogen deficiency in gallium nitride by Ga-71 magic-angle spinning NMR spectroscopy." Bull. Korean Chem. Soc. **24**(7): 1011-1013.
- Kalinkin, A. (2009). "Kinetics of carbon dioxide chemisorption by Ca-containing silicates." J. Therm. Anal. Calorim. **95**(1): 105-110.
- Keppler, H., M. Wiedenbeck, et al. (2003). "Carbon solubility in olivine and the mode of carbon storage in the Earth's mantle." Nature **424**(6947): 414-416.
- Kerrick, D. M. and J. A. D. Connolly (2001). "Metamorphic devolatilization of subducted oceanic metabasalts: implications for seismicity, arc magmatism and volatile recycling." Earth Planet. Sci. Lett. **189**: 19-29.
- King, P. L. and J. R. Holloway (2002). "CO₂ solubility and speciation in intermediate (andesitic) melts: the role of H₂O and composition." Geochim. Cosmochim. Acta **66**(9): 1627-1640.
- Kohn, S. C., R. A. Brooker, et al. (1991). "C-13 MAS NMR - A Method for Studying CO₂ Speciation in Glasses." Geochim. Cosmochim. Acta **55**(12): 3879-3884.

- Kohn, S. C., R. Dupree, et al. (1989). "A Multinuclear Magnetic-Resonance Study of the Structure of Hydrous Albite Glasses." Geochim. Cosmochim. Acta **53**(11): 2925-2935.
- Kubicki, J. D. and E. M. Stolper (1995). "Structural Roles of CO₂ and CO₃²⁻ in Fully Polymerized Sodium Aluminosilicate Melts and Glasses." Geochim. Cosmochim. Acta **59**(4): 683-698.
- Lee, S. K., H. N. Kim, et al. (2010). "Nature of Chemical and Topological Disorder in Borogermanate Glasses: Insights from B-11 and O-17 Solid-State NMR and Quantum Chemical Calculations." J. Phys. Chem. B **114**(1): 412-420.
- Lee, S. K., S. B. Lee, et al. (2009). "Structure of Amorphous Aluminum Oxide." Phys. Rev. Lett. **103**(9).
- Luth, R. W. (2003). Mantle Volatiles--Distribution and Consequences. Treatise on Geochemistry. D. H. Heinrich and K. T. Karl. Oxford, Pergamon: 319-361.
- Macias, A., A. Kindness, et al. (1997). "Impact of carbon dioxide on the immobilization potential of cemented wastes: Chromium." Cement Concrete Res. **27**(2): 215-225.
- Massiot, D., I. Farnan, et al. (1995). "Ga-71 and Ga-69 nuclear-magnetic-resonance study of beta-Ga₂O₃ - resolution of 4-fold and 6-fold coordinated Ga sites in static conditions." Solid State Nucl. Magn. Reson. **4**(4): 241-248.
- Massiot, D., T. Vosegaard, et al. (1999). "Ga-71 NMR of reference Ga-IV, Ga-V, and Ga-VI compounds by MAS and QPASS, extension of gallium/aluminum NMR parameter correlation." Solid State Nucl. Magn. Reson. **15**(3): 159-169.
- Morizet, Y., M. Paris, et al. (2010). "C-O-H fluid solubility in haplobasalt under reducing conditions: An experimental study." Chem. Geol. **279**: 1-16.
- Mysen, B. O., R. J. Arculus, et al. (1975). "Solubility of Carbon-dioxide in Melts of Andesite, Tholeiite, and Olivine Mephelinite Composition to 30 kbar Pressure." Contrib. Mineral. Petrol. **53**(4): 227-239.
- Mysen, B. O., M. L. Fogel, et al. (2009). "Solution behavior of reduced C-O-H volatiles in silicate melts at high pressure and temperature." Geochim. Cosmochim. Acta **73**(6): 1696-1710.

- Mysen, B. O. and D. Virgo (1980). "The Solubility Behavior of CO₂ in Melts on the Join NaAlSi₃O₈-CaAlSi₃O₈-CO₂ at High-Presssures and Temperatures - A Raman-Spectroscopic Study." Am. Miner. **65**(11-1): 1166-1175.
- Nomura, K., T. Kamiya, et al. (2010). "Comprehensive studies on the stabilities of a-In-Ga-Zn-O based thin film transistor by constant current stress." Thin Solid Films **518**(11): 3012-3016.
- Nowak, M., D. Schreen, et al. (2004). "Argon and CO₂ on the race track in silicate melts: A tool for the development of a CO, speciation and diffusion model." Geochim. Cosmochim. Acta **68**(24): 5127-5138.
- Park, J. H., S. Lee, et al. (2009). "Density of States-Based DC I-V Model of Amorphous Gallium-Indium-Zinc-Oxide Thin-Film Transistors." IEEE Electron Device Letters **30**(10): 1069-1071.
- Park, J. H. and D. J. Min (1999). "Solubility of Carbon in CaO-B₂O₃ and BaO-B₂O₃ Slags." Metall. Mater. Trans. B. **30B**: 1045-.
- Pawley, A. R., J. R. Holloway, et al. (1992). "The Effect of Oxygen Fugacity on the Solubility of Carbon oxygen Fluids in Basaltic Melt." Earth Planet. Sci. Lett. **110**(1-4): 213-225.
- Pearce, M. L. (1964). "Solubility of Carbon Dioxide and Variation of Oxygen Ion Activity in Soda-silicate Melts." J. Am. Ceram. Soc. **47**(7): 342-347.
- Philpotts, A. and J. J. Ague (2009). Principles of Igneous and Metamorphic Petrology, Cambridge University Press.
- Richet, P. and Y. Bottinga (1984). "Anorthite, andesine, wollastonite, diopside, cordierite, and pyrope: thermodynamics of melting, glass transitions, and properties of the amorphous phases." Earth Planet. Sci. Lett. **67**: 415-432.
- Sarda, P. and B. Guillot (2005). "Breaking of Henry's law for noble gas and CO₂ solubility in silicate melt under pressure." Nature **436**(7047): 95-98.
- Shcheka, S. S., M. Wiedenbeck, et al. (2006). "Carbon solubility in mantle minerals." Earth and Planetary Science Letters **245**(3-4): 730-742.
- Shcheka, S. S., M. Wiedenbeck, et al. (2006). "Carbon solubility in mantle minerals." Earth Planet. Sci. Lett. **245**(3-4): 730-742.

- Si, Y. and E. T. Samulski (2008). "Synthesis of Water Soluble Graphene." Nano Letters **8**(6): 1679-1682.
- Solovova, I. P., A. V. Girnis, et al. (2008). "Origin of Carbonatite Magma during the Evolution of Ultrapotassic Basite Magma." Petrology **16**(4): 401-420.
- Stolper, E., G. Fine, et al. (1987). "Solubility of carbon dioxide in albitic melt." Am. Mineral.
- Vosegaard, T., D. Massiot, et al. (1997). "Ga-71 chemical shielding and quadrupole coupling tensors of the garnet $Y_3Ga_5O_{12}$ from single-crystal Ga-71 NMR." Inorg. Chem. **36**(11): 2446-2450.
- Yoon, S. M., S. H. Yang, et al. (2010). "Impact of Interface Controlling Layer of Al_2O_3 for Improving the Retention Behaviors of In-Ga-Zn oxide-based Ferroelectric Memory Transistor." Appl. Phys. Lett. **96**(23).
- Zhang, Y. and A. Zindler (1993). "Distribution and evolution of carbon and nitrogen in Earth." Earth Planet. Sci. Lett. **117**(3-4): 331-345.

Tables

Table 1. Functional property of analytical facilities

Measurements	Raman	IR	NMR	XRD
Source	Monochromic laser	Infrared light	Electromagnetic pulse	X-ray
Method	Inelastic scattering	Absorption	Resonance with external magnetic field and nuclear spin	X-ray diffraction
Detecting Target	Vibrational mode of molecule	Vibrational mode of molecule	Nuclear spin excitation	Crystal structure
Detection Order	Short-range order of atomic structure	Short-range order of atomic structure	Short-range order of atomic structure	Inter-atomic layer distance

Table 2. Calculated isotropic chemical shift of CO₂

Method/ Basis set	Isotropic shielding tensor (σ)	σ_{11}	σ_{22}	σ_{33}	Isotropic chemical shift
HF/6-31G*	74.3815	-29.9204	-29.9204	282.9854	121.9574
HF/ 6-311+G(2d)	52.7114	-62.4767	-62.4767	283.0875	135.7250
UHF/6-31G*	74.3815	-29.9204	-29.9204	282.9854	121.9574
UHF/6- 311+G(2d)	52.7114	-62.4767	-62.4767	283.0875	135.7250
B3LYP/6-31G*	77.0453	-27.0767	-27.0767	285.2894	108.8074
B3LYP/ 6-311+G(2d)	52.3191	-64.4053	-64.4053	285.7680	125.7284

Table A1. T₁ relaxation measurement from micro-imaging NMR

ROI name	ISA_1			ISA_2			ISA_3		
ROI area	0.00598 cm ²			0.00299 cm ²			0.0234 cm ²		
Parameter	value	Std. Dev.	usage	value	Std. Dev.	usage	value	Std. Dev.	usage
Absolute bias	0	0	fixed	0	0	fixed	2676.68	78461.1	varied
Signal intensity	606403	3209.63	varied	-2.09E+06	1.23E+07	varied	109762	77942.2	varied
T ₁ relaxation time (msec)	509.757	4.82943	varied	2.24E+06	1.23E+07	varied	138.2	52.0383	varied
Standard dev. of the fit	2668.9			4185.79			2668.26		
Repetition time (msec)	Mean	Std. Dev.	Func.	Mean	Std. Dev.	Func.	Mean	Std. Dev.	Func.
4000	606123	188388	606166	141390	26847.5	146149	110373	45107.0	112439
3000	610456	185941	604717	153237	25935.7	146149	112772	43142.9	112439
2000	589368	182167	594412	142722	22984.9	146149	116630	45379.8	112439
1000	517101	148075	521133	147453	27004.5	146149	111898	44051.0	112360
600	424552	108059	419514	145007	24907.6	146142	107620	42176.9	111010
400	327396	76093	329724	147970	26628.1	145651	108756	38777.2	106366
300	270036	58795	269758	141580	25054.8	142072	98915	36091.6	99916
250	235253	52070	235064	134529	21832.7	134484	94629	33650.1	94458

Table A2. NMR chemical shift, quadrupolar coupling, and asymmetric parameter η of Ga species, as reported in previous studies of ^{71}Ga NMR

Composition	Sample Type †	Spinning Speed (kHz)	Field Strength (T)	Functional Group	Chemical Shift (ppm)	C_Q (MHz)	η_Q	Ref
$\alpha\text{-Ga}_2\text{O}_3$	p	15	14.1	^{61}Ga	52	8.16	0	[01]
$\beta\text{-Ga}_2\text{O}_3$	p	15	14.1	^{43}Ga	201	11.1	0.85	[01]
$\beta\text{-Ga}_2\text{O}_3$	p	15	14.1	^{61}Ga	41	8.34	0.1	[01]
$\beta\text{-Ga}_2\text{O}_3$	p	12.5	11.7	^{61}Ga	50	-	-	[02]
$\beta\text{-Ga}_2\text{O}_3$	p	static	11.7	^{43}Ga	220	-	-	[02]
$\gamma\text{-Ga}_2\text{O}_3$	p	31	17.6	^{61}Ga	50	-	-	[03]
$\gamma\text{-Ga}_2\text{O}_3$	p	31	17.6	^{53}Ga	20	-	-	[03]
$\gamma\text{-Ga}_2\text{O}_3$	p	31	17.6	^{43}Ga	110	-	-	[03]
$\delta\text{-Ga}_2\text{O}_3$	p	15	14.1	^{61}Ga	52	8.5	0	[01]
$\delta\text{-Ga}_2\text{O}_3$	p	15	14.1	^{43}Ga	210	7	0	[01]
$\text{Y}_3\text{Ga}_5\text{O}_{12}$ Garnet	s	-	9.4	^{43}Ga	220	13.1	0.05	[04]
$\text{Y}_3\text{Ga}_5\text{O}_{12}$ Garnet	s	-	9.4	^{43}Ga	220	4.1	0.03	[04]
MgGa_2O_4 spinel	p	10	9.4	^{43}Ga	171	7.6	0.5*	[05]
MgGa_2O_4 spinel	p	10	9.4	^{61}Ga	74	7.6	0.5*	[05]
$\text{LaGaGe}_2\text{O}_7$	p	static	7.0, 9.4 11.7	^{53}Ga	75.8	15	0.7	[05]
$\text{Ca}_2\text{Ga}_2\text{SiO}_7$ gehlenite	p	10	9.4	^{43}Ga	233	>13.5	0.6 ~ 0.8	[05]

Sn:Ga:Zn:Al:O = 0.5:3.3:1.7:34.7:59.8	P	30	18.8	⁶⁷ Ga	30	12*	-	[06]
		30	18.8	⁶⁹ Ga	200	12*	-	[06]
GaPO ₄ cristoballite	p	static	7.0, 9.4, 11.7	⁶⁷ Ga	118	4.7	0.45	[05]
	p	15	17.6	⁶⁷ Ga (1)	-61.3	6.4		[07]
GaPO ₄ cristobalite	p	15	17.6	⁶⁷ Ga (2)	-68.6	2.8		[07]
	p	15	17.6	⁶⁷ Ga (3)	-64.2	4.5		[07]
GaPO ₄ quartz	p	15	18.8	⁶⁷ Ga	111	8.5	0.45	[07]
GaPO ₄ quartz	p	15	18.8	⁶⁷ Ga	100.3	8.6	0.51	[05]
Ga(OH)(O ₃ PC ₂ H ₄ - CO ₂ H)	p	10	9.4	⁶⁷ Ga	23	9.3	0.1	[05]
	p	10	9.4	⁶⁷ Ga	48	14.3	0.57	[05]

† p: crystalline power, s: single crystal, a: amorphous

* : fixed value

- [01] Bradely et al., 1993, Magn. Reson. Chem.
- [02] Massiot et al., 1995, Solid State Nucl. Magn. Reson.
- [03] Vosegarrd et al., 1997, Inorg. Chem.
- [05] Massiot et al., 1999, Solid State Nucl. Magn. Reson.
- [06] Massiot et al., 2000, Solid State Nucl. Magn. Reson.
- [07] Jung et al., 2003, Bull. Korean Chem. Soc.
- [08] Areal et al., 2005, Anorg. Allg. Chem
- [09] Montouillout et al., 2006, Magn. Reson. Chem.
- [10] O'Dell et al., 2007, Appl. Magn. Reson.

Figures

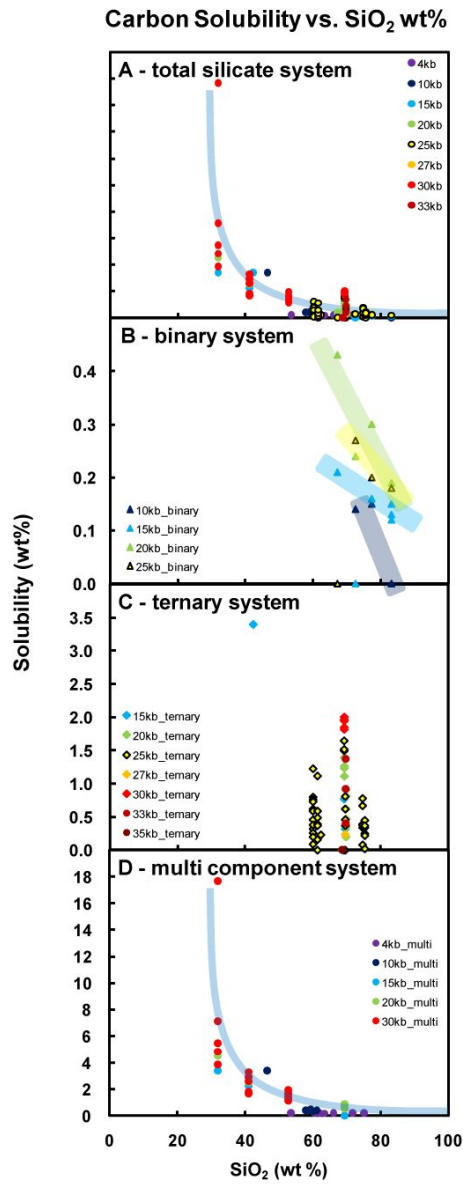


Figure 1 | Carbon solubility in silicate melts as a function of SiO₂ wt%. (A) Carbon solubility for the whole reference system. (B) Carbon solubility for the Na₂O-SiO₂ binary system. (C) Carbon solubility for the Na₂O-Al₂O₃-SiO₂ ternary system. (D) Carbon solubility for the multicomponent system.

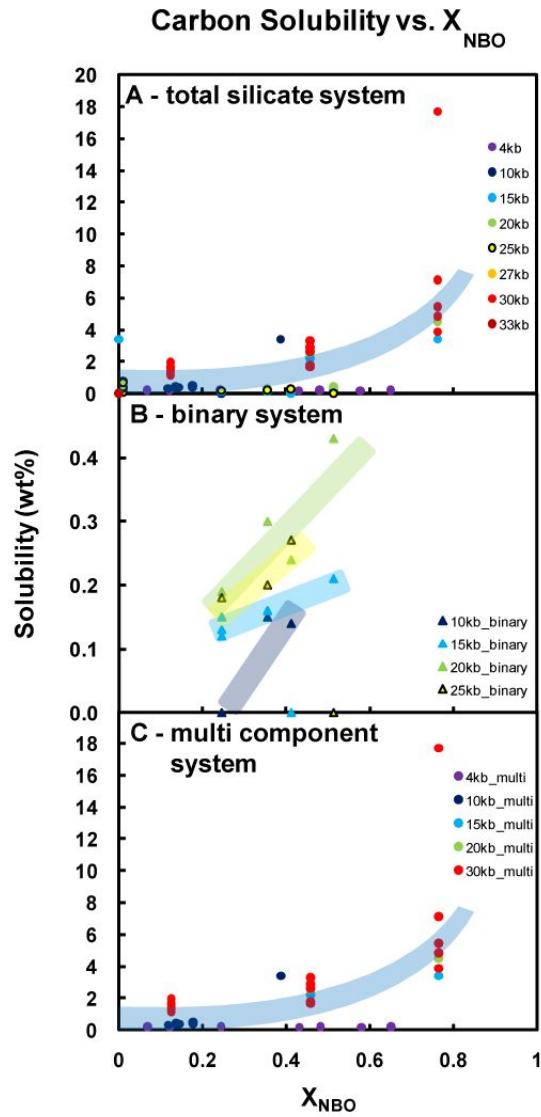


Figure 2 | Carbon solubility in silicate melts as a function of mole fraction of non-bridging oxygen (NBO). (A) Carbon solubility for the whole reference system. (B) Carbon solubility for the $\text{Na}_2\text{O-SiO}_2$ binary system. (C) Carbon solubility for the multi-component system.

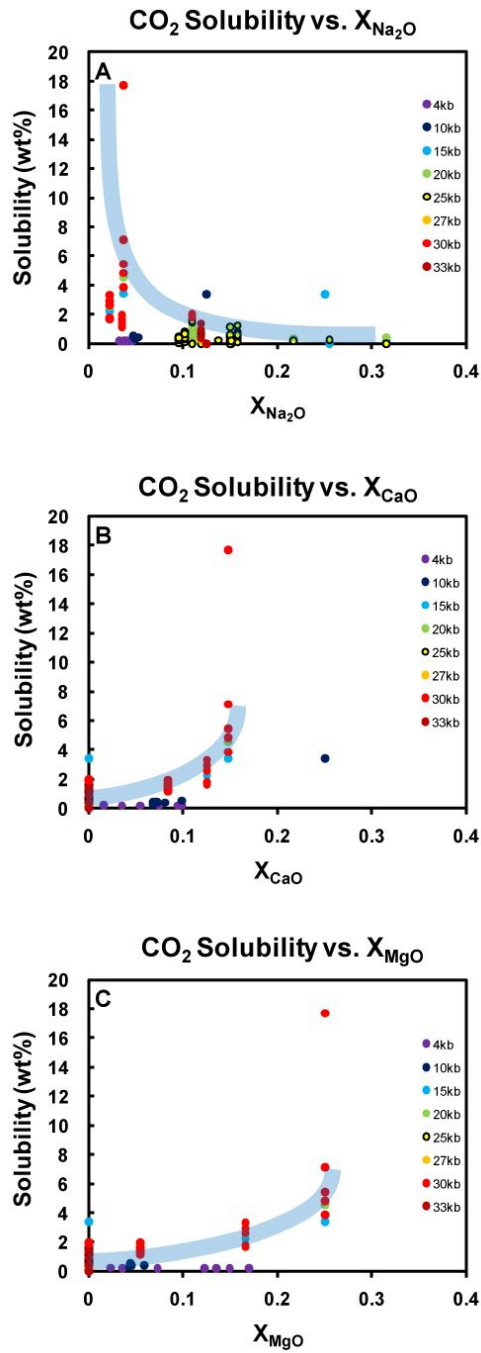


Figure 3 | Carbon solubility in silicate melts as a function of mole fraction of cations. (A) Carbon solubility as a function of mole fraction of Na₂O. (B) Carbon solubility as a function of mole fraction of CaO. (C) Carbon solubility as a function of mole fraction of MgO.

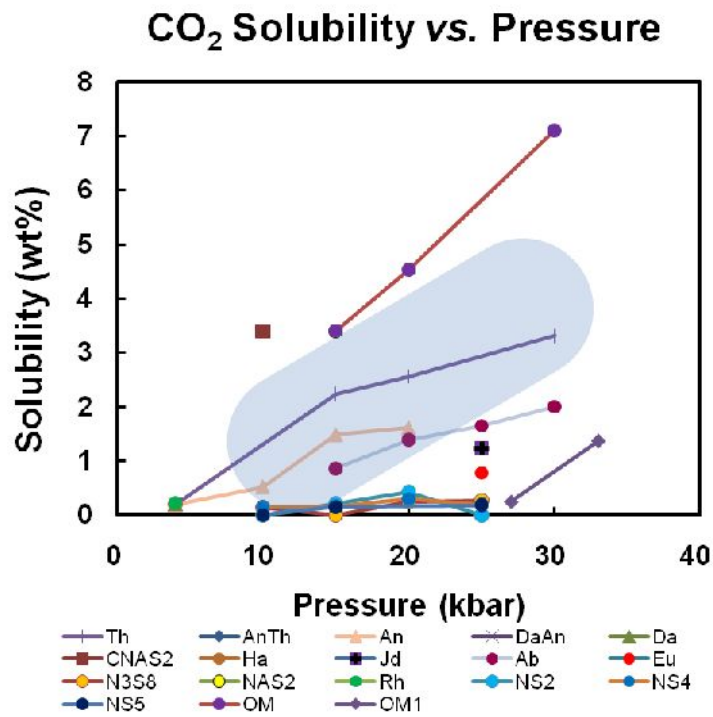


Figure 4 | Carbon solubility in silicate melts as a function of pressure. The upper limit of carbon solubility increases as increasing the pressure.

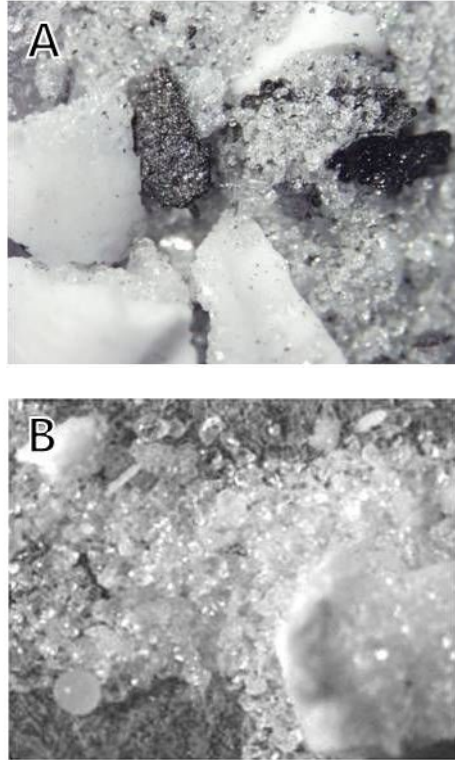


Figure 5 | Pictures of MgSiO_3 with 2.4 wt% amorphous carbon synthesized at 1.5 GPa in 1400°C for 48 hours. Figure 5A shows a first synthesized sample which has more impurities as-received and figure 5B shows a second synthesized sample which has relatively less impurities as-received. White grains in the picture are MgSiO_3 enstatite crystal, and black grains are compressed amorphous carbon.

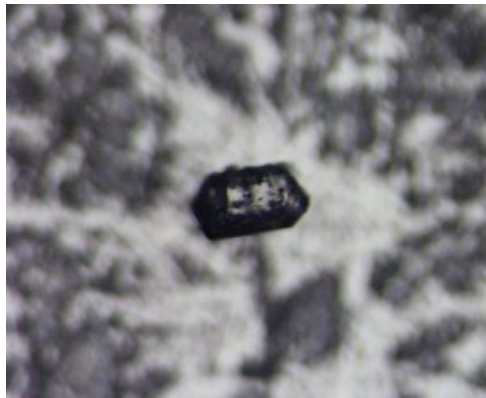


Figure 6 | A picture of an MgSiO₃ grain with 2.4 wt% amorphous carbon synthesized at 1.5 GPa in 1400°C for 48 hours.

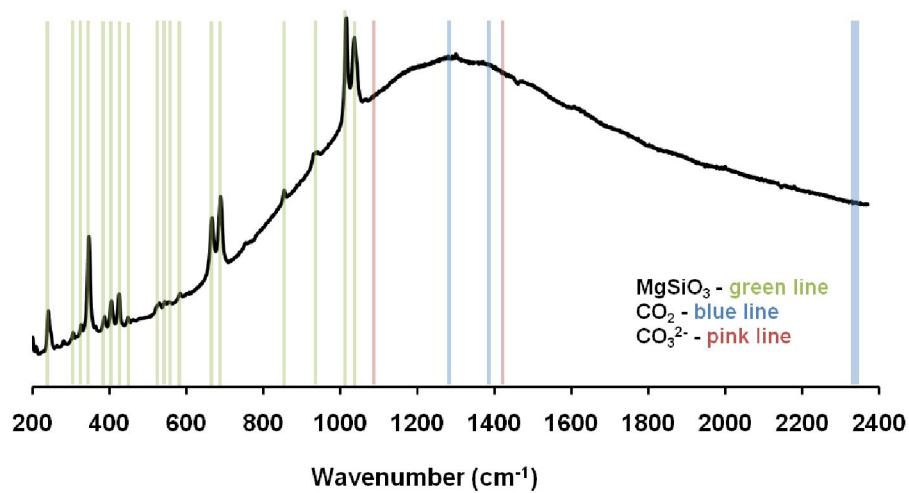


Figure 7 | Raman spectrum for crystalline MgSiO_3 with 2.4 wt% amorphous carbon at 1.5 GPa. The green, blue, and pink lines refer to the vibrational modes for crystalline MgSiO_3 , gas phase CO_2 , and CO_3^{2-} ion, respectively.

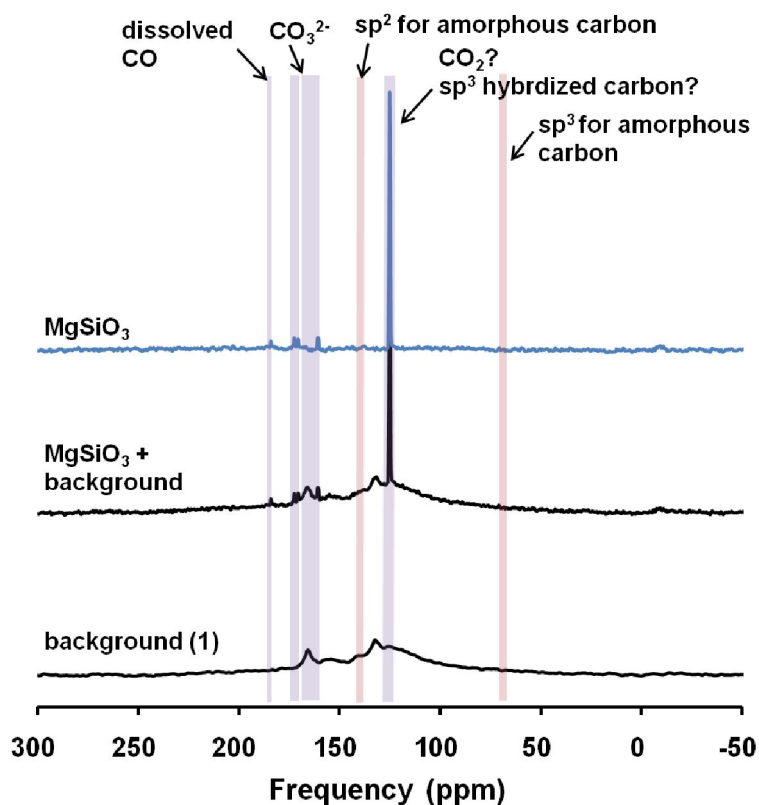


Figure 8 | One-dimensional ^{13}C MAS NMR spectrum of MgSiO_3 with 2.4 wt% amorphous carbon. The bottom line refers to spectral features for rotor backgrounds, the middle line refers to spectral features for rotor and carbon-bearing MgSiO_3 , and the top line refers to spectra features for carbon-bearing MgSiO_3 , background-subtracted. The number in the bracket means the number of spacers used to collect the NMR signal from the sample.

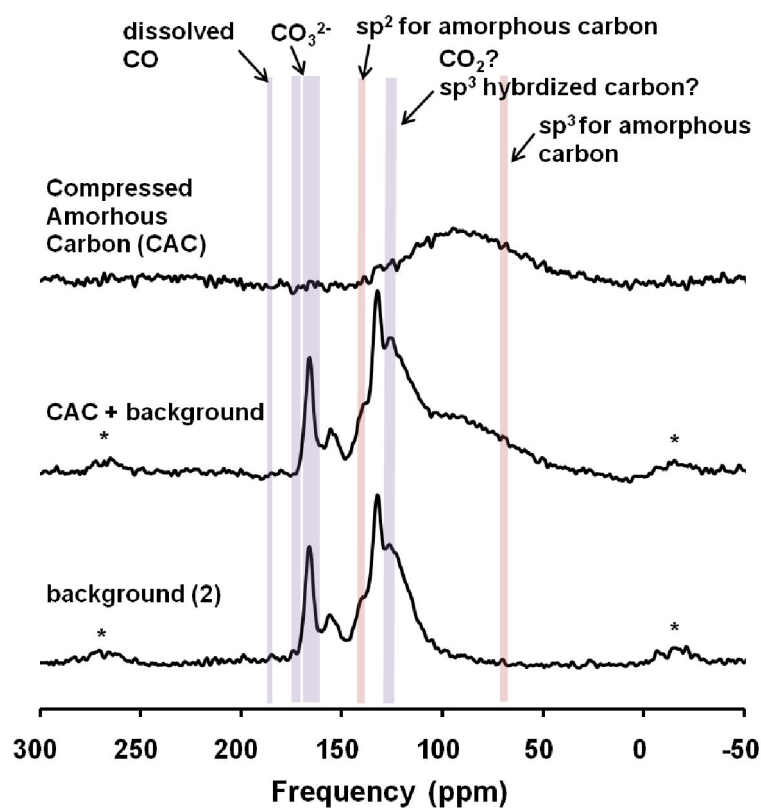


Figure 9 | One-dimensional ^{13}C MAS NMR spectrum of compressed amorphous carbon. The bottom line refers to spectral features for rotor backgrounds, the middle line refers to spectral features for rotor and compressed amorphous carbon, and the top line refers to spectra features for compressed amorphous carbon, background-subtracted. The number in the bracket means the number of spacers used to collect the NMR signal from the sample. An asterisk refers to spinning sidebands.

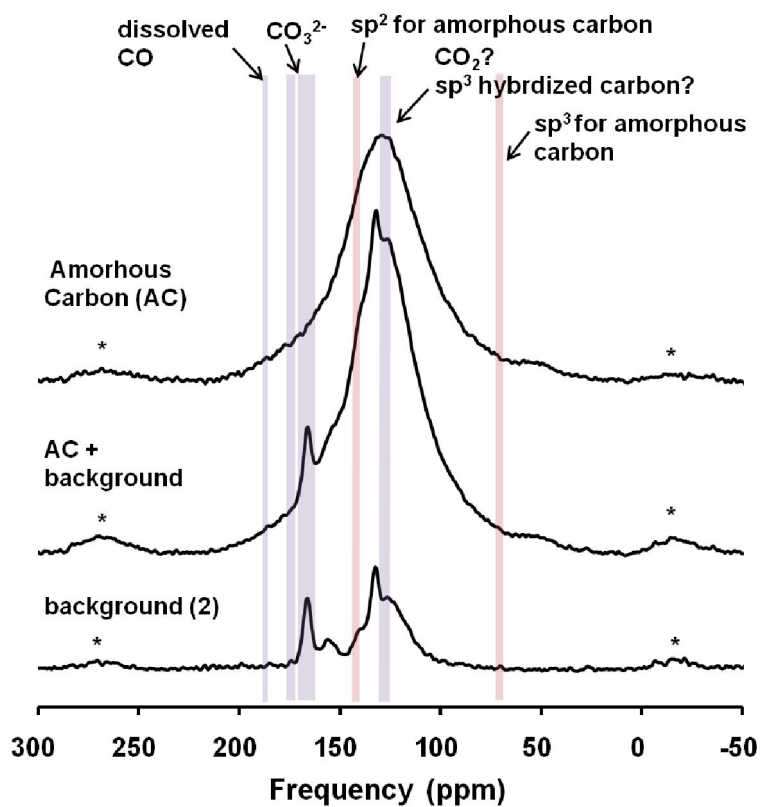


Figure 10 | One-dimensional ^{13}C MAS NMR spectrum of amorphous carbon.

The bottom line refers to spectral features for rotor backgrounds, the middle line to spectral features for rotor and amorphous carbon, and the top line to spectra features for background-subtracted amorphous carbon. The number in the bracket means the number of spacers used to collect the NMR signal from the sample. An asterisk refers to spinning sidebands.

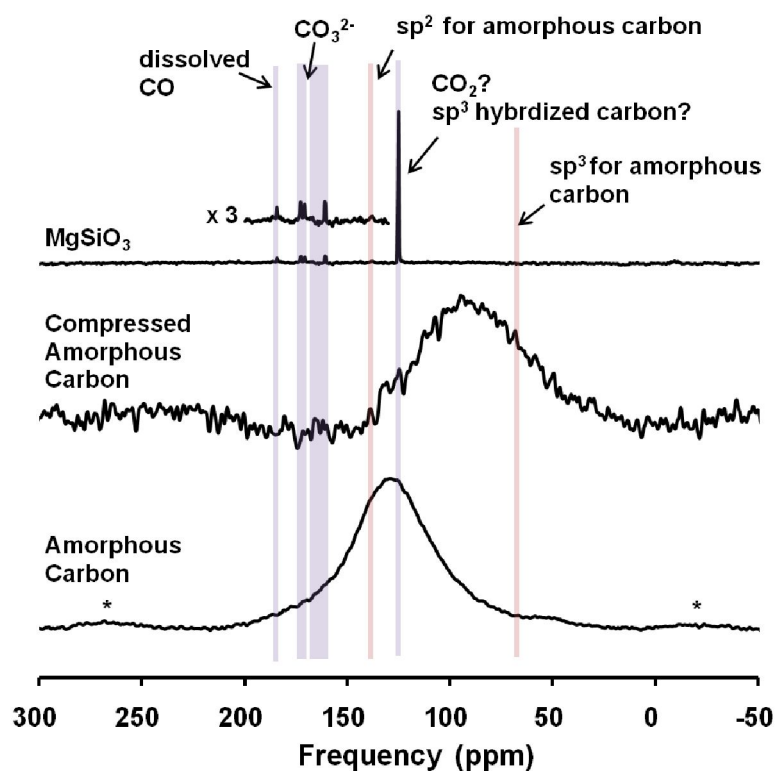


Figure 11 | One-dimensional ^{13}C MAS NMR spectra of MgSiO₃ with 2.4% amorphous carbon, compressed amorphous carbon, and amorphous carbon. The rotor backgrounds were subtracted from the spectra. An asterisk refers to spinning sidebands.

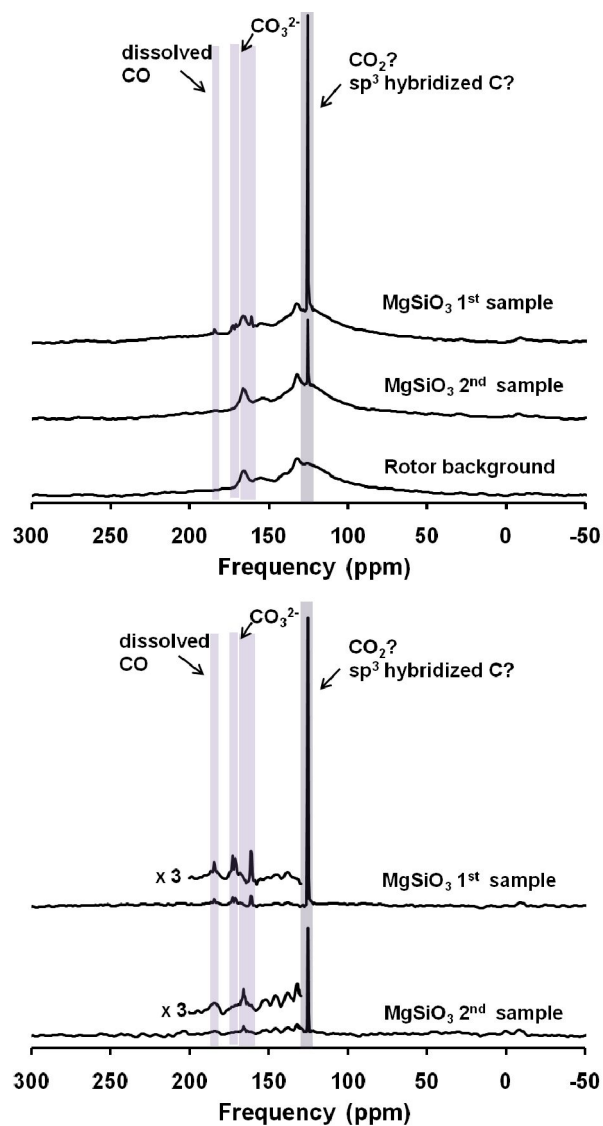


Figure 12 | One-dimensional ^{13}C MAS NMR spectra of firstly and secondly synthesized MgSiO_3 with 2.4 wt% amorphous carbon. (top) Background-included spectra. (bottom) Background-subtracted and weight-normalized spectra.

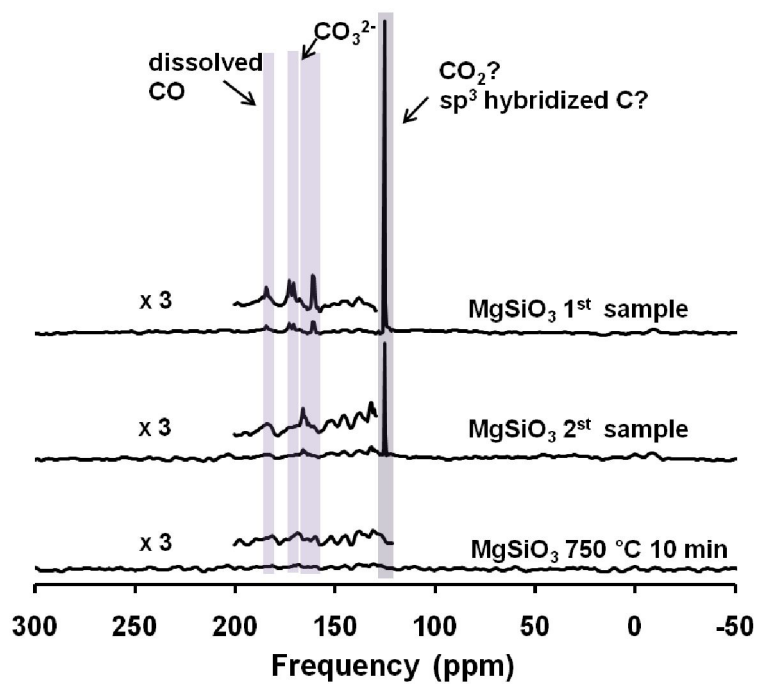


Figure 13 | One-dimensional ^{13}C MAS NMR spectra of MgSiO_3 with 2.4 wt% amorphous carbon and MgSiO_3 heated at 750 °C for 10 minutes. The rotor backgrounds were subtracted from the original spectra and the spectra were weight-normalized.

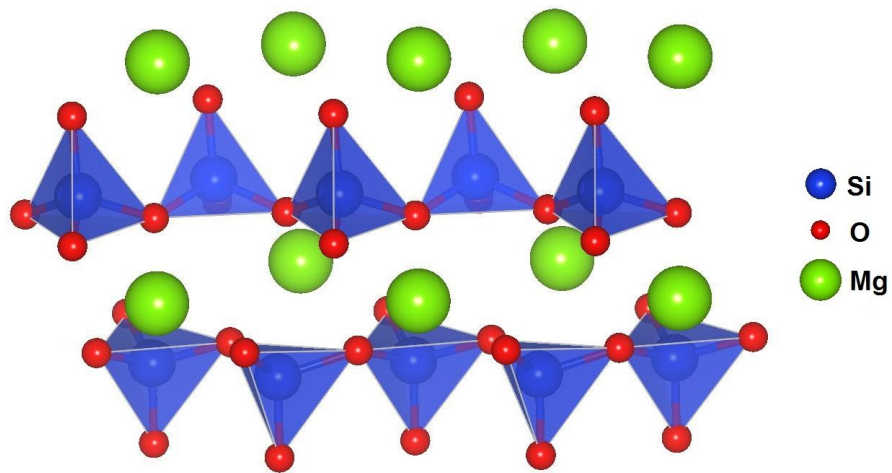


Figure 14 | Atomic structure of MgSiO_3 , ortho-enstatite.

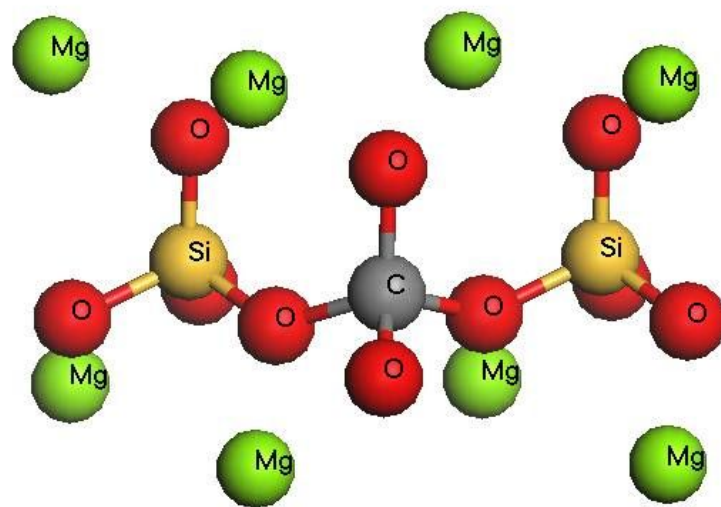


Figure 15 | A model cluster for simulating carbon-substituted MgSiO₃.

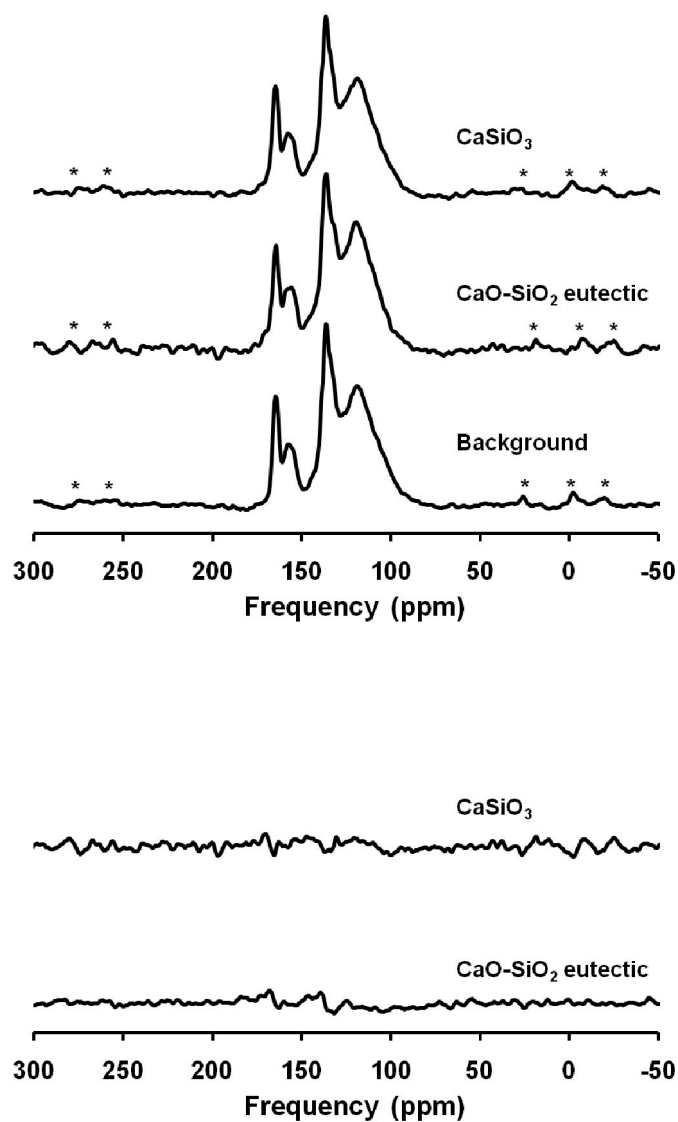


Figure 16 | One-dimensional ^{13}C MAS NMR spectra of carbon-bearing CaSiO_3 and carbon-bearing CaO-SiO_2 eutectic composition synthesized in CO gas flow at 1 atm. (top) Background-included spectra. (bottom) Background-subtracted spectra. An asterisk refers to spinning sidebands.

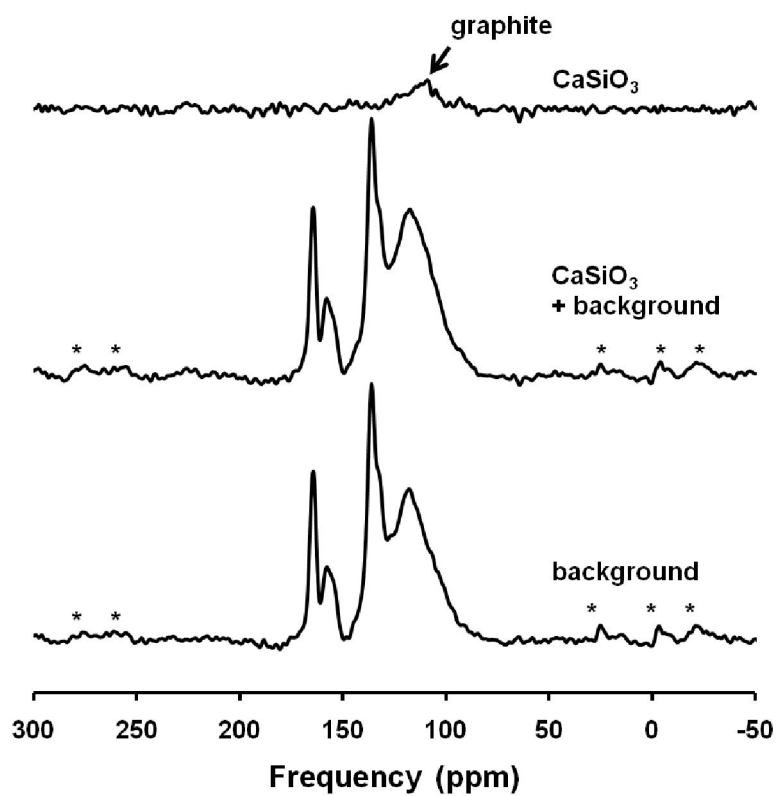


Figure 17 | One-dimensional ^{13}C MAS NMR spectra of carbon-bearing CaSiO_3 synthesized in CO gas flow at 1 atm. An asterisk refers to spinning sidebands.

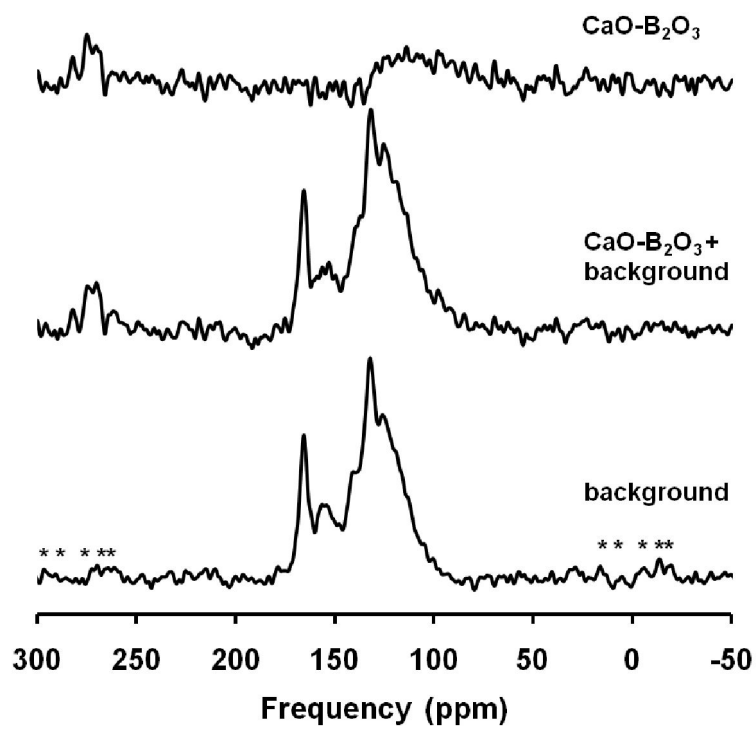


Figure 18 | One-dimensional ^{13}C MAS NMR spectra of carbon-bearing $\text{CaO-B}_2\text{O}_3$ synthesized in CO gas flow at 1 atm. An asterisk refers to spinning sidebands.

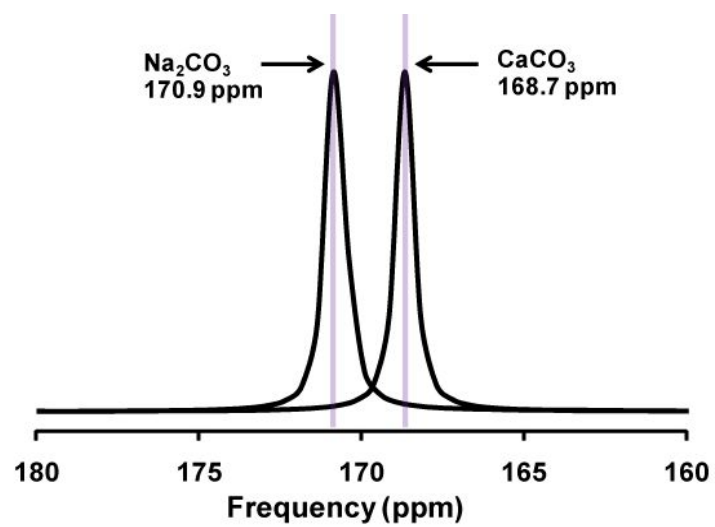


Figure A1 | ^{13}C MAS NMR spectra of CaCO_3 and Na_2CO_3 . The spectra are obtained from T_1 relaxation time measurements and the intensity is normalized to its maximum.

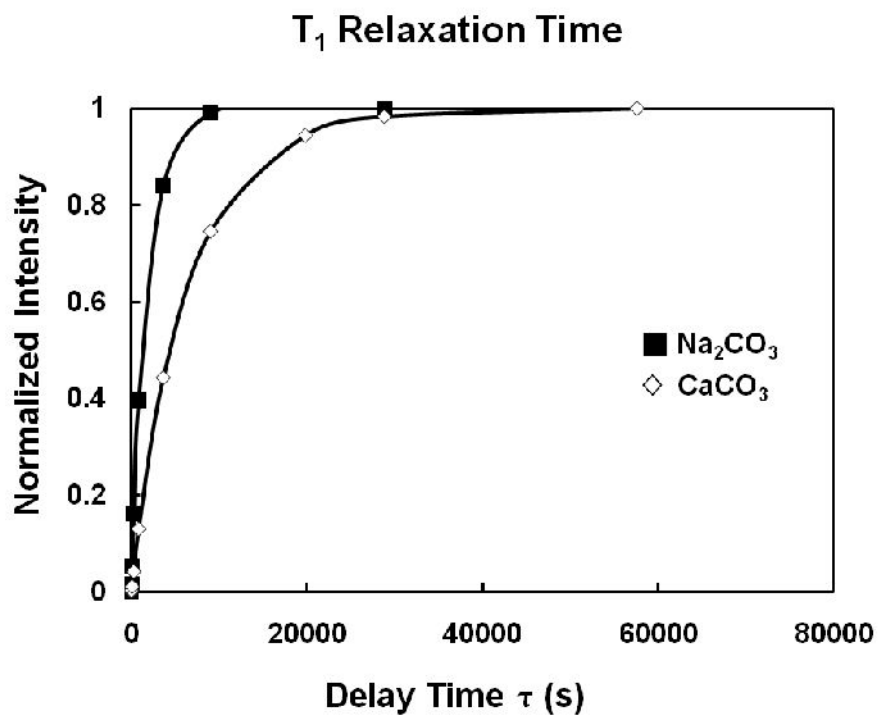


Figure A2 | Normalized maximum intensity of ¹³C NMR spectra for CaCO₃ and Na₂CO₃ as a function of delay time (s). Na₂CO₃ shows shorter T₁ relaxation time than CaCO₃.

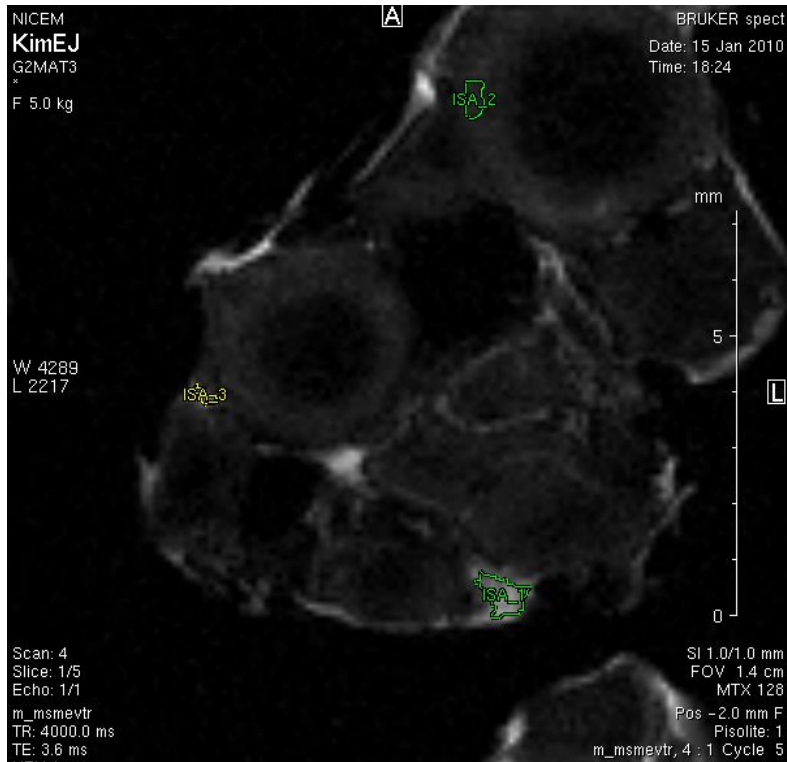


Figure A3 | Micro-NMR Imaging of pisolite. The selected areas are where we measure the T_1 relaxation time of water absorbed into pisolite.

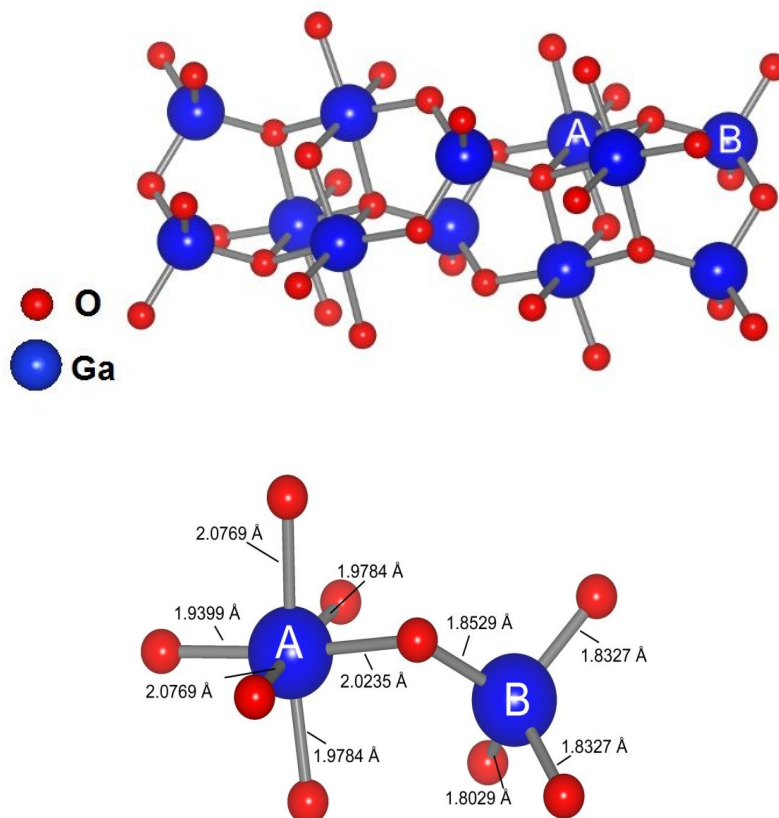


Figure A4 | Crystal structure of $\beta\text{-Ga}_2\text{O}_3$. (Top) Blue sphere is gallium and red sphere is oxygen. Unit cell structure of $\beta\text{-Ga}_2\text{O}_3$ shows two distinct gallium sites; octahedral sites and tetrahedral sites. (Bottom) Bond lengths of Ga-O in octahedron and tetrahedron. A and B mean the atoms at the top figure.

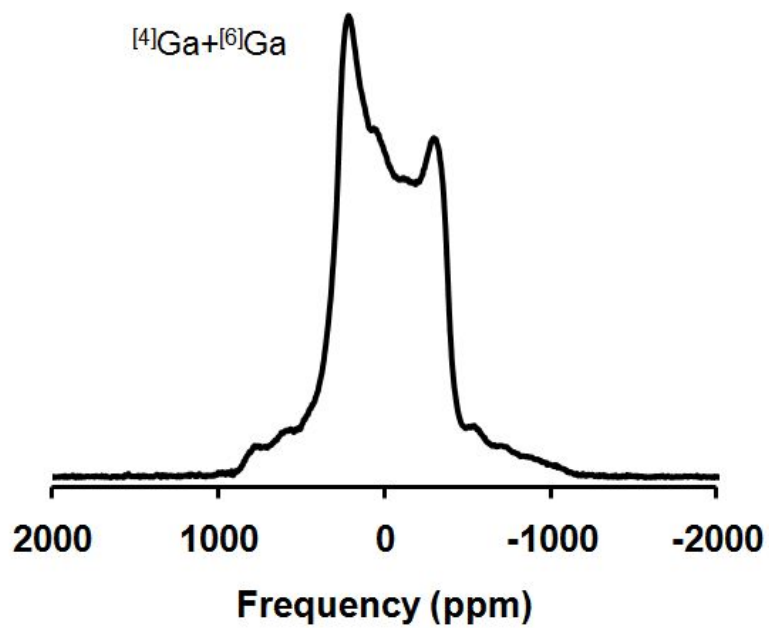


Figure A5 | ^{71}Ga static NMR spectrum of $\beta\text{-Ga}_2\text{O}_3$.

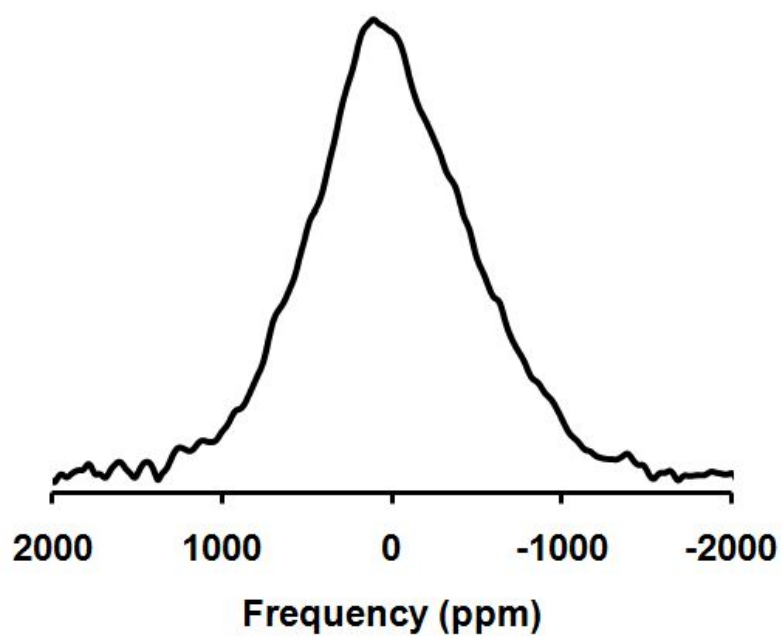


Figure A6 | ^{71}Ga static NMR spectrum of Ga-In-Zn oxide thin film.

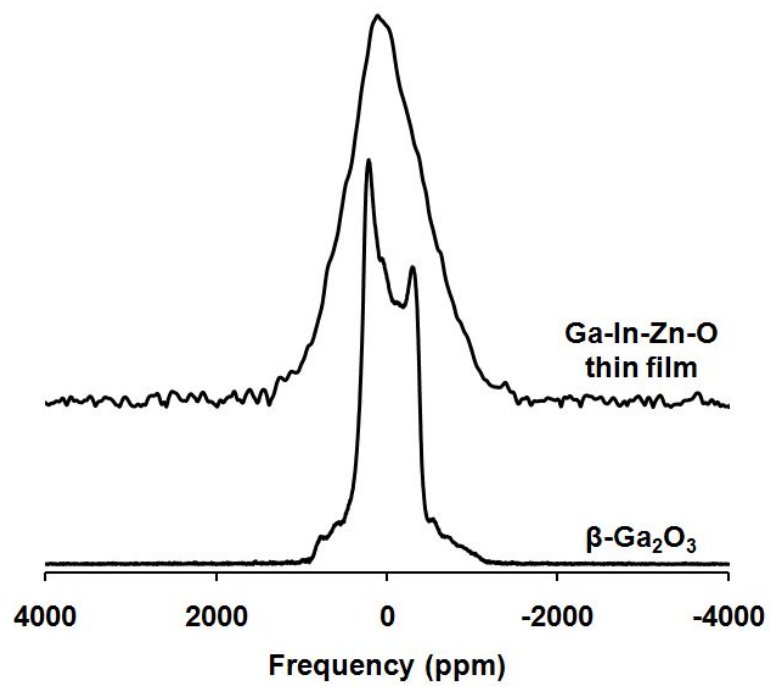


Figure A7 | ^{71}Ga static NMR spectra of $\beta\text{-Ga}_2\text{O}_3$ and Ga-In-Zn oxide thin film.

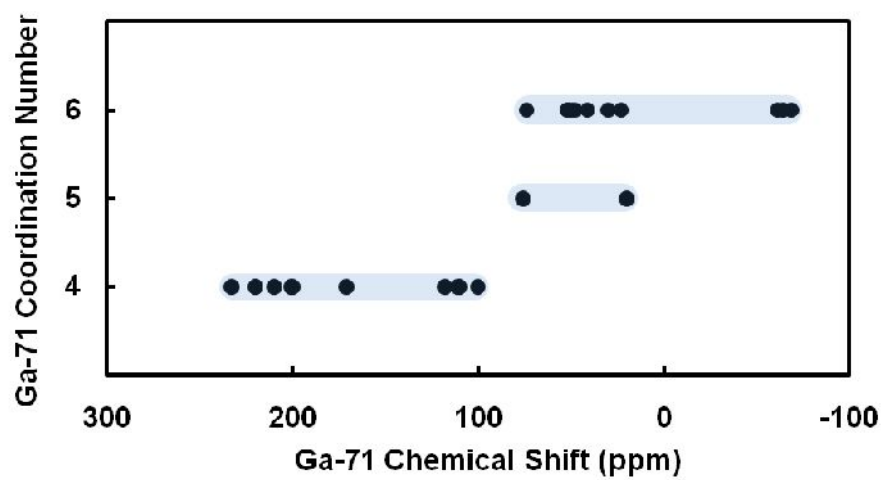


Figure A8 ^{71}Ga NMR chemical shift range of four, five, and six-coordinated Ga in crystalline Ga compounds.

Appendix section

Appendix I. T_1 relaxation time measurement

Determining T_1 relaxation time is important for quantitative analysis. T_1 relaxation is the interaction between spin and lattice (longitudinal relaxation). T_1 relaxation time is the time the max intensity spectrum is obtained. In solid-state NMR, recycle time is set about as three times as T_1 relaxation time. If we set the insufficient recycle time, the peak intensity decreases because of dephasing of signal due to the insufficient recycle time. Each species of nuclide can have different T_1 relaxation time. If the recycle time is not enough for some species, the peak of specific species decreases as the signal is collected and it is hard to get quantitative information from the spectrum.

Carbon has two major species in silicate melts; molecular CO_2 and carbonate ion structure CO_3^{2-} . What I want to know is the exact speciation of carbon in silicates and its quantitative analysis. The absolute amount of carbon in silicate is about tens to hundreds ppm by weight, and it is not a big difference between background signal and carbon in silicate signal. Measuring T_1 relaxation time of this sample is significant to get a high quality and quantitative C-13 NMR spectrum.

Figure A1 shows the C-13 MAS spectra of CaCO₃ and Na₂CO₃. CaCO₃ is a trigonal crystal with $R\bar{3}c$ space group, and Na₂CO₃ is a monoclinic crystal with $C2$ space group. Chemical shift is dependent on the atomic structure of nuclide, so CaCO₃ and Na₂CO₃ show the different chemical shift; 168.7 ppm, and 170.9 ppm, respectively.

Figure A2 shows the T1 relaxation time of CaCO₃ and Na₂CO₃ measured by NMR. Intensity of each spectrum is normalized by its maximum intensity. Experimental condition of each experiment is same except the recycle time condition. Echotime is arrayed from 0.5 s to 28800 s for Na₂CO₃ and 2 s to 57600 s for CaCO₃. Echotime and normalized intensity is plotted by exponential function,

$$M_z = M_0(1 - e^{-\frac{t}{T_1}})$$

M_z is the longitudinal magnetization, M_0 is the equilibrium magnetization, T_1 is T_1 relaxation time, and t is the echotime. Fitted in this equation, relaxation time of CaCO₃ is calculated as 6418 s with the 107 s of error, and 1729 s with 90 s of error for Na₂CO₃.

Appendix II. NMR Imaging.

NMR imaging spectroscopy is non-destructive 2D or 3D imaging technique with the resolution below 10 μm . The resolution is dependent on the contents of fluid, spin-spin relaxation time of fluid, and the connectivity of fluid in pores. A image is obtained by converting the frequency signal to space axes using the inhomogeneous magnetic field in Z-axis. It is called 'magnetic field gradient'. NMR imaging is sensitive to liquid phases, so by this process we can get a NMR image of fluids absorbed in solid, the distribution of fluids in solids, fluid-fluid interaction in pore structure of solids.

Figure A3 shows the NMR imaging of water-absorbed pisolite. This is obtained by 'm_msmevtr' method which can get 2D images of the sample. By varying the parameters, we can find the T_1 and T_2 relaxation time of fluid presented or absorbed in the pore structure of solid. Table A1 shows the T_1 relaxation time of the selected area. The brightness in the picture is how much water is detected by NMR imaging, and that means brighter spots have more water than darker spots. The brightest spots in the figure have water as isolated phases, and grey spots in the figure have water as absorbed phases.

Appendix III. Structure of Ga-In-Zn-O Thin Film: ^{71}Ga

NMR Studies

III-1. Introduction

GIZO thin film is used for thin film transistor. Because of its light-weight and a flexible property, GIZO thin film has received recent attention. It is spotlighted with electric paper, 3D peripheral circuit memory, flat display panel, and building blocks (Park, Lee et al. 2009; Nomura, Kamiya et al. 2010; Yoon, Yang et al. 2010). Ga is involved with site exchange with Al in crystalline phases, and substitution of Ga with Al can control the activity of zeolite used for catalyst. In these reasons, it is important to reveal the atomic structure of Ga in crystal and amorphous materials.

There are difficulties in investigating the structure of amorphous thin film with ordinary spectroscopy and X-ray scattering, but with solid-state nuclear magnetic resonance spectroscopy amorphous oxide researchers in Seoul National University have been discovering the structure of amorphous thin film(Lee, Lee et al. 2009).

There are two isotopes of gallium and the ratio of each are 60.4 % for ^{69}Ga and 39.6 for ^{71}Ga . Both of isotopes can be used for NMR spectroscopy but the relative sensitivity is higher for ^{71}Ga whose value is 0.14 than for ^{69}Ga whose relative sensitivity is 0.069, so ^{71}Ga is used for Ga NMR. ^{71}Ga is

categorized to a quadrupolar nuclide whose nuclear spin is $3/2$. Quadrupolar nuclides show 2nd quadrupolar effect because 2nd order perturbation is not zero in quadrupolar nuclides and quadrupolar effect does not appear from nuclides whose nuclear spin is $1/2$. Quadrupolar nuclides are hard to analyze NMR spectra because of broad peaks due to anisotropy and asymmetric peak shape. However, gallium has relatively high sensitivity and the structure of Ga-included complexes is getting more attention, so many papers have reported the atomic structure of Ga in crystal with ^{71}Ga NMR (Massiot, Farnan et al. 1995; Vosegaard, Massiot et al. 1997; Bureau, Silly et al. 1999; Massiot, Vosegaard et al. 1999; Jung, Park et al. 2003). Compared with the studies of atomic structure of Ga in crystalline phases, atomic structure of Ga in amorphous phases has not been studied due to the disorder of glass itself. There is no NMR study of Ga-bearing thin film until now. In this study, we report the local atomic structures of Ga thin films using ^{71}Ga NMR.

III-2. Experiments

Sample Preparation. $\beta\text{-Ga}_2\text{O}_3$ is used as a reference material to set up the ^{71}Ga NMR condition. $\beta\text{-Ga}_2\text{O}_3$ is purchased from Sigma Aldrich (serial number 215066), and GIZO thin film is taken from Jaejun Yu, the professor of department of physics and astronomy in SNU. Substrate

was removed from the sample until the thickness of the sample reached 20 μm to enhance the signal from the GIZO thin film.

NMR Spectroscopy. The ^{71}Ga NMR spectra were collected with Varian 400 MHz NMR spectroscopy (9.4 T) at a Larmor frequency of 121.989 MHz using a 4 mm Doty double resonance probe. The ^{71}Ga NMR spectra were referenced to Ga-nitrate atomic environments. Because of the high quadrupolar coupling constant, it is difficult to distinguish the signal from the spinning side band when the magic angle spinning (MAS) experiment is processed, so static experiment is performed. The procedure of the ^{71}Ga NMR was followed Hahn echo sequence. The recycle delay is 1 s and the 360° pulse length is 8 μs .

III-3. Results and Discussion

$\beta\text{-Ga}_2\text{O}_3$ is used for the reference to investigate the atomic environment of Ga in GIZO thin film. Figure A4 shows the crystal structure of $\beta\text{-Ga}_2\text{O}_3$. $\beta\text{-Ga}_2\text{O}_3$ is monoclinic system and is categorized in $C_{2/m}^2$ space group. The length of unit cell is $a=12.23 \text{ \AA}$, $b=3.04 \text{ \AA}$, $c=5.80 \text{ \AA}$, and axial angle is 103.7° . $\beta\text{-Ga}_2\text{O}_3$ has two distinguishable crystal sites of Ga as shown in Figure A4. One site is asymmetric tetrahedron and the other is asymmetric octahedron. They are arranged in a different direction. The

bond length of Ga-O of six-coordinated Ga is from 1.9399 Å to 2.0769 Å, and the bond angle of O-Ga-O is 171.934° which represents asymmetry of octahedron site. For four-coordinated Ga, the bond length is from 1.8029 Å to 1.8529 Å, and the bond angle of O-Ga-O of four-coordinated Ga is from 117.908° to 117.908°.

Figure A5 shows the ^{71}Ga static NMR spectrum of $\beta\text{-Ga}_2\text{O}_3$. From figure A4, it is analogized that the ratio of four- and six-coordinated Ga is 1 to 1. Table A1 is the previous NMR studies of ^{71}Ga NMR. According to table A2, chemical shift for four-coordinated Ga ranges between 100 and 200 ppm, and chemical shift for six-coordinated Ga ranges between -69 and 74 ppm.

Figure A6 presents the ^{71}Ga static NMR spectrum of GIZO thin film which shows a broad peak and whose FWHM is about 1000 ppm. ^{71}Ga static NMR spectrum of crystalline $\beta\text{-Ga}_2\text{O}_3$ featured in figure A5 shows 50 ppm of FWHM and tooth-shaped spectrum which can be found in NMR spectrum of general quadrupolar nuclide. In spite of figure A5, figure A6 shows the one broad peak, and spectrum has wider FWHM than in figure A5. Figure A7 shows the stack spectra of GIZO thin film and $\beta\text{-Ga}_2\text{O}_3$ crystal power. The broad peak in GIZO thin film cannot be simulated by one Gaussian or Lorentzian function. If there is one or two atomic environment, we can simulate the adequate atomic environment with Gaussian or Lorentzian function. In other words, this ^{71}Ga NMR spectrum

of GIZO thin film suggests that Ga in GIZO thin film should have structurally and topologically disordered atomic environment. Figure A8 presents the ^{71}Ga chemical shift as a function of atomic structure of Ga. Specific chemical shift data are shown in Table A1. Chemical shift range of four-coordinated Ga is from 100 to 220 ppm; from 20 to 76 ppm for five-coordinated Ga and from 69 to 74 ppm for six-coordinated Ga. There is a linear correlation between the coordination number and chemical shift in ^{71}Ga NMR. As the coordination number increases, chemical shift decreases. It is inferred from ^{71}Ga static NMR spectrum of $\beta\text{Ga}_2\text{O}_3$ and the change of chemical shift of other Ga complexes that Ga has four-, five- and six-coordinate atomic structure in GIZO thin film. However, we cannot clearly separate each atomic environmental peak from the spectrum of GIZO thin film because there is no specific information of peak position or quadrupolar coupling parameter of GIZO thin film. Quadrupolar broadening effect is reduced by NMR experiment with higher magnetic field. To analyze the atomic environment of GIZO thin film, experiments at higher field NMR is needed.

In this study, we report the first ^{71}Ga static NMR spectrum of amorphous GIZO thin film. GIZO thin film consists of quadrupolar nuclide Ga, and paramagnetic element In and Zn. The first ^{71}Ga NMR spectrum of GIZO thin film shows one broad peak and it is inferred that four-, five-, and six-coordinated Ga exists in GIZO thin film compared to the NMR

spectrum of β -Ga₂O₃ which has four- and six-coordinated Ga atomic environment. Because of the low resolution of the spectrum, we cannot analyze the quantitative atomic structure. We can obtain a better resolution spectrum with higher magnetic field NMR.

Eun Jeong Kim

Education

- 2009.8 ~ Candidates of M.S. Seoul National University, Korea. School of
Earth and Environmental Sciences
2009. 8 B. S. Seoul National University, Korea. School of Earth and
Environmental Sciences

Research Experience

- 2010 Teaching assistant, Seoul National University
- 2009 ~ 2011 Research assistant, Seoul National University

Research Interest

Physics and Chemistry of Earth Materials

Honors & Awards

- 2011.2 Scholarship from the Lotte foundation
- 2010.8 Scholarship from the Lotte foundation

Publications

- Lee, S. K., H. N. Kim, et al. (2010). "Nature of Chemical and Topological Disorder
in Borogermanate Glasses: Insights from B-11 and O-17 Solid-
State NMR and Quantum Chemical Calculations." J. Phys. Chem.
B 114(1): 412-420.

Conferencess

2011. 5 1.5 GPa에서 결정질 엔스테타이트의 탄소 용해도에 관한 미시적 기원 연구 (Oral), 2011년 한국광물학회 학술발표회
2010. 10 고압 환경에서 마그네슘 규산염 광물의탄소 용해도에 대한 미시적 기원 연구: 지구 내부에서의 탄소 순환의 고찰 (Oral), 2010년 추계지질과학연합 학술발표회

국문 요약

결정질 규산염 및 맨틀 용융체에 존재하는 기체들은 결정 및 용융체의 성질을 바꾸는 데 중요한 역할을 한다. 결정질 규산염에 존재하는 기체들은 결정질 물질들의 상전이 곡선을 바꾸므로 부분 용융으로 생성되는 마그마의 조성은 기체들의 존재 및 용해도에 따라 크게 바뀐다. 비정질 규산염에 존재하는 이산화탄소는 탄산염 이온(CO_3^{2-})이나 이산화탄소 분자의 형태로 존재할 수 있는데, 이것은 미시적인 관점에서 비정질 규산염의 중합도(polymerization)을 바꾸어 맨틀의 점성도에 영향을 줄 수 있다. 이산화탄소는 마그마에 존재하는 기체들 중 두 번째로 양이 많은 기체로, 압력에 따른 용해도의 차이가 크기 때문에 화산 분출이 일어날 때에는 다량의 이산화탄소가 지권으로부터 대기권으로 방출된다. 대기권으로의 이산화탄소의 유입은 기후 변화에 영향을 줄 수 있으며, 운석 내에 용해되어 있는 탄소의 양으로부터 추정하였을 때 맨틀에 지구상에서 가장 많은 양의 탄소 화학종이 존재할 것으로 생각되지만 이에 대한 실험 데이터들이 부족했기 때문에 1950년대부터 지금까지 여러 다성분계 규산염 물질에서의 이산화탄소의 용해도 및 용해 기작을 설명하기 위한 연구들이 활발히 진행되어 왔다. 하지만 분광 분석기기들의 분석 한계 및 분석 방법서부터 기인한 정량 분석이 어려움, 그리고 이산화탄소의 낮은 용해도로 인해 이산화탄소가

용해되었을 때의 탄소의 화학종 변화에 대한 연구만이 명확히 규명되어 있으며 이산화탄소로 인한 원자 구조의 변화를 명확히 규명한 예는 없다.

본 연구에서는 특정 원소에 대한 원자 구조를 제공함과 동시에 정량적인 분석이 가능한 고분해능 고상 핵자기 공명 분광 분석(NMR, nuclear magnetic resonance)를 이용하여 맨틀의 모델 시스템으로 볼 수 있는 이성분계 결정질 규산염인 MgSiO_3 엔스테타이트(enstatite)와 중앙해령 현무암(MORB, mid ocean ridge basalt)의 모델 시스템으로 볼 수 있는 이원계 비정질 규산염인 CaO-SiO_2 의 공유점 조성과 CaSiO_3 , 그리고 이원계 비정질 $\text{CaO-B}_2\text{O}_3$ 에 대해 이들에 용해된 탄소의 원자 구조를 규명하였다.

NMR을 이용하여 분석할 수 있는 탄소 동위원소는 자성 모멘트가 있는 ^{13}C 로, 자연 존재량이 1.1%이기 때문에 분광 분석에 어려움이 있다. 엔스테타이트에 용해된 탄소의 양은 ppm 단위로 자연 존재하는 ^{13}C 를 이용하여 분석하기에는 그 양이 매우 적기 때문에 ^{13}C 를 강화(enrich)하여 분석하였다. 이원계 비정질 산화물들의 경우 C/CO 평형을 맞추었을 때 이원계 비정질 규산염은 400 ppm 정도이고, 이원계 비정질 $\text{CaO-B}_2\text{O}_3$ 는 1000 ppm 정도의 탄화물(C_2^{2-} , carbide)이 용해된다는 이전 연구 결과에 따라 자연 존재하는 ^{13}C 를 이용하여 분석하였다.

엔스테타이트의 결정 구조에는 Mg^{2+} 가 들어가는 M 구조와 O^{2-} 가 Si^{4+} 와 연결되어 있는 사면체 구조가 존재한다. 합성된 시료가 엔스테타이트의 결정 구조를 유지하고 있는지를 확인하기 위하여 수행한

Raman 분광 분석에서 시료의 진동 모드는 기존에 알려진 엔스테타이트의 진동 모드와 일치함을 확인하였다. 그러나 Raman 분광분석을 통하여 기존에 알려진 기체상의 CO_2 의 진동 모드나 CO_3^{2-} 의 진동모드는 확인할 수 없었다. ^{13}C NMR 분석결과에서 126, 161, 171, 173, 그리고 184 ppm에서 피크가 존재함을 보았고, 이전 연구 결과에 따라 용해된 일산화탄소가 184 ppm에서 나타나며 탄산염 이온이 161, 171, 그리고 173 ppm에서 나타남을 확인하였다. 126 ppm에서 나타나는 피크에 대해서는 이산화탄소인 경우와 사베위수 탄소인 경우의 두 가지 원자 환경이 존재할 수 있다. 우선 NMR 분석결과에서 나타나는 126 ppm 피크가 실험적으로 나타나는 노이즈인지 아니면 실제 시료로부터 나오는 피크인지를 확인하기 위해 같은 합성 조건에서 합성한 시료를 통해 ^{13}C NMR 분석을 다시 수행하였고, 그 결과 126 ppm 피크는 재현 가능한 실제 피크인 것으로 확인되었다. 이에 따라 126 ppm 피크가 나타내는 탄소의 원자 환경을 정의하고자 탈기체화 반응과 양자 화학 계산을 수행하였다.

탈기체화 반응은 두 번째 합성한 시료를 이용하였으며 750 °C에서 10분간 가열했다. 탈기체화 반응 후 얻어진 시료는 ^{13}C NMR 실험에서 이전 실험에서 보이던 126 ppm 피크가 사라진 것을 확인하였다. 그러나 불안정한 사베위수 탄소가 탈기체화 반응 과정에서 화학 결합을 끊고 사라질 수 있으며, 이전 연구들에서 사베위수 탄소에 대한 양자 화학 계산이 존재하지 않았기 때문에 사베위수 탄소에 대한 양자 화학 계산을

수행하였다. 양자 화학 계산은 가우시안 03 프로그램을 이용하였다. 양자 화학 계산의 정확도를 평가하고자 계산된 화학 차폐값을 알고 있는 CO₂ 구조를 이용하여 양자 화학 계산을 실시한 후, 이 중에서 가장 정확도가 높은 계산 방법론을 이용하여 사베위수 탄소에 대한 계산을 수행하였다. B3LYP/6-311+G(2d) 방법을 이용한 계산 결과 사베위수 탄소는 254 ppm에서 화학 차폐값을 나타내는 것으로 확인되었다.

이원계 비정질 규산염 물질인 CaSiO₃와 CaO-SiO₂의 공융점 조성에 대한 시료는 1 기압 하에서 합성되었다. 초기에 합성한 시료는 Ar 분위기에서 ¹³C을 강화한 CaCO₃를 이용하여 합성하였다. 이들 시료에서는 ¹³C NMR 실험을 통해 탄소 원자 환경이 규명되지 않았으며 이것은 CaCO₃에 존재하는 이산화탄소가 가열 과정에서 열분해되어 사라지고 NMR을 통해 분석 가능한 하한선보다 적은 양의 이산화탄소가 용해되어서 나타나는 현상으로 생각된다. CO 분위기에서 C/CO 평형을 이룬 시료들에 대해서 400 ppm의 탄소가 용해될 수 있다는 이전 연구결과로부터 같은 조성의 시료에 대해서 흑연 도가니를 이용하여 CO 분위기에서 합성하였다. 두 번째 합성한 시료의 경우 흑연 도가니에서 함께 나온 흑연 불순물을 제대로 제거하지 못하여 흑연의 ¹³C NMR 스펙트럼만을 얻을 수 있었다. 이것은 시료가 C/CO 평형을 이루어 400 ppm 정도가 용해되어도, ¹³C을 강화하여 합성한 시료가 아니므로 시료에 용해된 탄소 화학종 중 NMR로 분석할 수 있는 것들은 4 ppm 이하로 매우 적은 양이기 때문에 나타나는 현상으로 생각된다. 이로부터 ¹³C

MAS NMR 연구를 통해 현재까지 분석할 수 있는 하한치는 적어도 4 ppm 이상은 되어야 하는 것으로 생각된다.

CaO:B₂O₃의 몰비율이 39.7:60.3 인 이원계 비정질 봉산염 물질은 CO 분위기에서 C/CO 평형을 이루었을 때 1000 ppm 정도의 탄소가 용해될 수 있다고 알려졌다. 1 기압 하에서 흑연 도가니를 이용하여 CO 분위기에서 합성한 탄소를 포함하는 봉산염의 ¹³C MAS NMR 결과에서는 불순물로 포함된 흑연의 피크와 이전 결과들에서는 보이지 않던 270 ppm의 피크가 나타난다. 이것은 양자 화학 계산에서 사베위수 탄소가 나타내는 NMR 화학 차폐의 값과 비슷한 영역이다. 이 피크가 실제 시료에 존재하는 탄소의 원자 환경을 나타내는 피크인지를 확인하기 위해서는 이전과 같이 시료를 재합성 및 재실험 과정을 거쳐야 할 것으로 생각된다. 이 피크가 봉산염에 존재하는 사베위수의 봉산을 치환하여 들어간 탄소가 나타내는 원자 환경이라면, 이것은 실험적으로는 처음으로 산소와 탄소로 이루어진 사면체 구조에 존재하는 사베위수의 탄소의 원자 구조를 밝힌 것이다.

실험을 수행하는 과정에서 초기 물질로 들어간 비정질 탄소와 압축된 비정질 탄소에 대한 ¹³C MAS NMR 실험도 처음으로 수행되었다. NMR 실험 결과에서 비정질 탄소는 138 ppm에서 넓은 반치폭의 피크를 보이며 이것은 비정질 탄소에서 sp² 혼성화된 탄소가 나타내는 피크이다. 압축된 비정질 탄소는 68 ppm에서 넓은 반치폭의 피크를 보이며 이것은 비정질 탄소에서 sp³ 혼성화된 탄소가 나타내는 피크이다. 압축된

비정질 탄소의 피크 위치가 비정질 탄소의 피크와 다른 곳에서 나타나는 것은 피스톤 실린더를 이용한 고압 실험과정에서 비정질 탄소에 압력으로 인한 영구적인 구조 변화가 일어난 것으로 생각된다. Raman 분광 분석을 이용하여 비정질 탄소와 압축된 비정질 탄소에 대한 진동 모드에 대한 연구도 수행되었다. 비정질 탄소의 경우 1200~1600 cm^{-1} 의 영역에서 흑연의 진동 모드가 나타난다. 이 중 1550 cm^{-1} 의 영역에서 G 모드라고 불리는 미세 결정질 흑연의 진동 모드가 나타나며, 1350 cm^{-1} 의 영역에서 D 모드라고 불리는 무질서한 미세 흑연 결정의 진동 모드가 나타난다. 비정질 탄소의 Raman 분광 분석에서는 1200~1600 cm^{-1} 영역에서 넓은 피크가 나타나는 반면에 압축된 비정질 탄소의 경우 G 모드라고 불리는 1550 cm^{-1} 의 영역에서 피크가 나타난다. 이것은 압력에 의해 구조 변화가 생기면서 비정질 탄소의 무질서도가 줄어들고 미세 결정질 흑연이 증가하였음을 알려준다.

위의 실험들은 이제까지는 실험 시간이 오래 걸리고 측정하기 어려워 잘 시도되지 않던 ^{13}C MAS NMR 실험을 이용하여 결정질 규산염 및 비정질 산화물에 용해된 탄소의 화학종을 밝혔으며 NMR을 이용하여 측정할 수 있는 용해도의 한계치가 어디까지인가를 확인했다는 데에 의의가 있다. 또한 비정질 붕산염 물질에서는 B^{4+} 를 치환하여 사면체 구조에 들어가 있는 C^{4+} 가 발견된 것으로 생각되는데, 이것이 실제 원자 환경을 나타내는 피크라면 이제까지 주장만 되어오던 사배위수의 탄소 원자 환경에 대하여 실험적으로 보인 첫 결과이다.

높은 압력 조건에서 실험을 수행한다면 비정질 규산염 물질에서도 규소와 탄소의 치환반응을 통한 사배위수의 탄소의 원자 환경을 발견할 수 있을 것으로 기대된다. 본 연구에서 얻어진 이원계 규산염에서의 이산화탄소의 원자 구조에 대한 정보는 전지구적인 지질현상에서 나타나는 이산화탄소의 용해 및 분출 기작을 설명해주며, 탄소의 원자 구조에 대한 새로운 실험 결과를 제시하고 있다. 이를 통해 지구 내부에서의 탄소 순환을 미시적인 관점에서 설명을 할 수 있다.

주요어: 이산화탄소, 휘발성 유체, 이성분계 비정질 규산염, 엔스테타이트, NMR, 원자 구조